ALMA MATER STUDIORUM A.D. 1088
UNIVERSITÀ DI BOLOGNA

DIPARTIMENTO DI SCIENZE BIOLOGICHE,
GEOLOGICHE E AMBIENTALI

Corso di Laurea Magistrale in Geologia e Territorio

Tesi di Laurea Magistrale

Thrusting and veining under blueschist facies conditions: multi-technique and multiscalar study of the Little Snake Gorge Thrust, Jabal Akhdar Mountains (Oman)

Candidato:
Tommaso Sanguettoli

Relatore:
Prof. Giulio Viola

Correlatore:
Dott. Costantino Zuccari

Sessione luglio 2025
Anno Accademico 2024-2025

ABSTRACT

The Oman Mountains are a geologically complex orogenic system formed by the interplay of several geodynamic processes and tectonic events. This complexity makes the region an exceptional natural observatory for examining the genesis and evolution of subduction zones, as well as the dynamics of accretionary wedges and obduction processes. Within the central-eastern sector of the mountain range, the Jabal Akhdar Dome stands as a prominent tectonic window, providing exceptional exposure to intricate structural frameworks and evolutionary sequences associated with its multi-phase geological history. The dome exposes a metasedimentary succession spanning from the Neoproterozoic to the Cretaceous that is representative of the Arabian Plate's former passive continental margin. Historically, the Jabal Akhdar Dome has been interpreted as having experienced only low-grade, anchizonal metamorphism, with a structural configuration largely unaffected by the deep subduction processes that reworked the northeastern margin of the Arabian Plate during the Cretaceous. However, recent findings have begun to challenge this paradigm. The discovery of blueschist-facies metamorphism dated to the Cretaceous suggests that the region was indeed affected by high-pressure, low-temperature metamorphic conditions typically associated with subduction channel environments. Targeted field investigations within a critical area of the dome - the so-called "Little Snake Gorge" - have produced new structural and metamorphic constraints. These findings, combined with petrological analyses, enable a reassessment of the dome's tectono-metamorphic evolution in light of the newly identified high-pressure constraints. The study of the deformation structures associated with the main tectonic contact, referred to as the "Little Snake Gorge Thrust", along with multiple occurrences of metamorphic aragonite infilling foliation-parallel Mode I veins, supports the interpretation of a Cretaceous high-pressure and low temperature metamorphic overprint. This event is likely linked to the Late Cretaceous subduction of the Arabian continental passive margin below the Eurasian plate. Subduction-related deformation induced a complex folding history within the exposed Precambrian lithologies, characterized by alternating brittle and ductile deformation stages. Moreover, the structural data collected provide critical insights into the deformation style associated with high-pressure metamorphism during subduction. To constrain the metamorphic conditions responsible for these features, Raman Spectroscopy on Carbonaceous Material (RSCM), associated with the thermodynamic equilibrium boundary between calcite and aragonite, has been employed. The results yield peak metamorphic conditions of approximately 348 ± 50 °C and 0.85 ± 0.12 GPa in the Mu'aydin Formation in the footwall to the thrust, as exposed within the Little Snake Gorge. To interpret these findings, a conceptual model involving progressive deformation is proposed to describe the tectonic evolution of the Little Snake Gorge Thrust. This model, based on existing U-Pb geochronological data, emphasizes the progressive rotation of the principal stress axes, which likely governed the observed structural patterns during the Late Cretaceous subduction of the Arabian passive margin. The deformation history comprises an initial SW-NE-directed phase of layer-parallel shortening (LPS), followed by active folding and thrusting under blueschist-facies conditions, and culminating in a secondary, NNW-SSE-directed folding phase attributed to the progressive rotation of the stress field relative to the subducting slab. This final stage gave rise to the interference structures currently observed in the field. These novel results provide a valuable opportunity to better understand the deformation mechanisms associated with high-pressure metamorphism and to revise existing tectonometamorphic models that describe the structural architecture and the evolution of the Jabal Akhdar Dome.

INDEX

INTRODUCTION

The Oman Mountains exhibit a remarkably complex polyphase tectonic history (e.g., Loosveld et al., 1996; Scharf et al., 2021; Weidle et al., 2023), making them an exemplary natural laboratory for the in-depth investigation of fundamental geodynamic processes such as lithospheric stretching and rifting, continental passive margin evolution, oceanic plate subduction, subduction-related metamorphism, and, above all, obduction of oceanic lithosphere. The Cretaceous tectonic convergence between the Afro-Arabian and Eurasian plates did not culminate in continental collision, differentiating this region as a singular geodynamic domain within the broader Alpine-Himalayan orogenic belt (e.g., Van Hinsbergen et al., 2009; Scharf et al., 2021). Instead, the local tectonic evolution was achieved through a protracted and spatially complex subduction-obduction cycle, after which the main convergence axis progressively migrated northward toward the Makran subduction system and the Zagros Mountains collisional front, in present-day Iran, where continental collision was ultimately realized during the Eocene (e.g., Molinaro et al., 2005; Mouthereau et al., 2012). This has resulted in the exceptional preservation of the subducted sequence in Oman, with minimal reworking or overprinting by subsequent Cenozoic orogenic processes. Consequently, the region offers unparalleled exposure of features related to passive continental margin subduction, enabling high-resolution analysis of the structural, metamorphic, and kinematic signatures of subduction and obduction dynamics, which are often obliterated in other orogenic belts due to superimposed collisional deformation and crustal thickening.

The internal Oman Mountains expose two major tectonic windows, the Jabal Akhdar and Saih Hatat Domes, which offer access to the metasedimentary stratigraphy of the Arabian Plate, spanning from the Neoproterozoic to the Cretaceous (e.g., Hanna, 1990; Mann & Hanna, 1990; Scharf et al., 2021). These structural culminations allow for detailed analysis of the complex and multi-stage deformation events that have been recorded over geological time. Although the Saih Hatat Dome has been extensively investigated, particularly concerning its metamorphic evolution and structural development within the context of the Cretaceous subduction (e.g., El-Shazly et al., 1990; Searle et al., 1994; Miller et al., 1998), integrated studies addressing the metamorphic conditions and internal deformation architecture of the Jabal Akhdar Dome remain, instead, relatively scarce. This disparity in research emphasis is likely attributable to the contrasting metamorphic and tectonic signatures preserved in the two domains. Saih Hatat hosts a well-documented assemblage of high-pressure metamorphic rocks, indicative of subduction to depths approaching c. 80 km, whereas Jabal Akhdar is generally associated in the literature with a low-grade, anchizonal metamorphism and a structural framework that appears largely unaffected by the deep subduction processes that reworked the northeastern margin of the Arabian Plate during the Cretaceous (e.g., Le Metour et al., 1990; Mann & Hanna, 1990; Breton et al., 2004; Scharf et al., 2021). However, recent investigations have yielded pressure-temperature estimates consistent with high-grade metamorphic conditions, specifically within the blueschist facies domain (Zuccari et al., 2023), thereby calling into question the conventional interpretations previously established in the literature.

High-pressure mineral assemblages preserved in exhumed metamorphic rocks provide critical insights into the pressure-temperature histories and deformation processes within subduction zones (e.g., Agard et al., 2009; Rubatto et al., 2011; Zuccari et al., 2023). The extent to which these assemblages are retained depends on factors such as exhumation dynamics, regional thermal conditions, fluid activity, strain intensity, and mineral stability, all of which influence retrograde transformations (e.g., Goffé & Velde, 1984; Zuccari et al., 2023).

Structural studies of exhumed subduction complexes reveal that thrust zones formed under blueschist-facies conditions commonly record a combination of brittle and ductile deformation. Brittle shear veins can transition into ductile shear zones within a blueschist matrix, reflecting synchronous frictional-viscous deformation under high-pressure, low-temperature regimes and elevated fluid pressures. This results in intricate structural fabrics characterized by repeated overprinting of metamorphic foliations, cataclasites, and vein networks within blueschist-facies shear zones (Behr & Burgmann, 2021; Muñoz-Montecinos et al., 2021; Zuccari et al., 2023). Cyclic brittle-ductile deformation under high-pressure conditions, combined with foliation-parallel permeability structures, typically promotes fluid flow along shear zones, which thus act as transient high-permeability pathways (Molli et al., 2017; Zuccari et al., 2023).

Considering the significance of recording high-pressure conditions in the Jabal Akhdar Dome, the primary goal of this thesis is to integrate structural and metamorphic data into a single, comprehensive interpretative model that constrains the pressure-temperature-deformation conditions responsible for the thrust emplacement of the Hajir Formation over the Mu'aydin Formation within a critical area of the tectonic window, known as the 'Little Snake Gorge,' as well as the development of aragonite veins exploiting the foliation formed during thrusting-related high-pressure metamorphism. Additionally, the study aims to develop a unified geodynamic framework that integrates the documented deformation features with the metamorphic history of the "Little Snake Gorge Thrust" to enhance the understanding of deformation structures linked to thrusting and vein development occurring under blueschist-facies conditions.

Following field investigations that focused on the structural delineation of the Little Snake Gorge section and the systematic acquisition of a comprehensive dataset of mesostructural features associated with the Little Snake Gorge Thrust, additional metamorphic analyses were conducted on carefully selected samples. In particular, Raman Spectroscopy on Carbonaceous Material (RSCM) led to the determination of peak metamorphic temperatures by analyzing the thermal alteration of microscopic graphite inclusions within representative rock specimens. Furthermore, the occurrence of metamorphic aragonite enabled the constraint of minimum pressure conditions associated with the RSCM-derived temperature estimates, based on the thermodynamic stability boundary between calcite and aragonite polymorphs.

Thus, this thesis presents new structural datasets, detailed microstructural analyses, and an integrated metamorphic investigation of the Little Snake Gorge Thrust. The extensive and systematic examination of this key tectonic contact is intended to enhance understanding of the geodynamic history of the latter, with a specific focus on the subduction-related deformation processes, such as thrusting and veining, that influenced this sector of the Jabal Akhdar Dome during Cretaceous times.

The outcome is the development of a comprehensive tectonic model that combines the newly acquired structural observations with the interpreted metamorphic signatures, aiming to enhance the regional scale understanding of the tectonometamorphic evolution of the Jabal Akhdar Dome. This, in turn, is used to provide deeper insights into the geological evolution of the Arabian passive margin.

OVERVIEW OF THE THESIS STRUCTURE

This section illustrates the organization of the thesis, summarizing each chapter to guide the reader through the research progression and its contribution to the study's main objectives. The thesis is organized as follows:

- To provide a clear and structured overview of the work conducted, the geological setting of the Oman Mountains is outlined in **Chapter 1**, starting from the broader context of the Arabian Plate and its complex geodynamic evolution from the Neoproterozoic to the Cenozoic. This is followed by a detailed examination of the established structural architecture of the Jabal Akhdar Dome and concludes with the report of previous studies focused on the Little Snake Gorge outcrop.

- In **Chapter 2**, the materials and methodologies employed are described, spanning from the field survey conducted in the Little Snake Gorge area to the petrographic examinations and metamorphic analyses carried out on the collected samples.

- The systematic review of all the results obtained from structural surveys as well as petrographic and Raman analyses is provided in **Chapter 3**, offering a comprehensive understanding of the heterogeneity within the local structural framework across the limited-scale study area.

- Results from fieldwork and metamorphic analyses are then integrated and discussed in **Chapter 4** to establish a plausible geodynamic model for the evolution of the Little Snake Gorge Thrust that reconciles all the acquired data; moreover, the outcomes have proven useful in improving our understanding of thrusting and veining processes under blueschist facies conditions, as well as in better constraining the metamorphic conditions of the Arabian passive continental margin during subduction phases.

- Finally, a summary of the work presented in this thesis is provided in **Chapter 5**, highlighting the new insights gained and the proposed interpretation of the results, and concluding with suggestions for potential future research directions.

CHAPTER 1 - GEOLOGICAL SETTING OF OMAN MOUNTAINS

The study area is in the Sultanate of Oman, located in the northeastern corner of the Arabian Plate, where convergence between the latter and the Eurasian plate is being presently accommodated by the subduction of the Gulf of Oman oceanic lithosphere below the Makran accretionary wedge and Eurasian continental lithosphere (Breton et al., 2004; Motaghi et al., 2020; Tavani et al., 2020).

The present-day boundaries of the Arabian Plate were primarily shaped and defined during the Oligocene, when the plate detached from the northernmost part of the African Plate. The relative northeastward translation and counterclockwise rotation of Arabia were driven by the subduction of the Tethyan oceanic lithosphere below Eurasia during the closure of the Neo-Tethys Ocean in the eastern Mediterranean region, along the NE margin of the Arabian Plate (Fournier et al., 2010; Augustin et al., 2014). Currently, the plate boundaries are defined to the northeast by the Makran subduction zone and by the Bitlis-Zagros mountain belt, to the northwest by the Dead Sea transform fault, to the south and southwest by the Red Sea and Gulf of Aden active spreading centers, and to the southeast by the Owen transform fault (Fig. 1) (Kopp et al., 2000; Vita-Finzi, 2001; Breton et al., 2004).

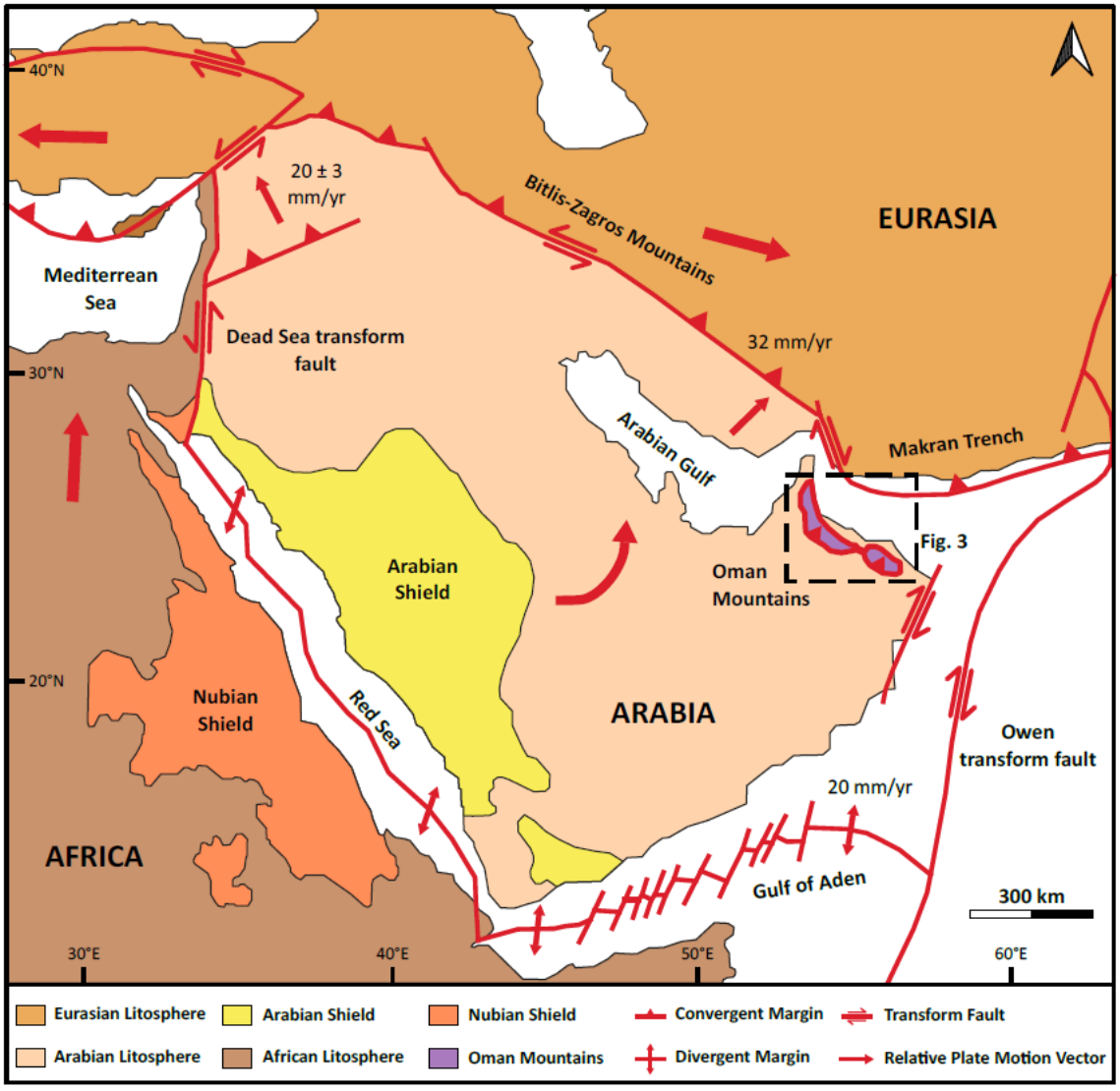

***Figure 1**: Simplified map of the Arabian Plate and its boundaries (redrawn and modified after Stern & Johnson, 2008).*

Several events have affected the tectonic evolution of the Arabian Plate (Fig. 2). NE-striking structural features, such as the Bir Umq and Yanbu sutures, were established during the Meso- to the Late Proterozoic Pan-African plate assembly, when island arcs and microcontinents were accreted to the western side of the Arabian Shield (Loosveld et al., 1996; Weidle et al., 2023).

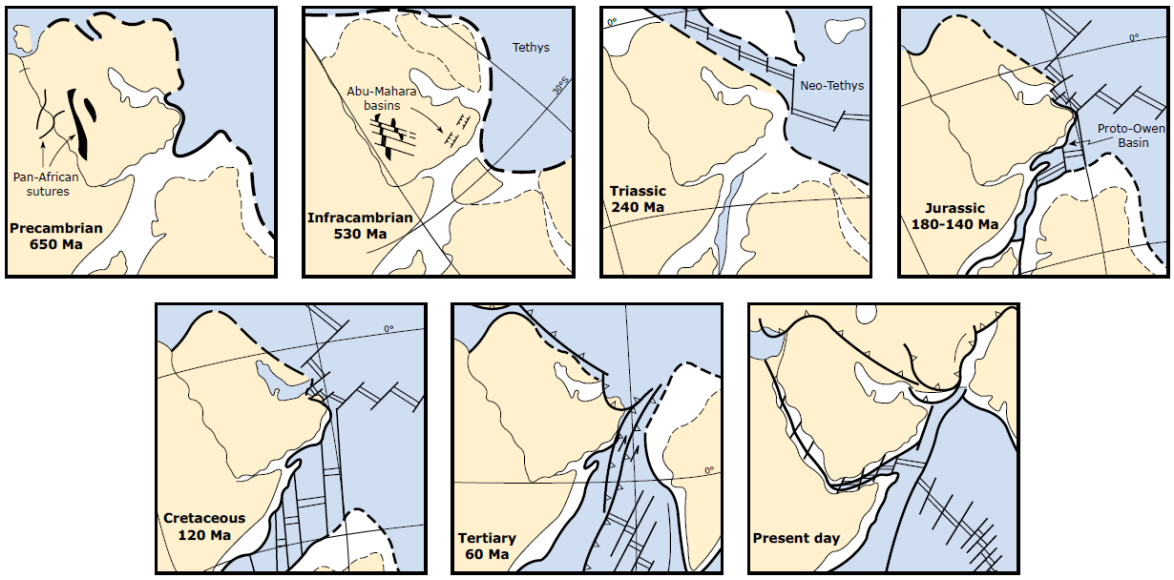

***Figure 2**: Simplified plate tectonic evolution of the Arabian Plate (modified after Loosveld et al., 1996).*

The Cryogenian was characterized by the formation of NE-SW trending basins and horst-and-graben structures during the Abu Mahara rifting phase (Loosveld et al., 1996). Later tectonic stages, following the Cryogenian rifting phase, consisted of regional subsidence due to thermal relaxation, eustatic sea level fluctuations, epeirogenic movements, and minor rifting events (Loosveld et al., 1996; Allen & Leather, 2006; Al-Husseini, 2014). Following subsidence, Cadomian and/or Angudan deformation-related structures in Eastern Arabia have been recently proposed to have formed during Ediacaran and Terreneuvian NE-SW compression (Callegari et al., 2020). The Pan-African-related structures were most likely reactivated during Cambrian to Ordovician extension (Loosveld et al., 1996).

The Caledonian (Cambrian-Devonian) and the Hercynian (Devonian-Permian) orogenies occurred at great distances from Arabia, and correlation between the latter and these two major deformation events can be far-fetched since it implies that far-field stresses were transmitted over thousands of kilometres to the Arabian lithosphere (Ruban et al., 2007). Even if the Hercynian orogeny was initially identified as the possible source of regional upwarps, sags, narrow N-trending basement cored uplifts, and eventual larges cale arch formation and block faulting in Eastern Arabia (Konert et al., 2001), such evidence has been recently correlated to the Middle Silurian breakaway from Gondwana of the Hun Superterrane, which extended from westernmost Iberia to Qiantang (Ruban et al., 2007), while the Hercynian orogeny has been recognized solely as a cause of thermal variations within the Arabian Plate (Abbo et al., 2018; Callegari et al., 2020).

Two rift axes formed due to the Permian breakup of Pangea, leading to the current geometry of the plate's eastern and northern passive margins. The present-day geology of Eastern Arabia has evolved through a complex sequence of geological and tectonic processes, culminating in the SW-directed obduction of a slice of Tethyan oceanic lithosphere, known as the Semail Ophiolite, during the Late Cretaceous (Loosveld et al., 1996; Weidle et al., 2023), followed by post-obduction doming during the Cenozoic Era (Gomez-Rivas et al., 2014).

From the Late Permian throughout the Mesozoic, Oman formed part of a wide carbonate platform at the southern passive continental margin of the Tethys (Mann & Hanna, 1990; Searle, 2007). At least one subduction zone is thought to have developed in the Tethyan ocean during the Late Cretaceous. While moving progressively northwards, the Arabian Plate entered this subducting zone, eventually experiencing overthrusting by the obducting Semail Ophiolite. Additionally, the subduction led to the imbrication of deep oceanic and slope sediments, the Hawasina Complex and the Sumeini Group, respectively, deposited initially on the Oman continental margin (Mann & Hanna, 1990; Searle, 2007; Carminati et al., 2020).

The northern Oman Mountains, or Al Hajar Mountains (Arabic for 'rock'), stretch for approximately 700 km from the Musandam Peninsula in the north to the Batain coast in the southeast (Fig. 3). They form a crustal-scale anticline, with a width between 40 and 150 km (Glennie et al., 1973; Mann & Hanna, 1990; Breton et al., 2004; Grobe et al., 2018; Tavani et al., 2020). Their maximum elevation of approximately 3000 m is at the Jabal (Arabic for 'mountain') Shams peak, located in the Jabal Akhdar Dome (Glennie et al., 1973). Since continental subduction was not followed by collision, the Oman Mountains represent one of the best-preserved examples of obducted ophiolitic complexes and continent-ocean convergent boundaries (Agard et al., 2010).

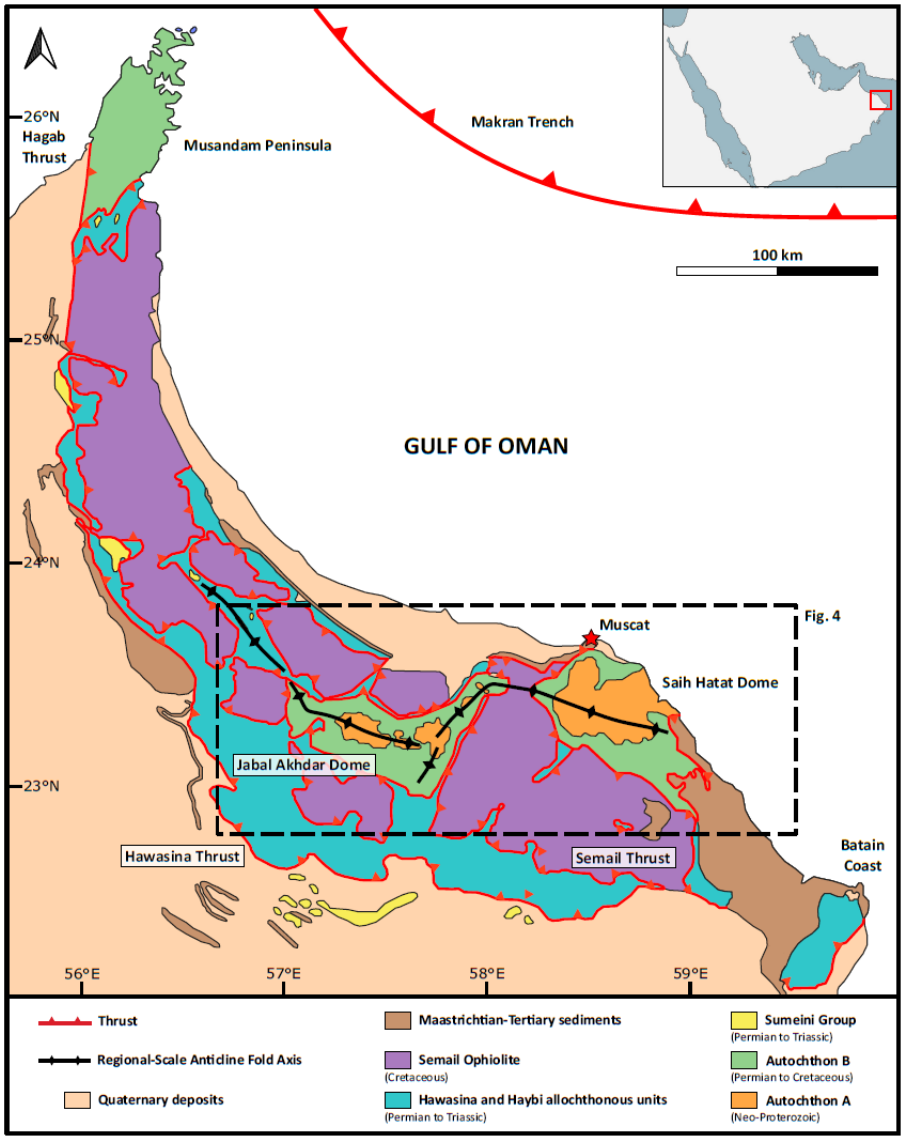

***Figure 3**: Simplified map of the Oman Mountains and of the main lithostratigraphic units (redrawn and modified after Searle, 2007, and Deif et al., 2018).*

The mountain belt consists of a SW-verging nappe stack containing allochthonous sedimentary and ophiolitic nappes obducted onto the autochthonous Mesozoic passive continental margin of the Neo-Tethys (Grobe et al., 2018; Carminati et al., 2020). Stacking occurred prior to and during the SW-directed Late Cretaceous ophiolite obduction. Cenozoic tectonics further shaped the stack (Carminati et al., 2020; Tavani et al., 2020). The bottom of the thrust pile includes Neoproterozoic metasediments, which are unconformably overlain by Permian to Mesozoic sediments of the Arabian passive margin (e.g., Carminati et al., 2020). Shallow-water sedimentation along the continental passive margin continued up to the Turonian and, after a period of non-deposition, was succeeded by foredeep sedimentation during the Coniacian-Santonian. During the Late Cretaceous, these sediments were overridden by multiple thrust sheets consisting of Late Permian to Cretaceous deep-water carbonates, sandstones, turbidites, and cherts from the Hawasina complex, and obducting ophiolitic upper mantle peridotites, overlying gabbros, trondhjemites, sheeted dykes, pillow lavas, and pelagic sediments from the Semail Ophiolite (Glennie et al., 1973; Mann & Hanna, 1990; Carminati et al., 2020).

Historically, the Oman Mountains' rock record has been subdivided into four major units (e.g., Glennie et al., 1974; Robertson & Searle, 1990; Gregory et al., 1998; Breton et al., 2004; Deif et al., 2018; Grobe et al., 2018), which, from bottom to top, are:

- Autochthon A: Precambrian units exposed in Jabal Akhdar and Saih Hatat Domes.
- Autochthon B: carbonate-dominated sequence deposited from the Middle Permian to the Late Cretaceous on the continental shelf of the Arabian passive margin.
- Allochthonous units: deeper water sediments of the Hawasina nappes, slope deposits of the Sumeini Group, the Semail ophiolite complex, and the serpentinitic melange, limestones, metavolcanic and metamorphic sole rocks of the Haybi Complex.
- Post-ophiolite Maastrichtian to Quaternary neo-autochthonous sediments.

Two tectonic windows, the Jabal Akhdar and Saih Hatat Domes, represent the principal structural features of the internal Oman Mountains, exposing the imbricated thrust sheets overlying the Precambrian basement rocks (e.g., Hanna, 1990). They are separated by the so-called Semail Gap, a complex and multiply reactivated NNE-trending fault zone (Fig. 4) (Scharf et al., 2019).

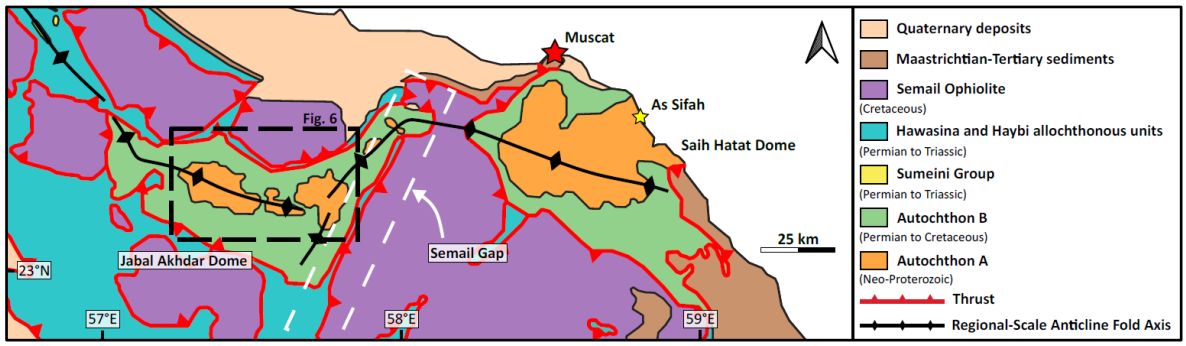

***Figure 4**: Schematic map of the Jabal Akhdar and Saih Hatat domes (redrawn and modified after Searle, 2007, and Deif et al., 2018).*

Several models have been proposed to explain the formation of the Semail Gap. Initially, it has been suggested that the Semail Gap is a collapse structure formed during and/or after the Cenozoic doming in the Jabal Akhdar Dome (Robertson, 1987; Hanna, 1990) or, alternatively, a sinistral strike-slip fault that initially existed along the Semail Gap even before or at an early stage of the Late Mesozoic obduction (Le Metour et al., 1990). The Semail Gap has been also interpreted as a NW-dipping blind thrust (Mount et al., 1998), an S-shaped listric normal fault with no significant lateral offset (Searle, 2007), or a lateral ramp within a crustal-scale blind thrust system south of the Jabal Akhdar Dome (Hansman et al., 2017). More recent models propose it as a dextral transtensional fault active during late Eocene-Miocene gravitational collapse (Scharf et al., 2021), or as a major transfer zone reactivating a Pan-African suture, active during ophiolite obduction and separating two offshore domains with distinct obduction histories (Ninkabou et al., 2021).

Previous studies report that the entire rock sequence, as exposed within the Jabal Akhdar and Saih Hatat Domes, records a structural and metamorphic gradient, increasing in intensity toward E and NE (Le Metour et al., 1990; Mann & Hanna, 1990; Breton et al., 2004), confining the highest tectonic strain and metamorphism to the north-eastern part of the Saih Hatat area: crossite blueschist facies characterizes the northernmost part of the dome, passing to almandine blueschist facies metamorphism and glaucophane eclogite facies near As Sifah (Breton et al., 2004). Differently, the highest metamorphic grade within the Jabal Akhdar dome has been constrained to the pumpellyite and epidote greenschist facies (Le Metour et al., 1990; Breton et al., 2004). However, recent studies have documented greenschist-facies metamorphic conditions affecting the Permian rocks in the western sector of the Jabal Akhdar Dome (Degl'Innocenti, 2024), as well as the occurrence of high-pressure metamorphic aragonite within Precambrian rocks in the central part of the tectonic window, linking its formation to blue schist facies conditions (Zuccari et al., 2023).

The description of the Jabal Akhdar Dome autochthonous stratigraphic sequence provided here below is arranged from oldest to the youngest and sets the scene for this study. The crystalline basement is known to be composed of several NNE-striking terranes, which were accreted during the Neoproterozoic. Major terrane boundaries run parallel to the Semail Gap and were likely reactivated during the Neoproterozoic and Phanerozoic (Weidle et al., 2023). The basement, however, only crops in the southeastern part of the mountain chain, and it is characterized by igneous and metamorphic rocks on top of which rests the sedimentary succession (Breton et al., 2004). In the Jabal Akhdar Dome the metamorphic basement is not exposed. The oldest rocks therein belong to the glaciogenic Mistal Formation. They most likely deposited during the Cryogenian Abu Mahara rifting event (Loosveld et al., 1996). This diamictitic unit is generally explained by the Snowball Earth theory, which envisages a series of paleoclimatic oscillations during the Neoproterozoic. the planet's climate changed significantly, alternating periods of time when much of the Earth's surface was frozen and unusually warm intervals (Stern et al., 2006). Geochronological analyses have linked the Mistal Formation at the base of the exposed succession with two events related to the Snowball Earth hypothesis, the Sturtian (715-680 Ma) and Marinoan (660-635 Ma) glacial epochs (Brasier et al., 2000; Leather et al., 2002; Le Guerroué et al., 2005; Stern et al., 2006). The subsequent deposition of the overlaying Ediacaran formations was most likely controlled by a phase of regional subsidence following the Abu Mahara rifting stage (Loosveld et al., 1996; Allen & Leather, 2006; Al-Husseini, 2014). These Precambrian formations comprise the black fetid limestones of the Hajir Formation, the siltstones and calcareous mudstones of the Mu'aydin Formation, the stromatolites and chert-rich limestones and dolomites of the Kharus Formation, and the conglomerates, sandstones, siltstones, ignimbritic volcanic rocks, and tuffites of the Fara Formation (Beurrier et al., 1986; Rabu et al., 1986).

The Mesozoic carbonate-dominated stratigraphic sequence, which accumulated on the Arabian passive margin's continental shelf during the opening of the Neo-Tethys Ocean, is separated by the Precambrian units by the so-called “Hercynian Unconformity”, a c. 265 Ma stratigraphic gap within the Jabal Akhdar geological record (Konert et al., 2001; Callegari et al., 2020; Scharf et al., 2021).

From the Late Carboniferous to the Early Permian, the Cimmerian continental blocks progressively rifted away from the northern margin of Gondwana, leading to the formation of the Neo-Tethys Ocean (Stampfli & Borel, 2002; Scharf et al., 2021; Zhu et al., 2022). The break-up of Gondwana led to the formation of two basins in the North Oman passive Neo-Tethys continental margin, thus creating space for the deposition of continental shelf and pelagic units: the older Batain Basin, which opened between the Arabian and Indian plates, and the younger Hawasina Basin, which opened between Gondwana and the Cimmerian blocks (Robertson & Searle, 1990; Scharf et al., 2021).

The drifting of the Cimmerian superterrane during the late Early Permian initiated the formation of new oceanic crust in the Neo-Tethys Ocean, which later began to subduct beneath the Cimmerian blocks in the Early Jurassic (Stampfli & Borel, 2002; Pilia et al., 2021). Seafloor spreading continued until at least the mid-Cretaceous, while the shelf carbonate successions of the Autochthon B sedimented and the North Oman passive margin became a mature carbonate-dominated rifted margin (Robertson & Searle, 1990; Agard et al., 2010; Pilia et al., 2021).

The Valanginian rotation of east Gondwana with respect to Africa induced a WNW-ESE-directed compressional regime in the Neo-Tethys Ocean (Stampfli & Borel, 2002). The consequent convergent stresses induced the shortening stage that shaped the present-day geology of Eastern Arabia and the Oman Mountains (Loosveld et al., 1996; Weidle et al., 2023).

Four evolutionary sub-stages can be identified:

- 104 - 96 Ma: The first stage of subduction was probably induced by the far-field stresses generated by east Gondwana rotation (Guilmette et al., 2018; Tavani et al., 2020). This led to intra-oceanic subduction in the Neo-Tethys northeast of the Oman passive margin, most likely along a paleo-transform fault acting as a weak, pre-existing structure (Robertsone & Searle, 1990; Loosveld et al., 1996; Stampfli & Borel, 2002; Guilmette et al., 2018; Tavani et al., 2020). The debate regarding the direction and the number of the subducting slabs is still ongoing. Even if generally accepted models involve a single NE-verging subduction (e.g., Le Metour et al., 1990; Mann & Hanna, 1990; Robertson & Searle, 1990; Searle & Cox, 2002; Tavani et al., 2020; Weidle et al., 2023), other studies have proposed an earlier SW-verging subducting slab (e.g., Gregory et al., 1998; Gray & Gregory, 2000; Boudier & Nicolas, 2018, Degl’Innocenti, 2024) or even a two-fold subducting system (e.g., Goscombe et al., 2020; Ring et al., 2023). Nevertheless, following its initiation by far-field stresses, subduction most likely transitioned into a self-sustaining phase between 104 and 96 Ma. (Guilmette et al., 2018; Tavani et al., 2020).

- 96 - 94 Ma: The sinking of the slab down to c. 35 km depth triggered trench retreat, back-arc extension, and calc-alkaline magmas production, inducing oceanic lithosphere generation along a supra-subduction zone spreading center (Guilmette et al., 2018; van Hinsbergen et al., 2019; Goscombe et al., 2020; Tavani et al., 2020; Rioux et al., 2021; Scharf et al., 2021). The Semail Ophiolite formation began around 95 Ma, concurrently with upper-plate extension in the supra-subduction zone (Lachize et al., 1996; Warren et al., 2005; Guilmette et al., 2018; Tavani et al., 2020; Rioux et al., 2021). A metamorphic sole formed at or slightly prior to the oceanic lithosphere formation (Rioux et al., 2021; Scharf et al., 2021), and, simultaneously, the Semail Ophiolite started its obduction above the Hawasina Basin (Scharf et al., 2021). Alternative models proposed the existence of two subduction zones at the mid-Cretaceous Arabian rifted margin, the outboard Semail subduction zone and the inboard, intracontinental Ruwi subduction zone. Contrasting thermal conditions, along with Rb-Sr multimineral ages for HP metamorphism in the Saih Hatat Dome, suggest that the Ruwi subduction zone was the first to form but that both regional-scale convergence and Saih Hatat HP metamorphism were accomplished by the latter (Ring et al., 2023).

- 94 - 70 Ma: The obduction initiation of the Semail Ophiolite resulted in a flexural forebulge moving through the Arabian passive margin (Grobe et al., 2018). This event marked the termination of stable sedimentation on the northern Arabian platform around 90 million years ago, as the passive margin was down warped to create the Aruma foreland basin (Warburton et al., 1990). The ophiolites, along with the metamorphic sole, were emplaced over the Hawasina Complex, and transported southwestward for at least 450 km (Agard et al., 2010; Scharf et al., 2021). The ophiolitic complex was subjected to a clockwise rotation from its formation to its emplacement above the Arabian autochthonous units (van Hinsbergen et al., 2019). The Hawasina nappes were imbricated and partly truncated by later out-of-sequence thrusting within the ophiolite (Sharf et al., 2021). Peak metamorphism of the subducted Arabian margin occurred during the deepest burial under the ophiolite at around 79 Ma, when the rocks now cropping out in the Saih Hatat area were subjected to blue schist and eclogitic facies metamorphism while being subducted to a minimum depth of 80 km (Warren et al., 2003, 2005; Grobe et al., 2018; Scharf et al., 2021). Between 88 and 70 Ma, tectonic slices of the Hawasina and Haybi complexes and of the Semail ophiolite were emplaced on top of the shelf carbonates (Loosveld et al., 1996; Agard et al., 2010).

- 70 - 66 Ma: The emplacement of the Semail Ophiolite onto the Arabia passive margin was completed during the Maastrichtian (Scharf et al., 2021). Buoyant crustal rocks jammed the subduction zone, causing possible slab break-off, while the Arabian crust within the subducting slab, including the Saih Hatat metamorphic rocks, was intensively and repeatedly folded during exhumation and ongoing convergence (Agard et al., 2010; Scharf et al., 2021). Post-peak metamorphic exhumation of the As Sifah eclogites occurred by return flow, which was enabled by NNE-dipping normal-sense shear zones and bottom-to-SSW active footwall extrusion (Agard et al., 2010; Grobe et al., 2018). This was related to the tectonic thinning of the ophiolite and to the formation of a precursor to the Jabal Akhdar Dome (Grobe et al., 2018). Here, the final exhumation stage was accomplished along NE-SW to NW-SE striking brittle faults cutting across the ductile shear zones and forming horst-graben structures (Agard et al., 2010; Grobe et al., 2018).

Late Cretaceous deformation ceased abruptly when a different subduction zone developed in the north, giving rise to the present-day Makran subduction zone (Loosveld et al., 1996). There, the Neo-Tethys subduction below the Iranian Plate continued until the end of the Eocene, when the Arabia-Eurasia continental collision led to the formation of the Zagros fold-and-thrust belt (Molinaro et al., 2005; Mouthereau et al., 2012). The Jabal Akhdar and Saih Hatat domal structures remained beneath sea level until the late Eocene. Recent studies support thermal thinning of the lithosphere rather than NE-SW-directed shortening to explain the Late Eocene uplift of the Oman Mountains because the latter and the rapid cooling in the Jabal Akhdar Dome started circa 10 Ma before the formation of the Zagros Mountains (Scharf et al., 2021; Weidle et al., 2023). Consequently, localised uplift led to the emergence of the two domes and the ophiolite to the surface regardless of the convergence between the Arabian and Eurasian plates (Weidle et al., 2023). In the western Jabal Akhdar, bedding has been tilted during doming, leading to the box-fold shape of the Jabal Akhdar Dome (Grobe et al., 2018).

Mountain-building mostly occurred during the second Alpine event, from the Oligocene to the Pliocene, when the Oman Mountains were uplifted until collapse and the development of major extensional structures, which partially exploited and reactivated the structural features initially formed during obduction (Loosveld et al., 1996; Gomez-Rivas et al., 2014; Grobe et al., 2018).

Deformed Quaternary alluvium, stepped fluvial terraces, and wadis (Arabic for ‘valley’ or ‘riverbed’) in the Jabal Akhdar Dome are attributed to the reactivation of several faults. All wadis exhibit a relatively recent incision of tens of metres or more, testifying to the ongoing uplift of the Oman Mountains; this is most likely related to isostatic rebound in response to flexural bulging and/or erosion of thick and dense allochthonous units, both contributing to the final geometry of the Jabal Akhdar Dome (Scharf et al., 2021).

1.1 - LITHOSTRATIGRAPHY OF THE JABAL AKHDAR DOME

The Jabal Akhdar Dome lithostratigraphy is mainly characterised by (meta)sedimentary units, spanning from Neoproterozoic to Quaternary in age. The autochthonous formations of the Arabian passive margin, subdivided in Autochthonous A and B, are presently overlain by the obducted Hawasina Nappes and Semail Ophiolite (Fig. 5), both initially belonging to the Neo-Tethys domain (e.g., Mann & Hanna, 1990; Searle, 2007).

Since the allochthonous units are not the focus of this thesis, they are not included in the following summary. Even though the tectonic window exposes a stratigraphic succession spanning from 720 Ma ago to the present, the sequence is interrupted by an angular unconformity, called the “Hercynian Unconformity”, a significant hiatus of more than 250 Ma in the Jabal Akhdar geological record, which juxtaposes Early Paleozoic rocks of the Autochthonous A below against Middle Permian sedimentary units of the Autochthonous B above.

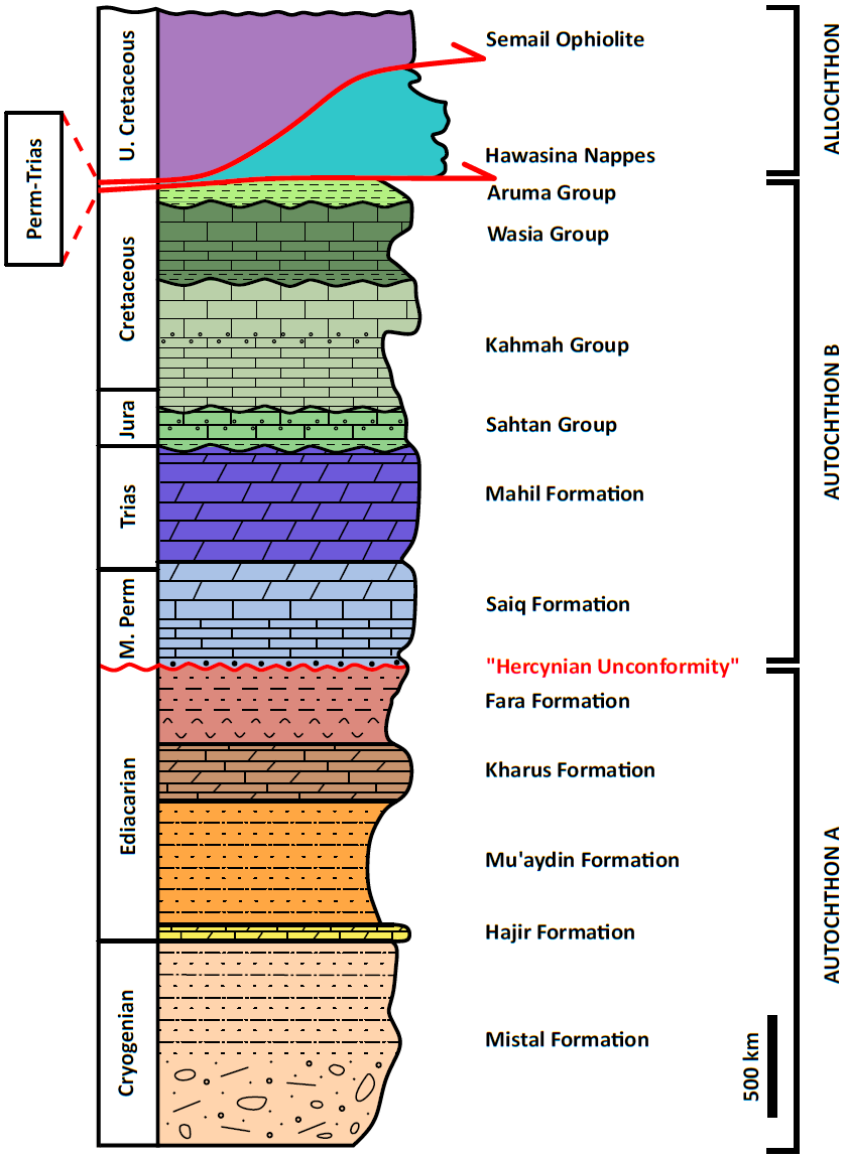

Figure 5: Lithostratigraphic column of the Jabal Akhdar Dome (redrawn and modified after Aldega et al., 2017, and Zuccari et al., 2021).

Initially, considerations on crystallization ages and WSW-ENE to SSW-NNE-oriented folds, led to interpretations of this hiatus as related to the Hercynian Orogeny (Konert et al., 2001; Callegari et al., 2020). Nonetheless, this explanation is debatable due to the considerable separation between the Arabian Plate and the Gondwana-Laurasia collision zone in the Late Paleozoic (Ruban et al., 2007; Callegari et al., 2020). Moreover, recent studies have interpreted the "Hercynian event" influence in Arabia as only capable to cause thermal oscillations (Abbo et al., 2018; Callegari et al., 2020). Later interpretations have identified the exhumation associated with the break-off of the Cimmerian blocks from Gondwana (Ruban et al., 2007; Callegari et al., 2020) or the tilting and block faulting generated by the Neo-Tethys rift opening as the cause for the stratigraphic hiatus (Scharf et al., 2021). Alternatively, evidence of tectonic movements along the unconformity surface, such as shearing and tectonic brecciation of both the Autochthonous A and B units, has led to the interpretation of the Hercynian Unconformity as a re-activated stratigraphic contact, which does not obey the "thrust tectonic rule", with younger middle Permian rocks being thrusted over older Precambrian units (Mann & Hanna, 1990; Degl'Innocenti, 2024).

The Neoproterozoic Autochthonous A has been subdivided into the Mistal, Hajir, Mu'aydin, Kharus, and Fara Formations, which have been correlated with the Huqf Supergroup of central and eastern Oman (Allen et al., 2007). It mainly comprises metamorphosed siliciclastic and carbonate rocks, with less abundant volcanic units. A description of each formation, from oldest to youngest, is provided below:

- **Mistal Formation (Cryogenian)**: It is the oldest formation in the Jabal Akhdar Dome, often correlated with the formations of the Abu Mahara Group in the subsurface and is divided into the Ghubrah, Saqlah, Fiq, and Amq members (e.g., Brasier et al., 2000; Allen, 2007; Scharf et al., 2021). Its thickness ranges between c. 1000 to 1500 m, and it comprises diamictites with granite boulders, sandstones, pinkish siltstones, graywackes, dolomites, and pillow lavas (Beurrier et al., 1986; Rabu et al., 1986), which deposited during the Cryogenian Abu Mahara rifting phase (Loosveld et al., 1996; Allen & Leather, 2006; Al-Husseini, 2014). Geochronological analysis dated the Mistal Formation to between c. 713 and 640 Ma (Bowring et al., 2007; Allen et al., 2011), linking the diamictitic Ghubrah and Fiq members with the Sturtian (715-680 Ma) and Marinoan (660-635 Ma) glacial epochs, respectively, which occurred during the Snowball Earth event (Brasier et al., 2000; Leather et al., 2002; Allen et al., 2004; Le Guerroué et al., 2005; Stern et al., 2006).

- **Hajir Formation (Ediacaran)**: It is characterized by black, thin to medium thick dolomitic limestones rich in organic matter and sulphur (Beurrier et al., 1986; Rabu et al., 1986). It most likely deposited in a restricted lagoon or in the distal environment of a prograding ramp (Scharf et al., 2021), between c. 610 and 582 Ma (Le Guerroué et al., 2006; Al-Husseini et al., 2014). From a maximum thickness of c. 100 m within the Jabal Akhdar Dome, the formation tends to disappear toward the W and NW of the tectonic window, truncated by the Hercynian Unconformity. (Scharf et al., 2021). The type of contact between the Hajir Formation and the overlaying Mu'aydin Formation is still under debate since sedimentation along their contact has been interpreted as either continuous (Le Guerroué et al., 2009; Scharf et al., 2021) or discontinuous (Scharf et al., 2021). Additionally, recent studies identified syn-sedimentary extensional faults at the contact, probably related to extensional movements along a precursor of the Semail Gap Fault Zone (Mattern & Scharf, 2019).

- **Mu'aydin Formation (Ediacaran)**: This formation, with a thickness ranging from 800 to 900 m, is characterized by green and reddish siltstones and is subdivided into three members. The lower member is represented by a 2-3 m thick, dark, quarzitic sandstone layer, overlain by 40-50 m of alternating thick reddish-brown sandstones and soft violet siltstones. The middle member contains greenish to soft violet, mica-rich siltstones. The upper member consists of micaceous siltstones interbedded with white limestone; the latter defines the transition with the overlying Kharus Formation (Beurrier et al., 1986; Rabu et al., 1986). Similarly to the subjacent Hajir Formation, it tends to disappear toward the NE of the Jabal Akhdar Dome (Allen, 2007; Scharf et al., 2021). The paleoenvironment of the Mu'aydin Formation has been interpreted as a distal siliciclastic shelf deposit (Le Guerroué et al., 2006), where its members probably deposited between c. 582 and 561 Ma (Al-Husseini et al., 2014). However, as mentioned above, the presence of a hiatus between the Hajir and Mu'aydin Formations is still uncertain (Scharf et al., 2021).

- **Kharus Formation (Ediacaran)**: It is defined by dark limestones and dolomites rich in organic matter, alternated with silicified stromatolites (Beurrier et al., 1986; Rabu et al., 1986; Cozzi & Al-Siyabi, 2004). Its depositional setting is interpreted as an intertidal to supratidal carbonate platform (Scharf et al., 2021) or as a distally steepened storm-dominated carbonate ramp (Cozzi et al., 2004; Scharf et al., 2021). This c. 245 m thick formation has not been properly dated yet, even if constraints from the subsurface equivalent of the Huqf Supergroup define a range between c. 561 and 547 Ma (Bowring et al., 2007; Al-Husseini et al., 2014).

- **Fara Formation (Ediacaran)**: It overlies the Kharus Formation in apparent conformity and is truncated by the Hercynian Unconformity (e.g., Scharf et al., 2021). This c. 380 m thick formation has been subdivided into three members. The lower member consists of black chert interbedded with gray dolomite, with layers of silicic tuff in its upper part. The phosphate-rich, middle member contains conglomerates, breccias, sandy limestones, siltstones, sandstones, and stromatolites. The upper member contains quartzitic and gray to greenish argillaceous siltstones, sandstones, cemented conglomerates, graywackes, and green silicic tuffites (Beurrier et al., 1986; Rabu et al., 1986). The transition from the stromatolite-rich rocks of the younger Kharus Formation to the chert deposits of the lower member of the Fara Formation suggests the deepening of the basin (Allen, 2007; Bowring et al., 2007). Ages obtained with the U-Pb zircon method allowed the formation to be dated between c. 547 and 542 Ma (Bowring et al., 2007).

The Autochthonous B, or Hajar Supergroup, has been subdivided into the Saiq and Mahil Formations and the Sahtan, Kahmah, Wasia, and Aruma Groups, spanning from the Middle Permian to the Late Cretaceous (Gregory et al., 1998). This carbonate-dominated sequence accumulated on the Arabian passive margin's continental shelf during the rifting phase linked to the Neo-Tethys Ocean rifting. A description of the formations and groups, from oldest to youngest, is provided below:

- **Saiq Formation (Roadian-Changhsingian)**: This formation comprises siliciclastic, carbonate, and volcanic rocks and is divided into two members. The lower member consists of a c. 25 m thick unit of siltstones, conglomerates, sandy limestones, felsic volcaniclastics, and volcanic rocks. The upper member has a thickness of c. 425 m and is composed of shallow-marine, fossil-rich, dark limestones and dolostones (Beurrier et al., 1986; Rabu et al., 1986). The Saiq formation deposited during the Middle Permian rifting phase of the Neo-Tethys Ocean opening, and it has been dated to between the Roadian and the Changhsingian (Koehrer et al., 2012; Scharf et al., 2021).

- **Mahil Formation (Changhsingian-Olenekian)**: This c. 600 m thick formation mainly consists of gray or yellowish dolostones, deposited during the syn- and post- Neo-Tethys Ocean rifting (Beurrier et al., 1986; Rabu et al., 1986). The origin of the contact between this and the Saiq Formation is still under debate. However, based on colour differences and micropaleontological studies on the disappearance of fossils related to the Late Changhsingian ‘Great Dying’ extinction event (Baud et al., 2010), the Mahil Formation can be dated as ranging from the uppermost Permian to the Olenekian (Koehrer et al., 2012; Scharf et al., 2021).

- **Sahtan Group (Hettangian-Callovian)**: This group, which rests unconformably on the Mahil Formation, has been dated to between the Hettangian and the Callovian (Scharf et al., 2021), and has been divided into the Mafraq and Dhruma Formations, reaching a total thickness between 400 m in the W and 80 m toward E (Beurrier et al., 1986; Rabu et al. 1986). The lower Mafraq Formation represents a terrigenous interruption formed in shallow-marine, tidal flat, coastal bar sands, and estuarine systems (Scharf et al., 2021). It is characterized by shallow-marine sandstones, micaceous siltstones, and bioclastic argillaceous limestones (Beurrier et al., 1986; Rabu et al., 1986). Differently, the Dhruma Formation consists of massive shallow-marine limestones deposited in a low-energy carbonate platform dominated by lagoonal mud- and wackestones in the lower part and by higher-energy facies, such as grainstones, toward the top (Scharf et al., 2021).

- **Kahmah Group (Tithonian-Aptian)**: The boundary between this group, dated between the Tithonian and the Aptian, and the younger Sahtan Group is marked by another unconformity. The Kahmah Group has been subdivided into the Rayda, Salil, and Shams Formations (Scharf et al., 2021). The 30 m thick Rayda Formation consists of silicified, whitish, micritic limestones deposited in an offshore to bathyal environment. The up-to-350 m thick Salil Formation is defined by alternating clayey-cherty marls and limestones, which become micritic and blackish toward the top, deposited in a subtidal to bathyal paleoenvironment. The Shams Formation, thick c. 450 m, contains different fossil-rich carbonate units associated with platform margin facies (Beurrier et al., 1986; Rabu et al., 1986).

- **Wasia Group (Aptian/Albian-Turonian)**: This group, dated to between the Aptian-Albian and Turonian, unconformably overlies the Kahmah Group and comprises the Nahr Umr and the Natih Formations (Scharf et al., 2021). The up-to-200 m thick Nahr Umr Formation deposited in a proximal subtidal platform and consists of black limestones alternating with thick beds of fossiliferous marls, characterized by a significant clastic terrigenous fraction. The c. 200 m thick Natih Formation disappears toward the NE of the Jabal Akhdar Dome, and it is characterized by the alternation of marly and pure limestones, suggesting a fossil-rich ramp as the depositional setting (Beurrier et al., 1986; Rabu et al., 1986).

- **Aruma Group (Coniacian-Maastrichtian)**: Dated between the Coniacian and the Maastrichtian, this group rests unconformably above the Wasia or older groups (Scharf et al., 2021). The up to 3.5 km thick Aruma Group contains the sediment filling that have accumulated in the flexural foreland basin in front of the obducting Semail Ophiolite, as well as post-obduction formations (Searle, 2007; Scharf et al., 2021). It is commonly divided into five formations (Scharf et al., 2021); however, in the Jabal Akhdar area, only the Muti Formation outcrops, characterized by yellowish siltstones, reef limestones, and turbidites, reflecting a subtidal carbonate platform (Beurrier et al., 1986; Rabu et al., 1986).

1.2 - STRUCTURAL SETTING OF THE JABAL AKHDAR DOME

Despite some studies dealing with the first-order geological framework of the Jabal Akhdar Dome (Fig. 6), the latter remains poorly explored and understood together with its > 700 Ma-long geological evolution.

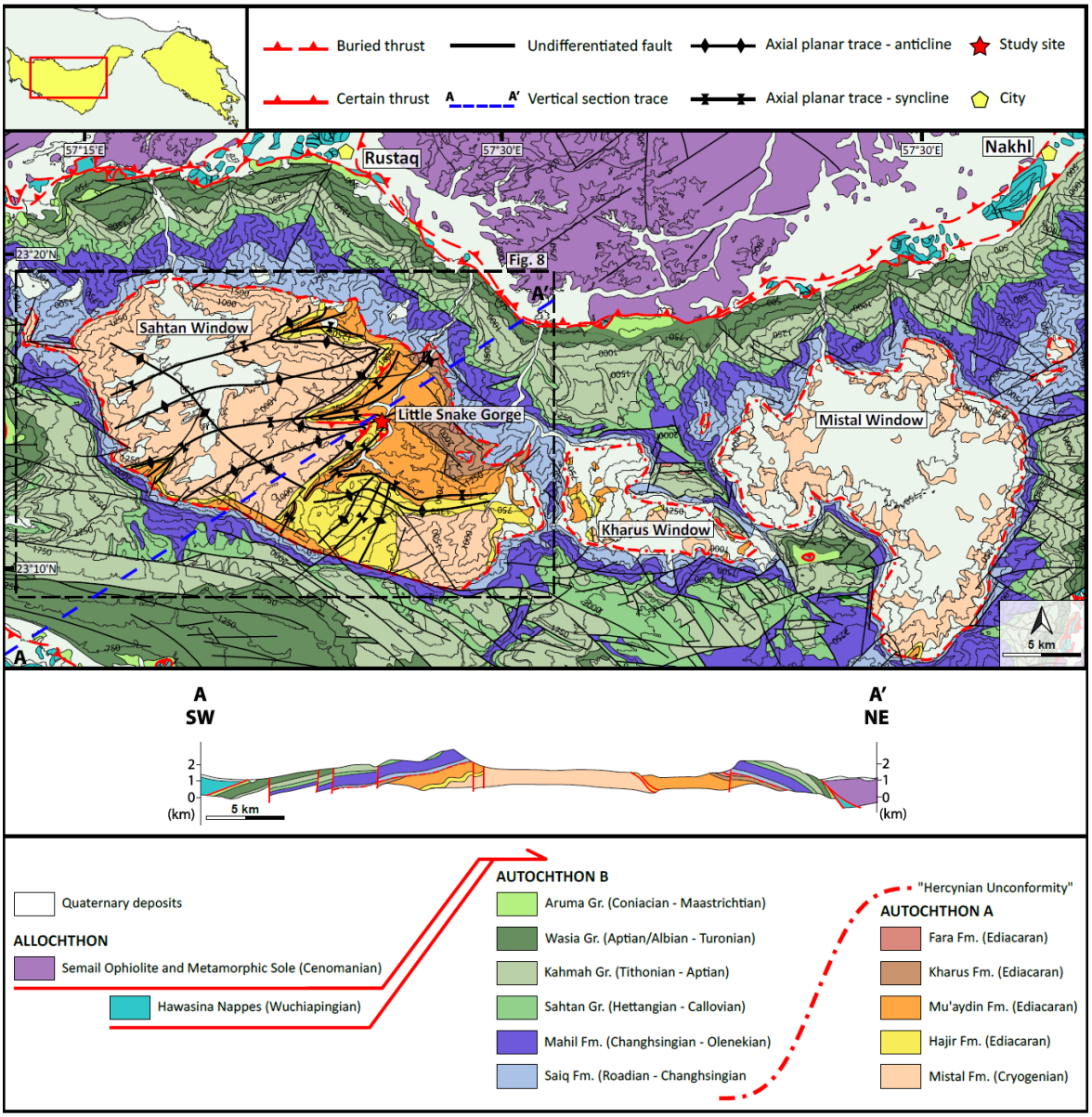

***Figure 6**: Geological map of the central and westernmost Jabal Akhdar Dome (redrawn and modified after Scharf et al., 2021).*

The Jabal Akhdar Dome is the largest tectonic window within the Oman Mountains, comprising the pre-Cambrian stratigraphic sequence of the Autochthon A that is unconformably overlain by the c. 2.5 km thick succession of the Permian to Cretaceous Autochthon B carbonate units (Zuccari et al., 2023). It consists of a 60 km wavelength anticline plunging to the NE beneath the Hawasina Window and is characterized by flexure flanks parallel to the various directions of its borders (Searle, 2007; Gomez-Rivas et al., 2014).

It comprises a principal structural dome with a WNW-ESE-trending fold axis, encompassing, from west to east, the Sahtan, Kharus, and Mistal Windows (Fig. 6), along with the NNE-SSW-oriented Nakhl Subdome, which is attached to the northeasternmost margin of the main dome (Mann & Hanna, 1990; Searle, 2007; Scharf et al., 2021).The northwestern part of Jabal Akhdar is, instead, defined by a symmetrical NW-SE-trending antiform, characterized by a subvertical axial plane and involving deformation of both the Autochthon B units and the overlying allochthonous nappes (Beurrier et al., 1986).

One or more distinct sets of cleavage have been documented within the Jabal Akhdar Dome, and different authors have proposed various interpretations as to the number and origin of the cleavage sets in the study area. Early investigations identified a subhorizontal, anastomosed fracture cleavage, generally referred to as "S_1," that extends from the southwestern margin of the Jabal Akhdar Dome and affects most of its surface area (Beurrier et al., 1986; Le Métour et al., 1990). This fracture cleavage has been described as associated with NE-verging asymmetric folds and C-planes at approximately 15-30° to the S1 itself. Additionally, the intersection between S_1 and the C-planes has been reported as consistently indicating a top-to-NE shearing, defined by the lineation of clasts, pebbles, and asymmetrical pressure-shadows extension (Le Métour et al., 1990). Furthermore, a well-developed schistosity fabric has been observed in the northeastern part of the tectonic window (Rabu et al., 1986; Le Métour et al., 1990).

Differently, Mann & Hanna (1990) identified a NE-SW-directed axial planar cleavage, steeply dipping toward NW and SE, referred to as, again, "S_1". Furthermore, a second, subhorizontal, S to SW-dipping cleavage, referred to as "S_2," was identified as cutting through the earlier S_1 (Mann & Hanna, 1990). The latter has been linked to Late Cretaceous deformation, implying that the pre-Permian units exposed within the tectonic window underwent thrusting during this compressive phase, potentially involving the reactivation of older thrusts, and that the initial structural uplift of the Jabal Akhdar may have commenced during this tectonic event (Mann & Hanna, 1990). Recent studies, on the other hand, have led to a revision of the relative chronology between the two cleavage sets. Callegari et al. (2020) identified two slaty cleavage systems, with the steeply dipping cleavage "S_2" crosscutting the gently dipping "S_1" cleavage, indicating that the latter formed earlier than S_2.

The formation of the cleavage systems in the pre-Permian rocks of the Jabal Akhdar Dome is still controversial. Although S_1 was initially proposed to result from a Palaeozoic folding event, commonly interpreted as Hercynian in age, Le Métour et al. (1990) reported that structural analyses in the Sahtan Window demonstrated that the Palaeozoic folds are not associated with an axial plane cleavage. However, the author also stated that the asymmetric folds to which S_1 appears to be genetically related are characterized by SW-dipping axial planes, with the vergence direction consistent with the sense of shear deduced from the cleavage-shear plane relationship (Le Métour et al., 1990). Indeed, most studies still ascribe the origin of the cleavage sets to folding events. Mann & Hanna (1990) linked their S_1 to a set of asymmetrical folds, referred to as "F_1", up to 5 km in wavelength, with subvertical, NE-SW to ENE-WSW-trending axial planes and fold axes plunging toward the NE (Scharf et al., 2021). These features are mostly developed in the Sahtan Window, where the subhorizontal cleavage set S_2 has been interpreted as overprinting major folds. S_2 has been associated with the development of kinks, mullions, crenulations, and meter-scale, low amplitude, SW to S shallow dipping folds, referred to as "F_2" (Fig. 7) (Mann & Hanna, 1990).

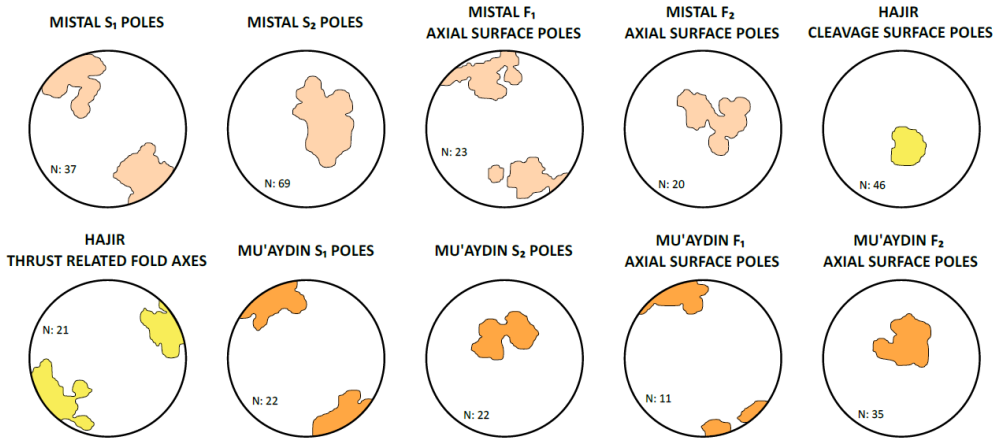

***Figure 7**: Stereographic projections of fold axes and poles to axial surfaces (F_1 and F_2) and to cleavage systems (S_1 and S_2) measured in the Sahtan Window area (redrawn and modified after Mann & Hanna, 1990).*

Even parasitic folds, affecting both the Mistal and Mu'aydin Formations in the conglomerate and competent calcareous siltstone beds, respectively, have been reported as displaying S_1 being overprinted by S_2 (Mann & Hanna, 1990). Additionally, S_1 has also been associated with NW to NNW-dipping thrusts, characterized by a transport direction toward NE and mainly evident along fold limbs and within the competent Hajir Formation; SW-dipping shear zones have been interpreted as backthrusts, leading to the formation of triangle zones and pop-up structures (Mann & Hanna, 1990).

On the other hand, a study by Callegari et al. (2020) has identified two main deformation events, "D_1" and "D_2," characterised by the associated F_1 and F_2 folds (Fig. 8), as ranging in age between the age of the Ediacaran Fara Formation deposition and the age of the hiatus of the "Hercynian Unconformity", extending from the Early Cambrian to the Middle Permian (Callegari et al., 2020).

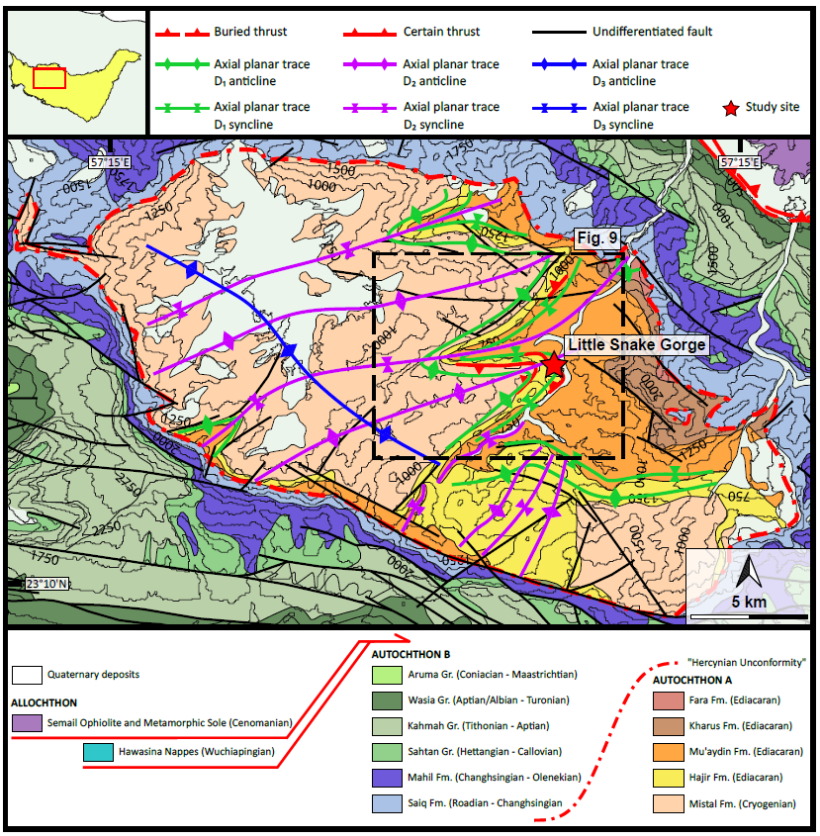

***Figure 8**: Geological map of the Sahtan Window, where the D_1 (green), D_2 (purple), and D_3 (blue) axial planar traces are indicated (redrawn and modified after Callegari et al., 2020, and Scharf et al., 2021).*

A third event, "D_3", has been related to the post-Semail Ophiolite obduction doming of the Jabal Akhdar tectonic window, which affected the orientation of the pre-Permian F_1 and F_2 while shaping the dome as presently exposed (Fig. 8) (Callegari et al., 2020; Scharf et al., 2021).

The two S_1 and S_2 slaty cleavage systems have been linked with the D_1 and D_2 deformation phases and represent the axial planar cleavage to F_1 and F_2, respectively (Callegari et al., 2020). The tight, cylindrical F_1 folds are characterized by subhorizontal fold axes and gently dipping axial planes, and their amplitude ranges between meters and tens of meters. They are best visible in the Hajir Formation, with truncated hinges due to ductile shear zones and thrusts near the Small Snake Gorge location, the study area of this thesis. The geometrical relationship between D_1 and D_2-related structures suggests that the maximum shortening direction during D_1 and F_1-formation was NE-SW with overall NE fold vergence. Ductile conditions are suggested by thickened hinges, thinned limbs, shallow SW-dipping axial planes, D_1-related thrusting with NW-vergence, and the ductile deformation that characterizes the Hajir Formation. After exhumation, F_1-related planar structures were most likely reactivated as brittle extensional faults (Callegari et al., 2020; Scharf et al., 2021).

F_2 folds are characterized by ENE-WSW-striking, subvertical axial planes, suggesting a NNW-SSE-oriented, subhorizontal maximum shortening direction. Their amplitude ranges between hundreds of meters and kilometers. Their fold axes plunge c. 55-60° toward the ENE. However, since the rock formations of the Jabal Akhdar tectonic window were rotated during the D_3 doming by c. 30° along a WNW-ENE-trending axis, the original plunge of the F_2 axes is to be considered at c. 25-30° (Fig. 9) (Callegari et al., 2020; Scharf et al., 2021).

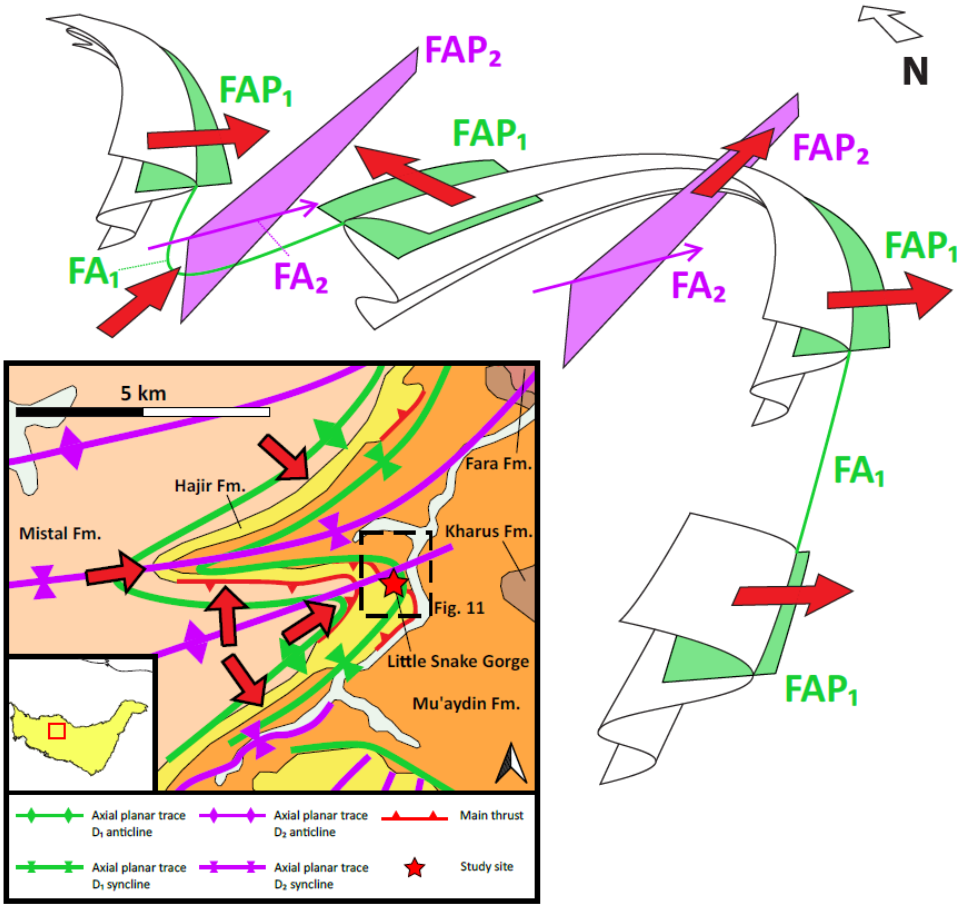

***Figure 8**: Schematic representation of the F_1 (green) and F_2 (purple) folds; D_1 vergence direction is indicated by the red arrows; FA: Fold Axis, FAP: Fold Axial Plane (modified and redrawn after Callegari et al., 2020, and Scharf et al., 2021).*

Considering the systematic change in F_1 orientation, an interference folding model suggests that F_1 folds have been re-folded by F_2 folds (Callegari et al., 2020; Scharf et al., 2021). Since the deposition of the Fara Formation ended in the Ediacaran (Bowring et al., 2007) and the NW-SE-directed shortening associated with the Angudan Orogeny has been dated to c. 525 Ma (Al-Husseini, 2014; Callegari et al., 2020), D_2 has been associated with this major deformation event because of the compatibility between its shortening direction and the F_2-related structures (Callegari et al., 2020; Scharf et al., 2021). Therefore, the NE-SW-directed D_1 event has been generally interpreted as having affected the Jabal Akhdar Dome between c. 540 and 525 Ma. Consequently, D_1 has been traditionally ascribed to the Cadomian Orogeny, which is dated to between c. 620 and 500 Ma and described as characterized by a SW-NE-directed compression (Rossetti et al., 2015; Callegari et al., 2020; Scharf et al., 2021; Stern et al., 2024).

Accordingly, the development of major structures within the Precambrian units of the Jabal Akhdar Dome is principally attributed to a complex succession of deformation phases spanning from the Ediacaran to the early Cambrian (e.g., Mann & Hanna, 1990; Callegari et al., 2020; Scharf et al., 2021). Geochronological data on the evolution of the tectonic window remain, however, scarce, and the deformation phases outlined above are primarily based on the relative dating of major structures and on the rather lose correlation between shortening directions and structural geometries. The Jabal Akhdar tectonic window, located in the inner zone of the Arabian margin, has been mainly considered part of the unsubducted portion of the Arabian passive margin during the Late Cretaceous continental subduction and, as such, it would have experienced only anchizonal deformation and metamorphic conditions during the Semail Ophiolite obduction (e.g., Searle, 2007; Zuccari et al., 2023). Subduction evidence has thus been exclusively sought after in the Saih Hatat Dome farther to the NE, where exposed rocks have been subjected to eclogite facies conditions (e.g., Warren et al., 2003; Breton et al., 2004; Agard et al., 2010). A steep structural and metamorphic gradient, ranging from upper anchizonal conditions in the SW of the Jabal Akhdar Dome to eclogite facies conditions in the northeasternmost portion of the Saih Hatat Dome, has thus been proposed (Fig. 10) (Breton et al., 2004).

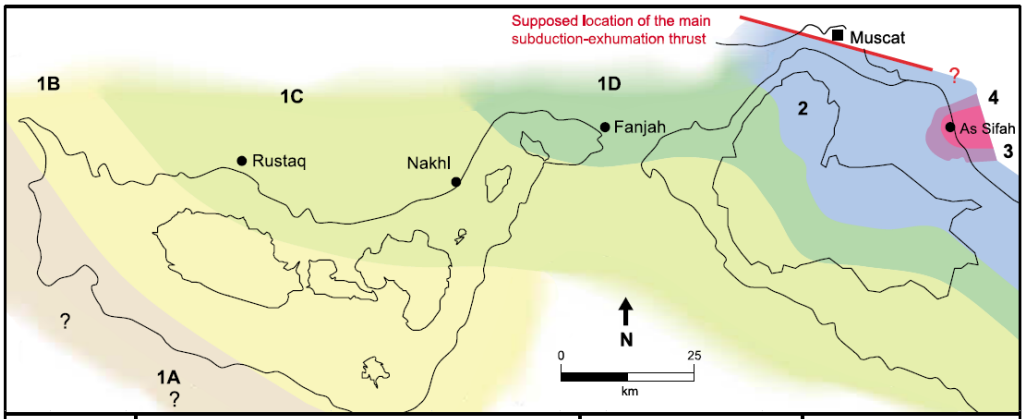

Zone		Metamorphic facies	Pressure	Temperature
EXTERNAL	1A	Upper Anchizone	0.2 - 0.4 GPa	<200°C
	1B			
	1C	Deep Anchizone		
	1D	Greenschist	0.4 - 0.7 GPa	200 - 300°C
INTERNAL	2	Glaucophane Blueschist	0.6 - 1 GPa	250 - 435°C
	3	Glaucophane-Almandine Blueschist	0.6 - 1.5 GPa	380 - 500°C
	4	Glaucophane Eclogite	1.5 - 2 GPa	500 - 580°C

***Figure 9**: Metamorphic facies spatial distribution of the autochthonous units from the southwestern Jabal Akhdar Dome to the northeastern Saih Hatat Dome (modified after Breton et al., 2004).*

However, Breton et al. (2004) identified in the autochthonous units of both tectonic windows top-to-NNE shear deformation defined by thrusts, imbrications, and associated ductile shear foliations. These structures have been interpreted as consequences of a NE-dipping, intra-continental subduction zone, developed in the Arabian passive margin during the Late Cretaceous (Breton et al., 2004). Since an opposite regional scale vergence would be generally expected from a NE-directed slab subduction, these NNE-verging structures have been associated with syn-orogenic exhumation processes in the subduction channel; the only reported indication of the subduction phase is represented by microfolds verging toward the SSW, whose axial plane foliation has been linked to a prograde mineral assemblage within the Saih Hatat Dome eclogites (Breton et al., 2004).

A different perspective has been recently offered by Zuccari and coworkers (2023), who studied top-to-NE calc-mylonitic shear zones and carbonate veins within the Hajir Formation in the central Sahtan Window, documenting evidence of blueschist-facies metamorphic conditions associated with temperature and pressure estimates of c. 350°C and c. 0.9 GPa, respectively. They were dated using the U-Pb method and yielded ages of approximately 97 Ma. Therefore, this deformation phase has been tentatively ascribed to the Late Cretaceous subduction of the Arabian continental margin and to subsequent obduction of the Semail Ophiolite (Zuccari et al., 2023), confirming the presence of Late Cretaceous, NE-verging structures.

Additionally, Degl'Innocenti (2024) reported temperature and pressure conditions of approximately 328 °C and 0.66 GPa, respectively, associated with NW-verging folds within the Mu'aydin Formation in the central Sahtan Window. In contrast, estimates of c. 350 °C and c. 0.47 GPa were obtained from the western sector of the window, along the NE-verging Yasib Thrust, which emplaces the Saiq Formation over the Mistal Formation, thereby reactivating the Hercynian Unconformity (Degl'Innocenti, 2024). The presence of both greenschist and blueschist facies assemblages in the region indicates that the previously proposed SW-NW metamorphic gradient (Fig. 8) may require reevaluation.

Recent studies by Scharf et al. (2025) dated by U-Pb extensional calcite veins from the outer parts of the Hajir Formation fold hinges, previously attributed to Cadomian deformation by Callegari et al. (2020). The resulting ages, ranging between 9 and 2 Ma, are in stark contrast with the expected Cambrian or Late Cretaceous ages, suggesting that calcite-filling and overprinting of possibly Cadomian or Cretaceous subduction-related fractures must have also occurred during a late Miocene to Pleistocene hydrothermal event (Scharf et al., 2025).

The major structures in the Autochthon A are truncated by the Hercynian Unconformity, which separates the steeply dipping and folded Precambrian rocks and the gently N-dipping Saiq Formation. Both the Hercynian Unconformity and the Autochthon B formations have been mainly considered "undeformed" by the Late Cretaceous tectonic evolution of the Arabian passive margin. However, early studies have identified Late Cretaceous thrusting even in the Autochthon B platform carbonates in the northern Jabal Akhdar Dome and have described evidence of tectonic movement along the unconformity surface, supported by displacement evidence and tectonic brecciation of both the overlying Permian carbonates and the underlying Precambrian formations (Hanna, 1990; Mann & Hanna, 1990; Degl'Innocenti, 2024). Due to the lack of absolute age constraints, it can only be concluded that the reactivation of the Hercynian Unconformity took place during post-Permian times.

Evidence of post-Carboniferous deformation of the Jabal Akhdar Dome is also preserved in the architecture of the middle and lower crust and in variations in Moho depth. Seismic tomography and deep seismic cross sections have been recently used to reveal and characterize the deep structural features of the Central Oman Mountains. The negative seismic velocity anomalies below the Jabal Akhdar Dome, in the middle and lower crust levels, have been interpreted as due to NE-directed continental crust underthrusting. Additionally, the thickened tectonic window crust and the difference in Moho depth between the latter, around 40 km deep, and the Saih Hatat Dome, around 35 km deep, have been related to different post-obduction exhumation histories (Weidle et al., 2023).

1.3 - STRUCTURAL SETTING OF THE LITTLE SNAKE GORGE

The following analysis focuses on a c. 800 m long outcrop situated in a steep and narrow canyon, known as the "Little Snake Gorge". The gorge is located in the western Jabal Akhdar Dome, in the Sahtan Window, along Wadi Bani Awf (Fig. 10), and, specifically, it cuts through steep cliffs in the hinge zone of one of the regional-scale F_2 folds defined by Callegari et al. (2020), with c. NE-SW-trending, subvertical axial planes, along the tectonic contact between the Hajir and the Mu'aydin Formations, inhere referred to as the "Little Snake Gorge Thrust" (Fig. 11).

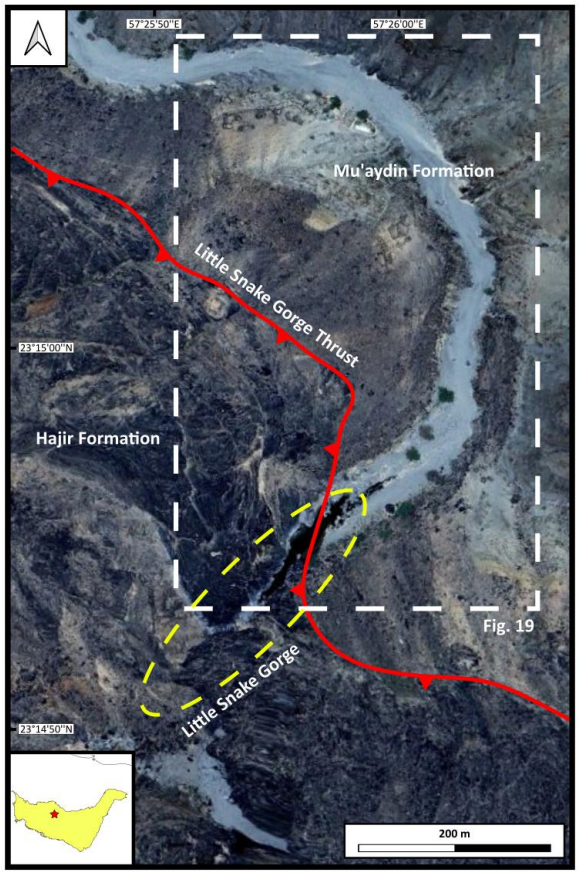

***Figure 10**: Satellite image of the Little Snake Gorge section, located in the Sahtan Window; the yellow dashed line delineates the precise extent of the gorge, whereas the study area is framed by the white dashed box.*

Previous studies from this locality mainly focused on the competent, organic matter-rich carbonates of the Hajir Formation, and the structural and tectonic evolution of the area is still debated. Mann & Hanna (1990) have reported that NW to NNW-dipping thrusts dominates the area, characterized by a transport direction toward SSE. SW-dipping shear zones have been interpreted as backthrusts (Mann & Hanna, 1990).

Based on measurements carried out in the greater Snake Gorge area, where thrust surfaces are exposed within the Hajir Formation, the authors identified two phases of movement: a first event is associated with NW to SE-dipping slickensides and NE-SW-trending folds, while NNE-SSW-dipping slickensides define a second event. Furthermore, a subhorizontal, S to SW-dipping "S_2" cleavage has been identified as cutting through an earlier, NE-SW-directed axial planar "S_1" cleavage, steeply dipping toward NW and SE (Mann & Hanna, 1990).

Callegari et al. (2020) reported that the deformation event "D_1" can be studied in this location, situated in the hinge of one of the "F_2" anticlines. "F_1" folds, which exhibit here an amplitude of c. 50 m, have been associated with the subhorizontal "S_1" cleavage, which appears parallel to the fold axial plane with an ENE vergence. F_1 fold axes are described as subhorizontal, with a trend that varies from E-W along the fold northern limb, to N-S in the hinge zone, and to NE-SW along the southern limb. F_1 folds have also been associated with ENE-verging, up to 50 cm thick carbonate shear zones within the Hajir Formation. Evidence of brittle overprint of these shear zones, linked to an extensional, top-to-SW event, has been reported. Furthermore, the subvertical axial plane cleavage "S_2" has also been reported in the area (Callegari et al., 2020).

Zuccari et al. (2023), on the other hand, reported the presence of the Little Snake Gorge Thrust placing the Hajir Formation above the Mu'aydin Formation. Several measurements taken on contractional calc-mylonitic shear zones within the Hajir Formation carbonates indicate a NE-directed transport. Up to 20 cm thick mylonitic to ultramylonitic shear zones cutting discordantly across the bedding and thinner shear zones, developed along the bed-bed interfaces of the NE-verging fold limbs due to a flexural-slip folding mechanism, have been distinguished and described (Zuccari et al., 2023). The former shear zones are characterized by a penetrative, SW-dipping mylonitic foliation defined by lenses and laterally continuous films of graphite; this foliation is associated with a SW-plunging stretching lineation and thrusting-related top-to-NE S-C structures along with oblique foliation, and it transposes quartz and calcite veins. Shear zones along bed-bed interfaces are more localized, up to 5 cm thick, and contain sheared quartz and calcite-aragonite veins and fibers (Zuccari et al., 2023). Cyclic brittle-ductile deformation has been documented for all the shear zones, since mode-I veins with opening directions subparallel to the regional SW-NE shear direction cut across the mylonites and are themselves transposed by the latter. This dynamic equilibration occurred under high-pressure conditions, as aragonite has been observed in both the veins and the mylonites, which have been interpreted as coeval. Additionally, the veins have been considered natural barometers, as the tectonic overpressure is released upon fracture formation, leaving the vein infill subjected solely to ambient pressure conditions (Zuccari et al., 2023).

Dating and pressure-temperature estimates carried out by Zuccari et al. (2023) were conducted on the carbonate rocks of the Hajir Formation exposed in this area, thereby documenting blueschist-facies conditions related to the Cretaceous continental subduction of the Arabian passive margin within the Little Snake Gorge (Zuccari et al., 2023). Raman spectroscopy on carbonaceous material (RSCM) and high-resolution micro-Raman maps have been used to determine the maximum metamorphic temperature reached by the mylonites and to discriminate calcite from aragonite in the latter and mode-I veins (Zuccari et al., 2023). Trace element analyses on aragonite confirmed Sr values lower than 1%, thus excluding lower pressure values for the calcite-aragonite transformation (e.g., Carlson, 1980).

At the same outcrop, however, Scharf et al. (2025) studied the veins associated with SW-dipping thrusts, located in the extended part of the overturned "F_1" folds' hinge zones. Here, veins have been reported as mostly bed perpendicular, with vein-bed intersections subparallel to both fold axes and planes. Furthermore, up to 1 cm-thick, randomly oriented calcite veins have been reported along fault planes. NE-verging thrusts, which are subparallel to the fold axial planes, have been described as associated with calc-mylonitic, up to tens of cm-thick shear zones. Slickenlines on thrusts indicate a SW vergence, suggesting that they may have been reactivated as extensional faults (Scharf et al., 2025).
The supported maximum shortening horizontal direction is NE-SW-trending, consistent with both the Cadomian and Cretaceous interpretations. However, U-Pb dating provided ages ranging from 9 and 2 Ma, contrasting with the expected Cambrian or Late Cretaceous ages, suggesting that calcite-filling and overprinting of possibly Cadomian or subduction-related veins must have been active during a late Miocene to Pleistocene hydrothermal event (Scharf et al., 2025).

There are only a few studies dealing with the deformation structures of the Mu'aydin Formation. Mann & Hanna (1990) have reported that thrusting is not easy to recognize within this formation, although the frequent repetition of the more competent carbonate layers suggests that tectonic imbrication could have been active. Nevertheless, parasitic folding has been reported affecting bands of the Mu'aydin Formation calcareous siltstones, often associated with a NE-SW-directed axial planar cleavage "S_1". The authors reported that the latter is again overprinted by a later, gently dipping cleavage "S_2" (Mann & Hanna, 1990).

To reconstruct the tectonic and structural evolution of the Autochthon A, the Mu'aydin Formation proves crucial for understanding the processes that have affected the Jabal Akhdar Dome itself, from a possible Cadomian deformation event to a potential Late Cretaceous continental subduction.

CHAPTER 2 - METHODS

The initial phases of this study involved detailed lithostratigraphic and structural mapping of the Little Snake Gorge key sector to achieve a comprehensive understanding of the processes responsible for the development of the Jabal Akhdar Dome and the evolution of the Oman Mountains (Ch. 2.1).

This outcrop-scale investigation was integrated with microstructural characterization and systematic petrographic analysis of representative samples to quantitatively assess deformation mechanisms and potential metamorphic overprints in the Mu'aydin Formation (Ch. 2.1).

Raman spectroscopy was applied to constrain the pressure-temperature conditions associated with forming calcium carbonate-filled veins in organic matter-rich lithotypes (Ch. 2.2).

2.1 - STRUCTURAL SURVEY AND MICROSTRUCTURAL PETROGRAPHIC ANALYSES

Comprehensive structural field data were gathered from ten key locations along the Little Snake Gorge outcrop, encompassing brittle and semi-ductile deformation features. Analysis of the geometry and kinematics of these structures provided the basis for an initial qualitative interpretation of the deformation mechanisms active in the study area.

Alongside the structural survey, two rock samples were collected for thin-section preparation. These sections facilitated petrographic examination of mineral assemblages and deformation microstructures under the microscope, contributing to a more detailed understanding of the local kinematic evolution. Additionally, selected thin sections obtained from the rock samples were used for Raman spectroscopic analyses.

2.2 - RAMAN MICROSPECTROSCOPY

Raman spectroscopy is a fast, non-destructive analytical method, useful to identify materials from their characteristic spectral patterns, to obtain information on their chemical structures and physical properties, and to measure quantitively or semi-quantitatively the amount of a substance contained in a sample, whether this is in the solid, liquid, or gaseous state (Smith & Dent, 2019). This technique is based on the spectra generated after measuring the Raman light scattering frequency shift, i.e., the inelastic scattering of photons generated by a light source that collides with the sample’s atoms or molecules (Rostron et al., 2016). Despite issues related to sample degradation and fluorescence, the instrument technology has been recently subjected to substantial improvements; furthermore, its ability to analyse samples without preparation, materials inside glass containers, and aqueous solutions led to a recent, significant increase in the application of the technique (Smith & Dent, 2019).

The primary mineral phases analysed were carbonate veins and organic matter. Raman spectral data offered critical insights into their crystallographic structures, specifically allowing distinction between the calcite and aragonite polymorphs in calcium carbonate veins, and estimating the peak temperature experienced by the organic matter within the Mu'aydin Formation. These results were then used to infer the minimum pressure-temperature conditions to which the studied samples were subjected.

The Raman spectroscopy analyses were performed using the WITec alpha300 R confocal Raman microscopy system at the Department of Biological, Geological, and Environmental Sciences (BiGeA) of the University of Bologna. Raman spectra were acquired using the following parameters:

- 532 nm laser source.
- 100x objective.
- 600 g/mm grating.
- 2.5 and 8 mW laser power for carbonaceous material and calcium carbonate, respectively.
- 5 accumulations.
- 10 s integration time.

Furthermore, to focus the observations on the diagnostic peaks, a spectral stitching method has been used to acquire spectra in specific ranges, such as between 0 and 1200 cm^{-1} for calcium carbonate and between 700 and 2000 cm^{-1} for carbonaceous material.

The calcite-aragonite stability field (Fig. 12) has been subjected to several experiments to better constrain the pressure and temperature values that define the transformation between $CaCO_3$ polymorphs (Clark, 1957; Johannes & Puhan, 1971; Madon & Gillet, 1984; Lin & Huang, 2004; Hacker et al., 2005; Zhao et al., 2022; Zuccari et al., 2023).

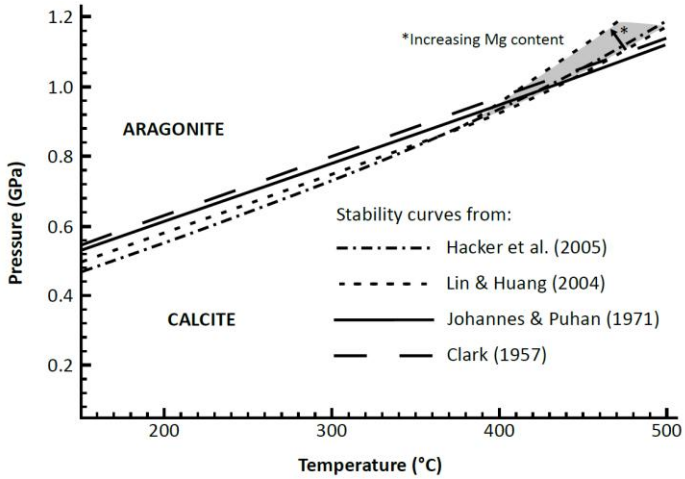

***Figure 12**: Calcite-aragonite stability field as defined by different experimental stability curves (modified after Zuccari et al., 2023).*

Aragonite is a polymorph of calcite that represents a reliable blueschist facies indicator for "pure" carbonate rocks that otherwise lack other pressure-sensitive mineral phases; it is metastable under standard P-T conditions, and its formation and preservation are mostly limited to <10 °C/km thermal gradients and rapid exhumation in dry conditions (Zuccari et al., 2023).

Even if some characteristic textures can help in the discrimination between $CaCO_3$ polymorphs, such as the acicular texture for aragonite (Chakrabarty & Mahapatra, 1999), their precise identification is not possible through common optical microscopy observations. However, Raman spectroscopy represents a non-destructive approach that can provide a quick distinction between calcite and aragonite (Carteret et al., 2013).

The diagnostic bands for aragonite are three weak bands at c. 143 cm^{-1}, 181 cm^{-1}, and 192 cm^{-1}, a strong band at c. 206 cm^{-1}, and two weak bands at c. 702 cm^{-1} and 706 cm^{-1} (Parker et al., 2010). The comparison between calcite and aragonite spectra is shown below (Fig. 13):

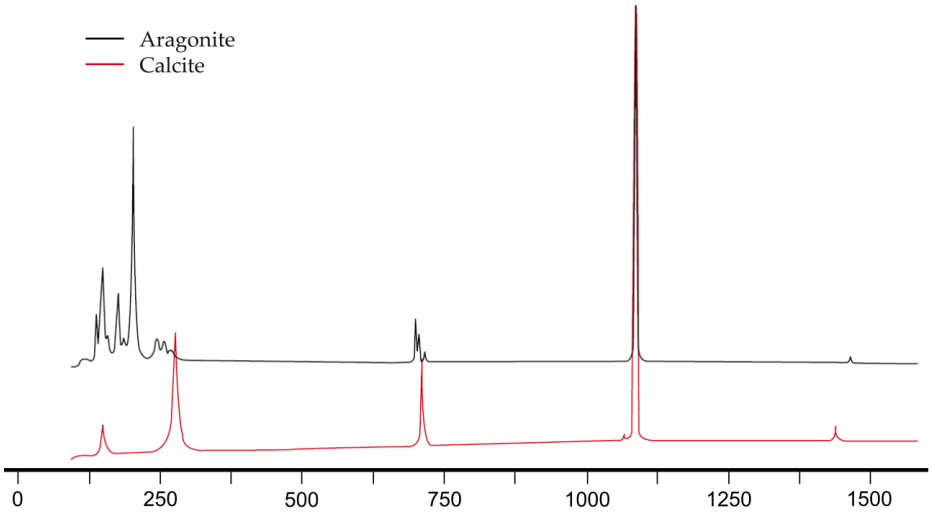

***Figure 13**: Comparison of the Raman aragonite (black) and calcite (red) spectra (modified after Wehrmeister et al., 2007).*

High-P aragonite is characterized by low Sr wt% values, which often substitutes Ca atoms in the mineral crystal lattice under standard P-T conditions. Thus, trace element analyses are important to exclude lower P values for the calcite-aragonite transformation (Carlson, 1980; Zuccari et al., 2023).

The identification of organic matter based solely on optical observations can also present significant challenges. As organic matter is heated, hydrogen, oxygen, and nitrogen are expelled, and the carbon atoms become progressively organized into stacked graphene sheets. This range of materials is called carbonaceous material (Kouketsu et al., 2014). Consequently, organic matter is progressively transformed into graphite s.s. during metamorphic processes (Beyssac et al., 2002; Aoya et al., 2010; Lahfid et al., 2010). Therefore, Raman Spectroscopy of Carbonaceous Material (RSCM) has become a widely used approach to characterize organic matter's structure and to determine its irreversible thermal alteration (Henry et al., 2019).

Carbonaceous material can appear in flake-shaped or anhedral geometries, with colours ranging from mouse gray to straw yellow. It is often included in other minerals, and its grain size can vary significantly, even within the same sample. Furthermore, mechanical polishing of thin sections can compromise the integrity of carbonaceous materials, leading to significant alterations in their Raman spectral characteristics. To mitigate this effect, graphite grains were deliberately selected from subsurface regions, specifically those encapsulated within quartz or calcium carbonate crystals, and situated away from oxides, phyllosilicates, and microfractures.

RSCM is based on the following evidence:

- The carbonaceous material Raman spectrum is sensitive to variations of metamorphic grade (Beyssac et al., 2002; Henry et al, 2019).
- There is an excellent agreement between Raman spectra related to samples with an equivalent metamorphic grade (Beyssac et al., 2002; Henry et al, 2019).
- The evolution of the Raman spectrum with metamorphic grade is controlled by temperature (Beyssac et al., 2002; Henry et al, 2019).
- The degree of organisation of carbonaceous material is not affected by retrograde metamorphism, thus recording peak metamorphic conditions (Beyssac et al., 2002; Henry et al, 2019).

This approach can, therefore, be used as a geothermometer of the maximum temperature conditions reached by the source rock during regional and contact metamorphism, or frictional heating along fault planes (Beyssac et al., 2002; Henry et al., 2019). Furthermore, this method allows in-situ, non-destructive analysis of grains, even when buried in the sample, and it is sensitive to amorphous structures, for instance, amorphous carbon (Kouketsu et al., 2014).

The Raman spectrum of graphite is composed of a first- and a second-order regions falling between 1100 and 1800 cm^{-1} and 2500 and 3100 cm^{-1}, respectively (Fig. 14) (Beyssac et al., 2002; van Zuilen et al., 2012).

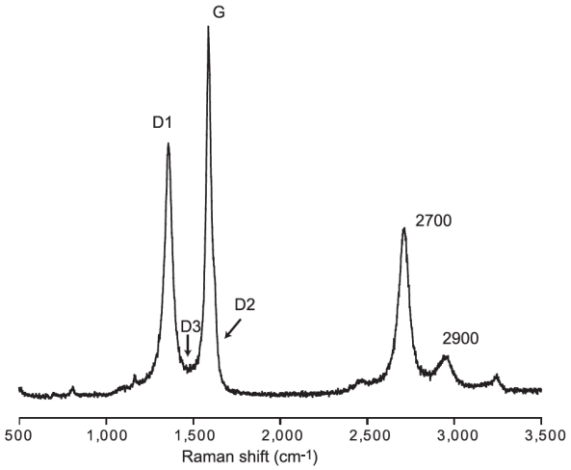

***Figure 14**: Graphite Raman spectrum with first- and second-order regions (modified after van Zuilen et al., 2012).*

The evolution of the graphite Raman spectrum with the increase of the metamorphic degree is shown in Figure 15:

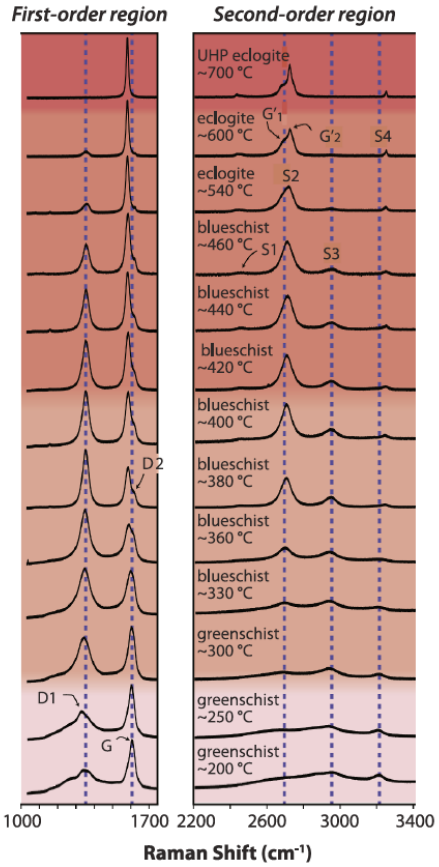

***Figure 15**: Evolution of the first-order region with the metamorphic degree (modified after Henry et al., 2019).*

However, since the degree of organization in the structure of carbonaceous material is quantified by the relative area ratio of the bands in the first-order region (Beyssac et al., 2002), the procedure is based only on the latter (Fig. 16).

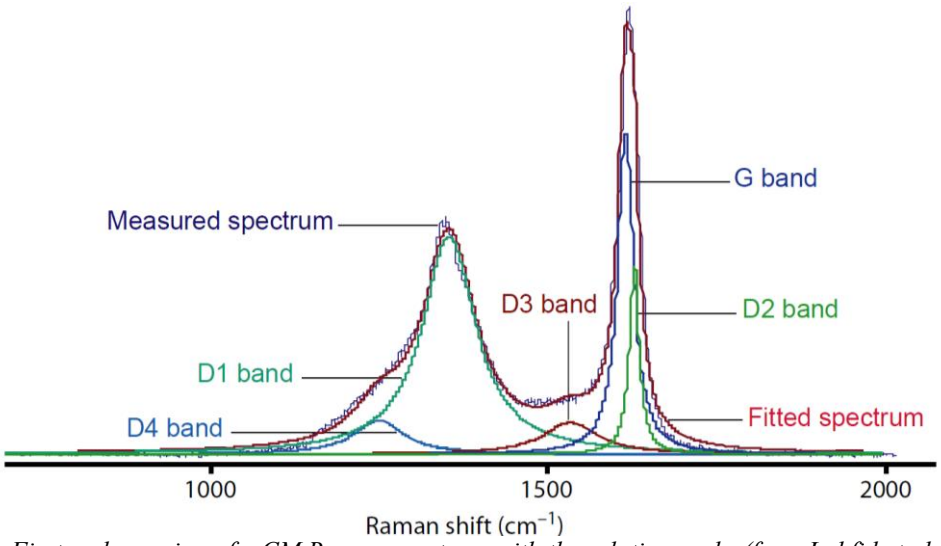

***Figure 16**: First-order region of a CM Raman spectrum with the relative peaks (from Lahfid et al., 2010).*

In the first-order region, the graphite band (G) occurs at c. 1580 cm-1. The band occurring at c. 1350 cm-1 (D1) is intense and wide in poorly ordered carbons. Since during the graphitization process its relative area decreases, it has been attributed to substituting atoms (O, H, N, for instance) or structural defects. The c. 1620 cm-1 band (D2) appears as a shoulder on the G band: in poorly organised carbon, it is impossible to separate the two components, and only one band occurs shifted toward slightly higher wavenumber values. The c. 1500 cm-1 band (D3) is present in poorly ordered carbons as a very wide band, and it is attributed to out-of-plane defects like tetrahedral carbons or small crystallite sizes (Beyssac et al., 2002; Aoya et al., 2010). In addition, a small shoulder is observed on D1 at c. 1250 cm-1 (D4) (Lahfid et al., 2010).

Following Raman spectra acquisition on graphite, the resulting spectra are analyzed and processed using the peak-fitting procedure of the software PeakFit to estimate the maximum temperature experienced by the sample. Various relative area ratios have been tested for their ability to describe the evolution of the Raman spectrum with increasing metamorphic grade, and different approaches have been developed with time (Lahfid et al., 2010). Two methods have been selected to calculate the peak temperature of the samples.

The first method, presented by Lahfid et al. (2010), has been developed to study low-grade metamorphic conditions, from diagenesis to epizone, and it is valid for temperatures between 200 and 320°C, with estimated errors of ± 50°C. Two different area ratios, which rely on the identification of five bands during the peak-fitting procedure, have been proposed (Lahfid et al., 2010):

- RA1 = (D1 + D4) / (D1 + D2 + D3 + D4 + G)
- RA2 = (D1 + D4) / (D2 + D3 + G)

For the analyses conducted in this study, the first ratio (RA1) has been selected.

The peak temperature is then obtained from linearly regressing the data, as shown below in Figure 17:

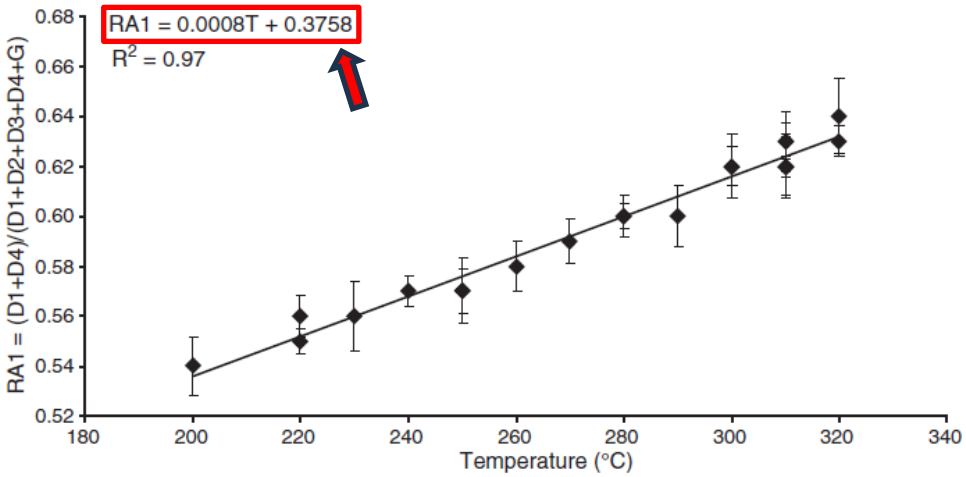

***Figure 17**: Linear correlation between T and RA1 (modified after Lahfid et al., 2010).*

The second method, presented by Aoya et al. (2010), has been developed to study low-pressure (< 3 kbar) contact metamorphism. The proposed relationship between the temperature and the area ratio R2 (Fig. 18), which only relies on the identification of three bands, is valid between 340 and 655°C, with estimated errors of ± 30°C if a sufficient high number of measurements is carried out (N > 50) and if a 532 nm laser source is used (Aoya et al., 2010).

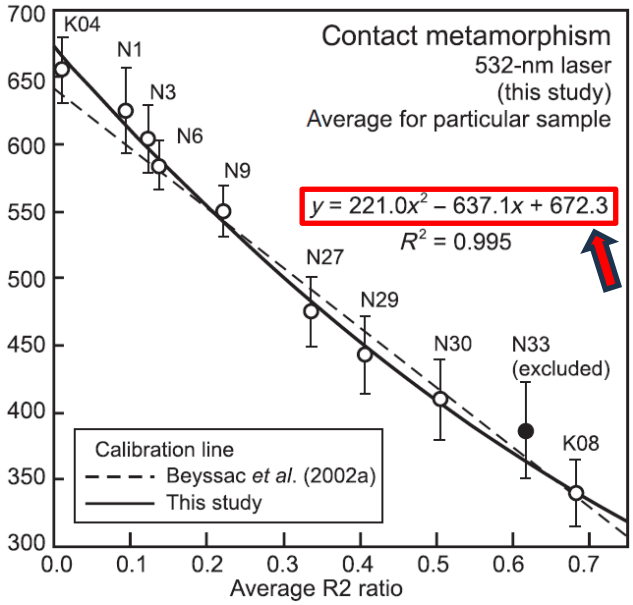

***Figure 18**: Linear correlation between R2 and T (modified after Aoya et al., 2010).*

CHAPTER 3 - RESULTS

3.1 - STRUCTURAL AND PETROGRAPHIC RESULTS

The field campaign conducted in Oman resulted in the collection of a comprehensive set of structural data at the outcrop. These data were subsequently used to produce a structural and geological map of the Little Snake Gorge area, including stereographic projections of the documented structural features (Fig. 19).

The structural survey was carried out through a careful analysis of the outcrops to achieve a high level of detail capable of capturing the smallest variations in the structural framework of the Little Snake Gorge. The structural features measured in the field are further supported by a detailed petrographic analysis of thin sections prepared from rock samples collected during the survey (Table 1).

Location name	Latitude	Longitude	Formation	Sample code	Thin sections number and code
STOP 01	23°15'10.19"N	57°25'54.28"E	Mu'aydin	x	x
STOP 02	23°15'05.79"N	57°26'00.94"E	Mu'aydin	x	x
STOP 03	23°15'02.75"N	57°26'02.13"E	Mu'aydin	x	x
STOP 04	23°14'58.98"N	57°26'01.00"E	Mu'aydin	x	x
STOP 05	23°14'58.54"N	57°26'00.57"E	Mu'aydin	x	x
STOP 06	23°14'58.33"N	57°26'00.38"E	Mu'aydin	x	x
STOP 07	23°14'57.35"N	57°25'59.23"E	Mu'aydin	OM2402A OM2402B OM2402C OM2402D	2 (a, b) 0 2 (a, b) 1
STOP 08	23°14'57.17"N	57°25'58.76"E	Mu'aydin	x	x
STOP 09	23°14'56.84"N	57°25'58.10"E	Mu'aydin	x	x
STOP 10	23°14'56.58"N	57°25'57.50"E	Mu'aydin	OM2401A OM2401B	1 3 (a, b, c)
STOP 11	23°14'55.13"N	57°25'56.54"E	Hajir	x	x

***Table 1**: Reference table of the samples collected during the structural survey; locations are shown in Fig. 19.*

The primary objective was to reconstruct the geometry and kinematics of the outcrop-scale structures and to identify mineral indicators that could aid in constraining the metamorphic conditions associated with specific, regional-scale deformation stages. In the following section, a detailed description of the structures at each structural station is provided (Ch. 3.1).

In addition, the results obtained from fieldwork have been integrated with inputs derived from Raman spectroscopy analysis to quantitatively constrain the temperature and pressure conditions reached by the Mu'aydin Formation in the Little Snake Gorge (Ch. 3.2).

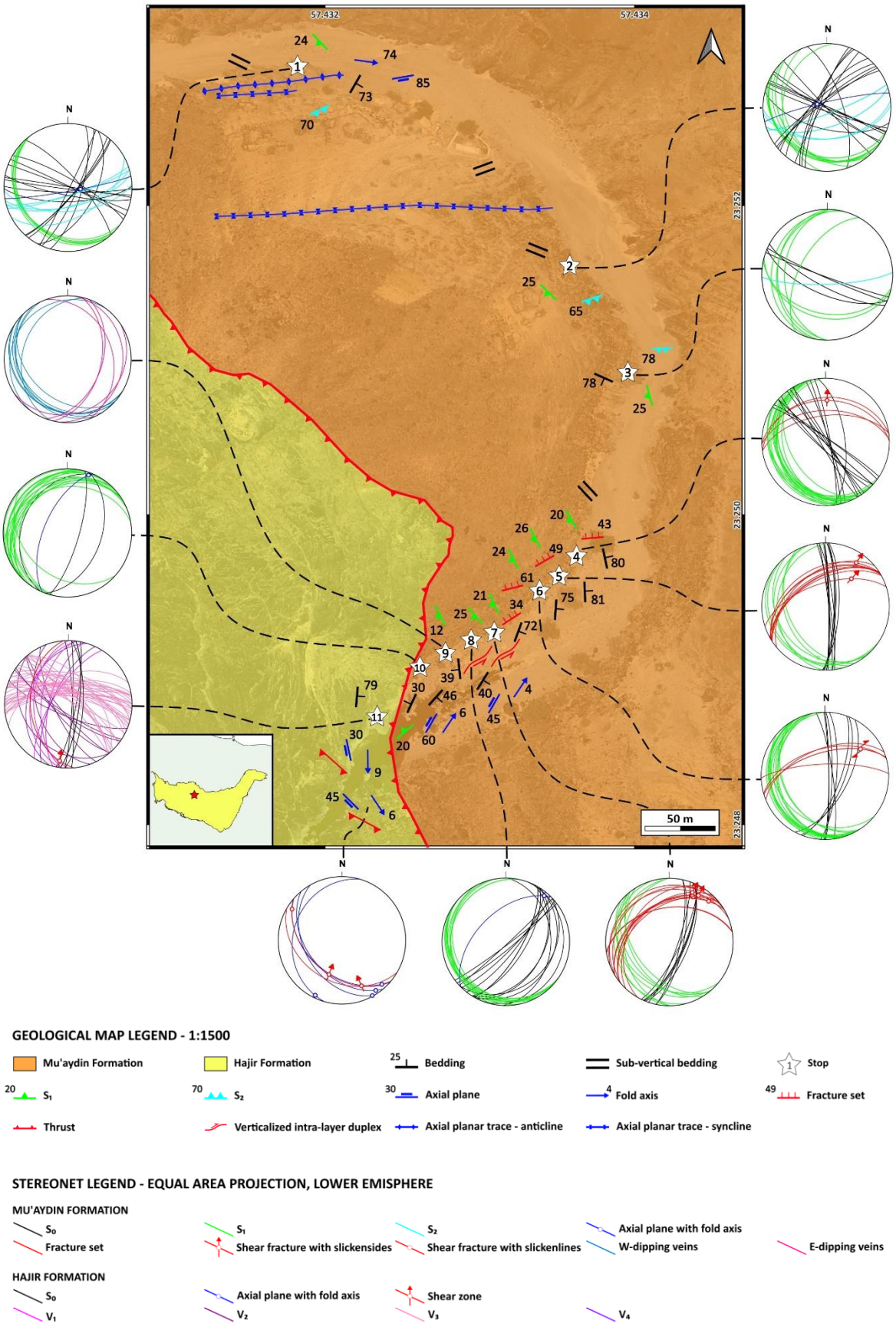

***Figure 19**: Geological map of the Little Snake Gorge area, featuring stereographic projections of all measured structural elements.*

3.1.1 - STOP 01 (23°15’10.19’’N; 57°25’54.28’’E)

Here the Mu’aydin Formation is characterized by subvertical, decimetric carbonate strata, consisting of fine-grained calcarenites and calcilutites with distinct cleavage planes. These strata alternate with less abundant siliciclastic layers, ranging from centimetric to decimetric in thickness, composed of fine-grained arenite interbedded with locally laminated siltstone. Quartz and platy minerals, such as micas, are present.

A meter-scale, ENE-WSW-trending fold, with an axial plane steeply dipping toward the SSE and a subvertical fold axis, is evident (Fig. 20A).

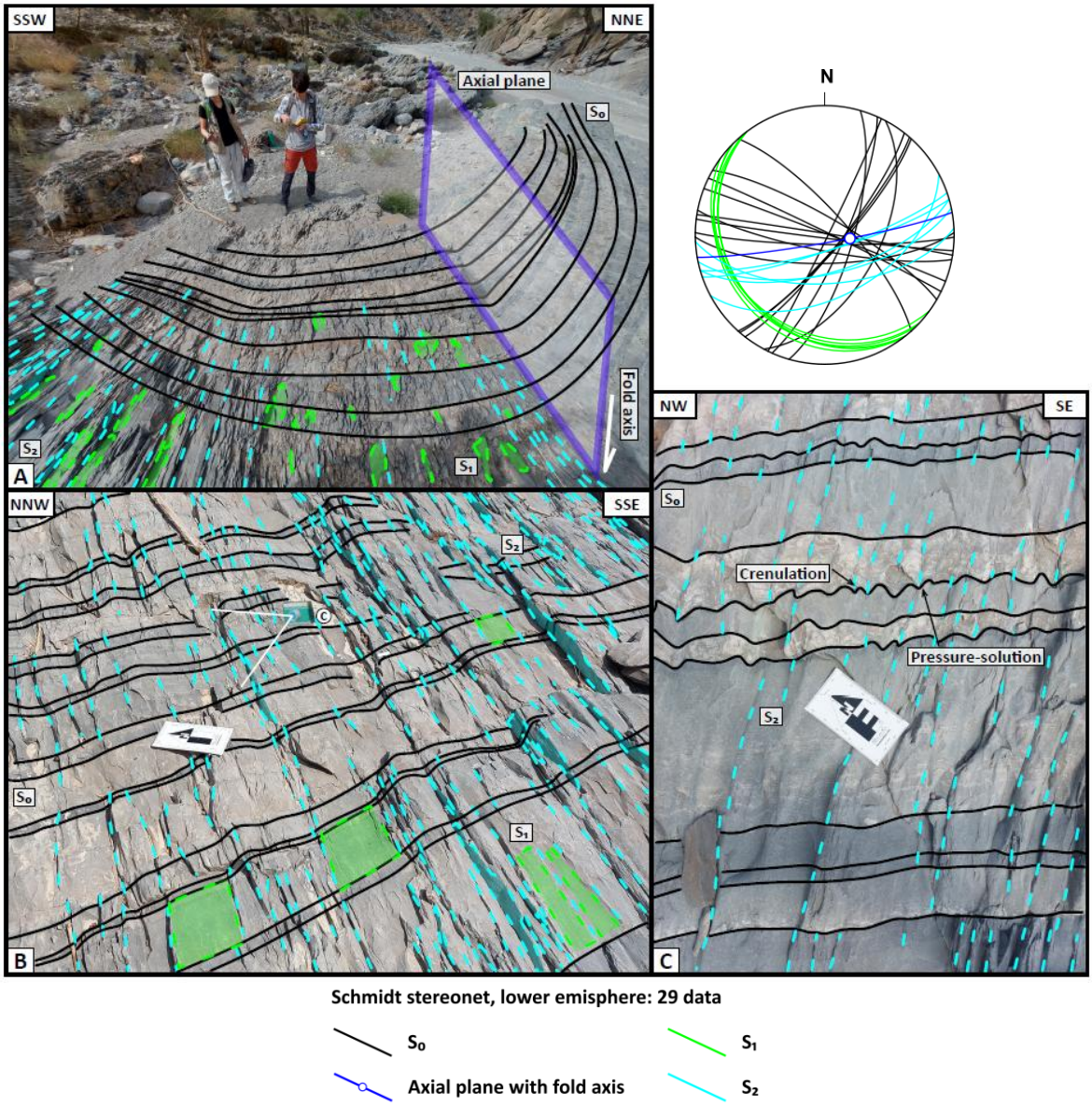

***Figure 20**: Stop 01 - **A**, WSW-ENE-trending fold with subvertical axial plane and fold axis; **B**, Spatial relationship between S_1 (green), S_2 (light blue), and S_0 (black); **C**, Detail on the S_0 incipient crenulation generated by S_2, associated with pressure-solution.*

Two foliation sets have been distinguished. The first set, hereafter referred to as “S_1”, generally dips shallowly to the SW, and is cut across by the second set, hereafter referred to as “S_2”, which steeply dips to the SSE (Fig. 20B). Additionally, the latter appears to be responsible for the weak and incipient crenulation of S_0 and is associated with a pressure-solution component along the cleavage planes (Fig. 20C).

The S_2 foliation set is characterized by foliation planes that are subparallel to the axial planes of the WSW-ENE-trending folds. Moreover, in proximity to the hinge zone of these folds, the angle between S_0 and S_2 approaches 90° (Fig. 20A, B, C). For these reasons, the S_2 foliation has been interpreted as the axial plane cleavage associated with the WSW-ENE-oriented folds, likely associated with a deformation phase characterized by a NNW-SSE-oriented maximum shortening. However, the same perpendicular spatial relationship characterizes S_0 and S_1, suggesting that it too may be associated with the axial plane cleavage of the larger-scale, generally NE-verging folds referred to as "F_1" by Callegari et al. (2020).

The relative chronology of these foliation sets has been previously discussed. Initially, Mann & Hanna (1990) described the gently SW-dipping set as cutting across the subvertical, WSW-ENE-directed one. Differently, Callegari et al. (2020) inverted the relative chronology of the two foliation sets, associating the subhorizontal set with the youngest deformation event, in agreement with the results from my study. However, in contrast to the observations reported by Callegari et al. (2020), no rotation of S_1 dip values has been detected along the fold limbs of the small-scale, WSW-ENE-trending folds with subvertical axial planes.

3.1.2 - STOP 02 (23°15'05.79''N; 57°26'00.94''E)

The Mu'aydin Formation lithotype appears similar to that observed at the previous stop, with subvertical bedding planes. This site hosts another major fold with a WSW-ENE-trending subvertical axial plane and a subvertical fold axis dipping toward WNW. These up-to-decametric-scale folds, inhere referred to as "F_2," are visible from satellite images (Fig. 21A, B).

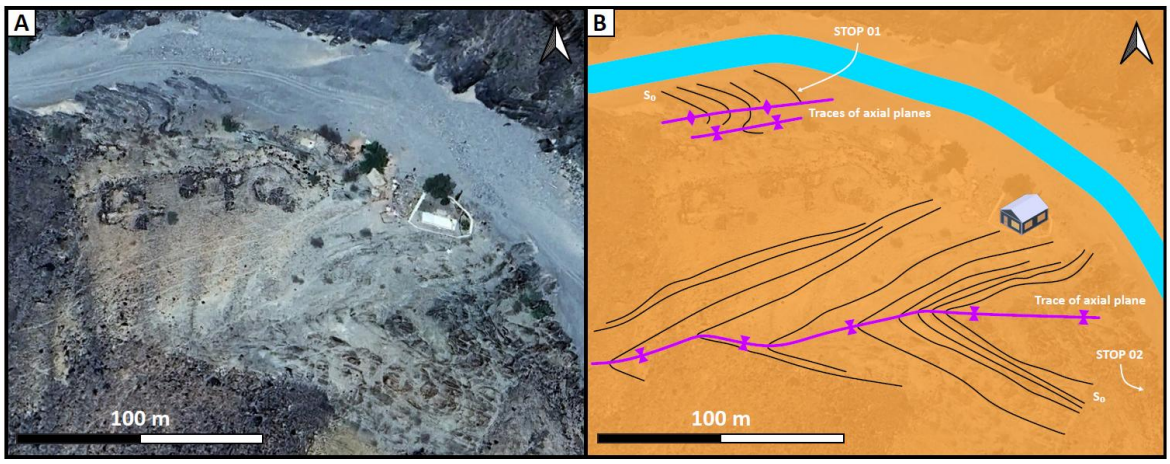

***Figure 21**: **A**, Satellite image of the up-to-decametric scale, ESE-WNW-trending folds present at Stops 01 and 02; **B**, Simplified sketch of the folds with their axial planar traces.*

S_1 and S_2 are, again, evident, with similar dip angles and directions to the Stop 01 (Fig. 22A). As at the previous stop, no significant rotation in the dip values of the S_1 foliation around the fold limbs has been observed. Close to the hinge zone of the F_2 fold, the angle between S_2 and S_0 is again approximately 90° (Fig. 22A).

The bedding surfaces are exposed along the east bank of the wadi. Here, the lineation generated by the intersection between S_0 and both S_1 and S_2, inhere referred to as "L_{01}" and "L_{02}", respectively, provides further details on their overall spatial arrangement (Fig. 22B).

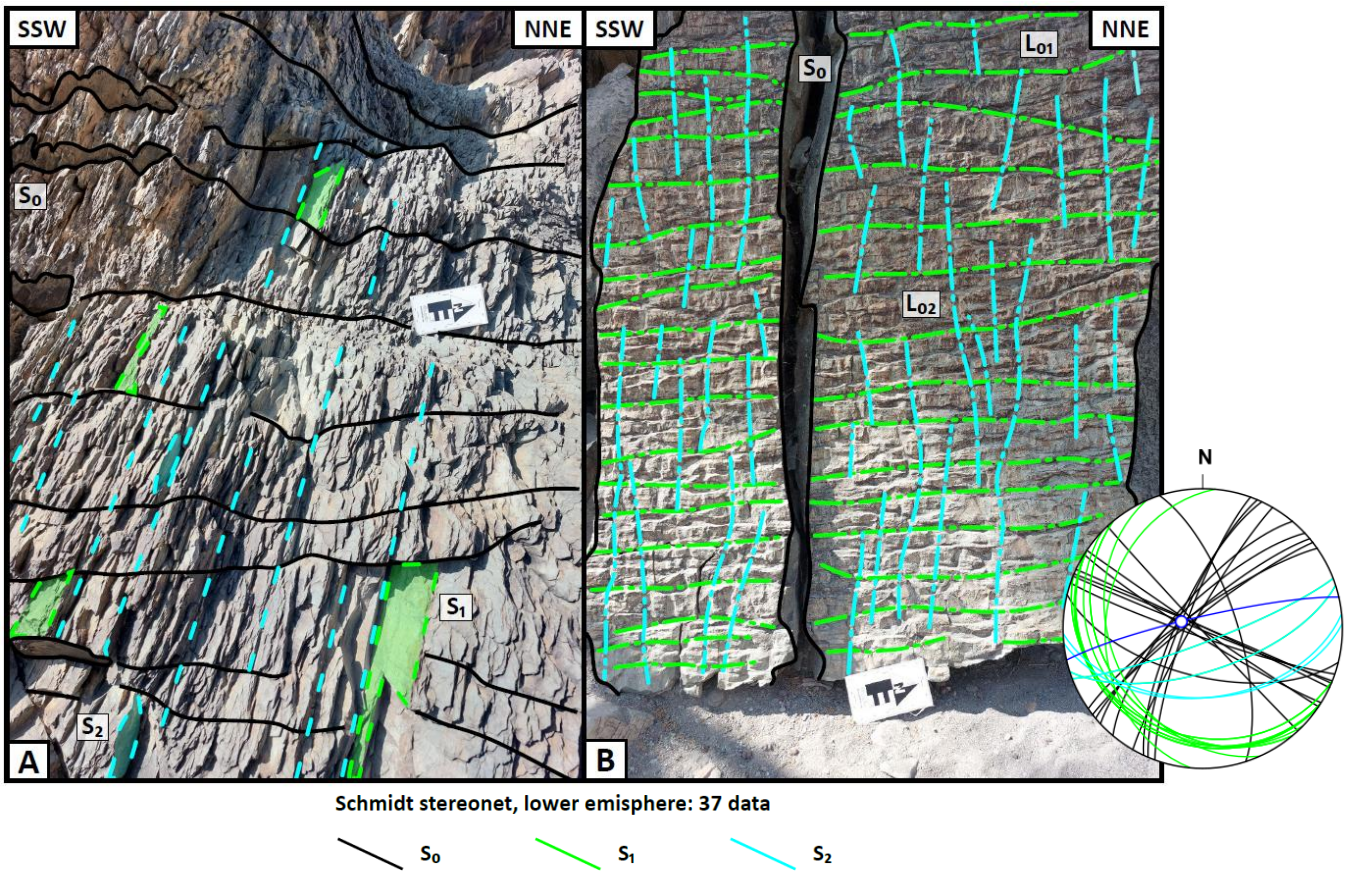

***Figure 22**: Stop 02 - **A**, Spatial relationship between S_0 (black), S_1 (green), and S_2 (light blue); **B**, Bedding surface exposing L_{01} (dashed and dotted green line) and L_{02} (dashed and dotted light blue line).*

3.1.3 - STOP 03 (23°15'02.75''N; 57°26'02.13''E)

A lithological transition toward more abundant siliciclastic layers has been noted at this outcrop, where subvertical bedding planes dip steeply toward the SW (Fig. 23).

The S_1 foliation is characterized by greater variability in its azimuth, ranging from the SSW to WNW, while the subvertical S_2 dips steeply toward the SSE. In this area, the latter appears to be less penetrative. This is likely due to the distance from the hinge zone of the F_2 folds. Indeed, the spatial relationship between S_0 and S_2 is characterized by lower angles (Fig. 23).

Furthermore, S_2 is again responsible for the incipient crenulation of S_0, which is more evident here, likely due to the more significant abundance of siliciclastic layers and to the competence contrast between the latter and the carbonate layers (Fig. 23).

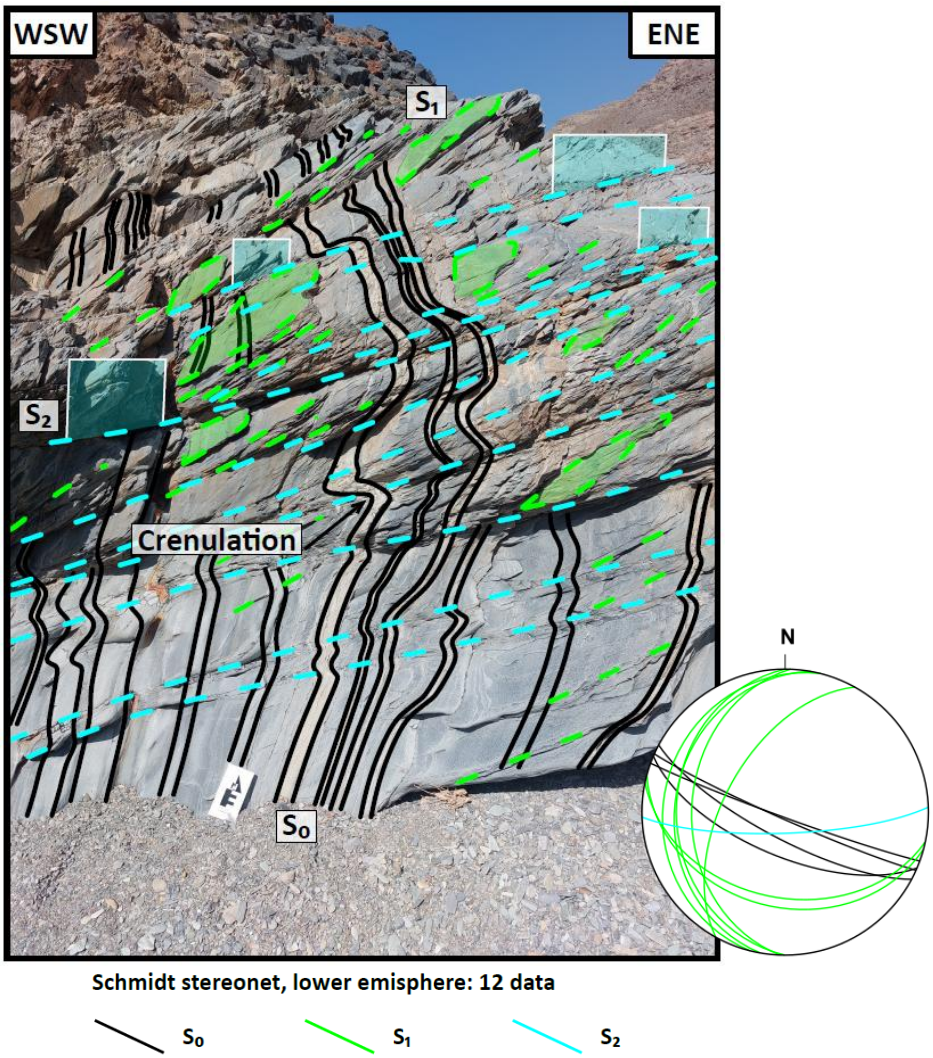

***Figure 23**: Stop 03 – Spatial relationship between S_0 (black), S_1 (green), and S_2 (light blue); the incipient crenulation of the subvertical bedding planes is again caused by S_2; S_1 is characterized by dip directions ranging between SSW and WNW, while S_2 is steeply SSE-dipping.*

3.1.4 - STOP 04 (23°14'58.98''N; 57°26'01.00''E)

The siliciclastic component becomes here the dominant lithotype of the Mu'aydin Formation accounting for approximately 75% of the rock volume. Here, the subvertical strata strike NW-SE to NNW-SSW-with the variation likely due to local weak folding (Fig. 24A).

The gently, SW-dipping S_1 foliation becomes less pervasive and appears to be significantly less pronounced within the carbonate layers (Fig. 24B), while, far from the hinge zone of the F_2 folds, S_2 in no longer distinguishable. S_1 and S_0 are almost perpendicular, and S_1 dip directions are similar to those measured in Stops 01 and 02, dipping toward the SW. A set of high-angle fractures, hereafter referred to as "Fr", has been noted, dipping toward the NNW. This set cuts across both S_0 and S_1 (Fig. 24B), while slickensides along a shear fracture plane support top-to-N extensional kinematics.

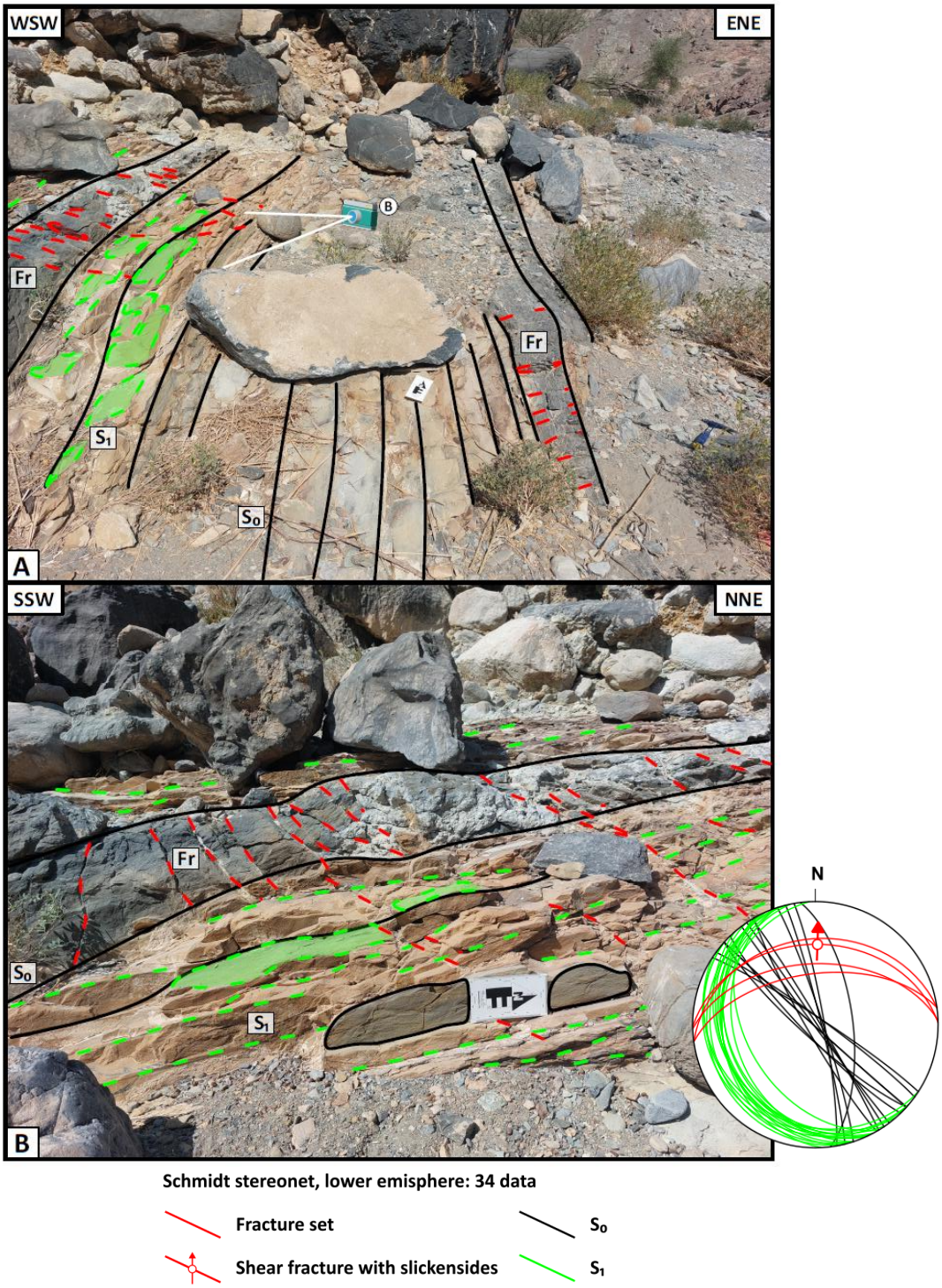

***Figure 24**: Stop 04 - **A**, Lithological variations in the Mu'aydin Formation, where the siliciclastic component becomes the dominant lithotype; **B**, Spatial relationship between S_0 (black), S_1 (green), and Fr (red).*

Different vein systems are present. In the siliciclastic layers, veins exploit the planar anisotropy provided by the foliation, accounting for approximately 10% of the total rock volume. Differently, in the carbonate layers, veins exploit intense and apparently little structured fractures. Nonetheless, two principal vein sets can be identified: one set appears to be parallel to S_1, while another set appears to be perpendicular to S_0, seemingly exploiting Fr.

3.1.5 - STOP 05 (23°14’58.54’’N; 57°26’00.57’’E)

Here bedding planes dip steeply toward the E. A marked increase in both the abundance of siliciclastic layers and in the intensity of foliation therein has been noted. The siltstones display dense, pervasive S_1 planes, which remain perpendicular to S_0. The associated vein volume increases significantly, representing up to 35% of the total rock volume (Fig. 25A, B). Differently, in the carbonate layers, veining is again primarily aligned with the previously defined shear fracture set Fr, characterized here by a dip direction toward the NW and by a top-to-NE, likely transtensional kinematics (Fig. 25A).

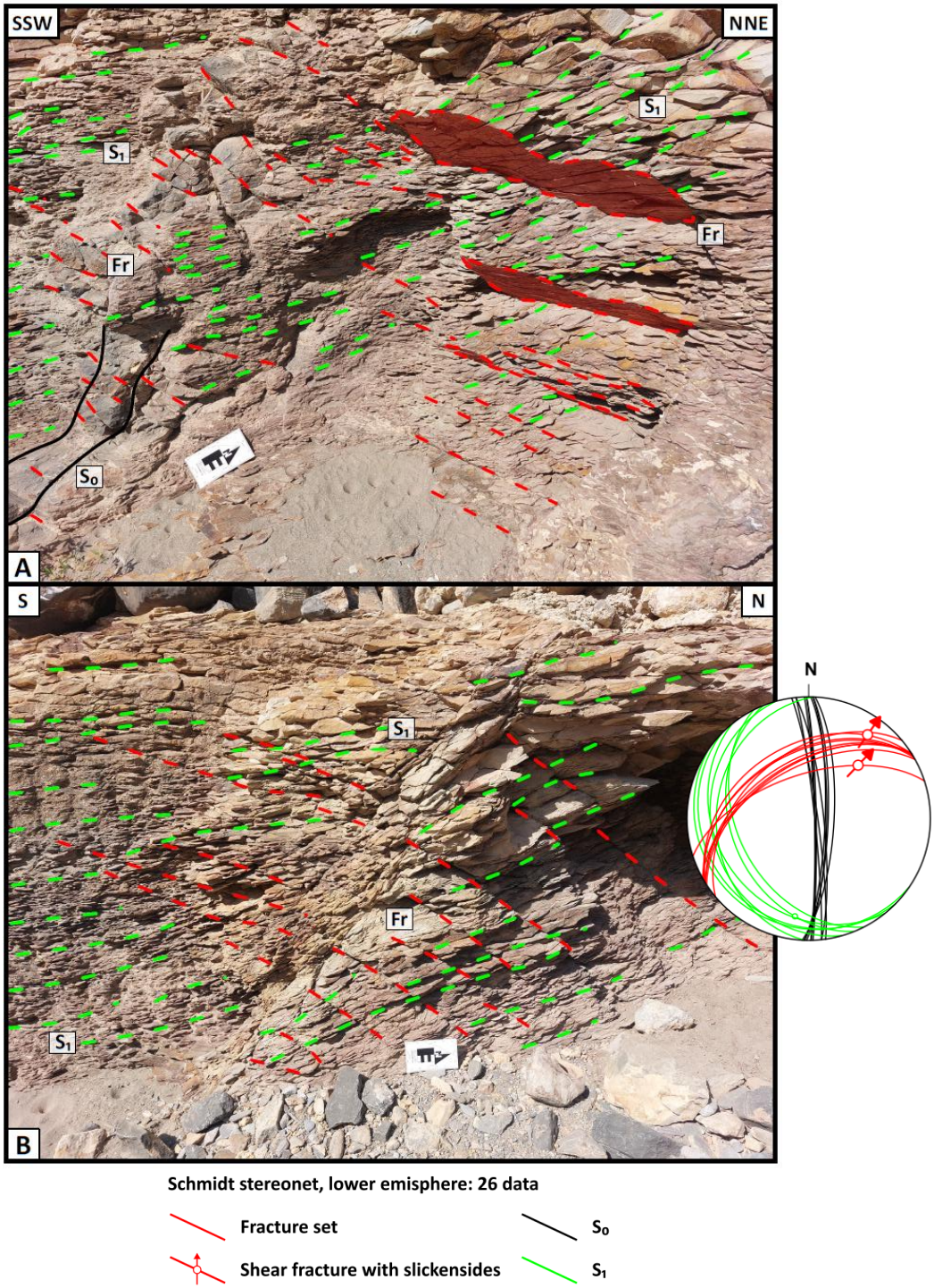

***Figure 25**: Stop 05 - **A**, Spatial relationship between S_0 (black), S_1 (green), and Fr (red); **B**, Focus on the angular relationship between S_1 and Fr.*

3.1.6 - STOP 06 (23°14’58.33’’N; 57°26’00.38’’E)

The siliciclastic component of the Mu’aydin Formation contains here more silty horizons characterized by a light gray color. The bedding planes strike NNE-SSW, dipping steeply toward the ESE (Fig. 26A). Both the density and penetrative nature of S_1 cleavage intensify markedly, while the orthogonal relationship with S_0 is preserved. Vein frequency keeps increasing, accounting for approximately 40% of the rock volume, while the shear fracture set Fr becomes less pervasive, characterized here by a transtensional kinematics (Fig. 26B).

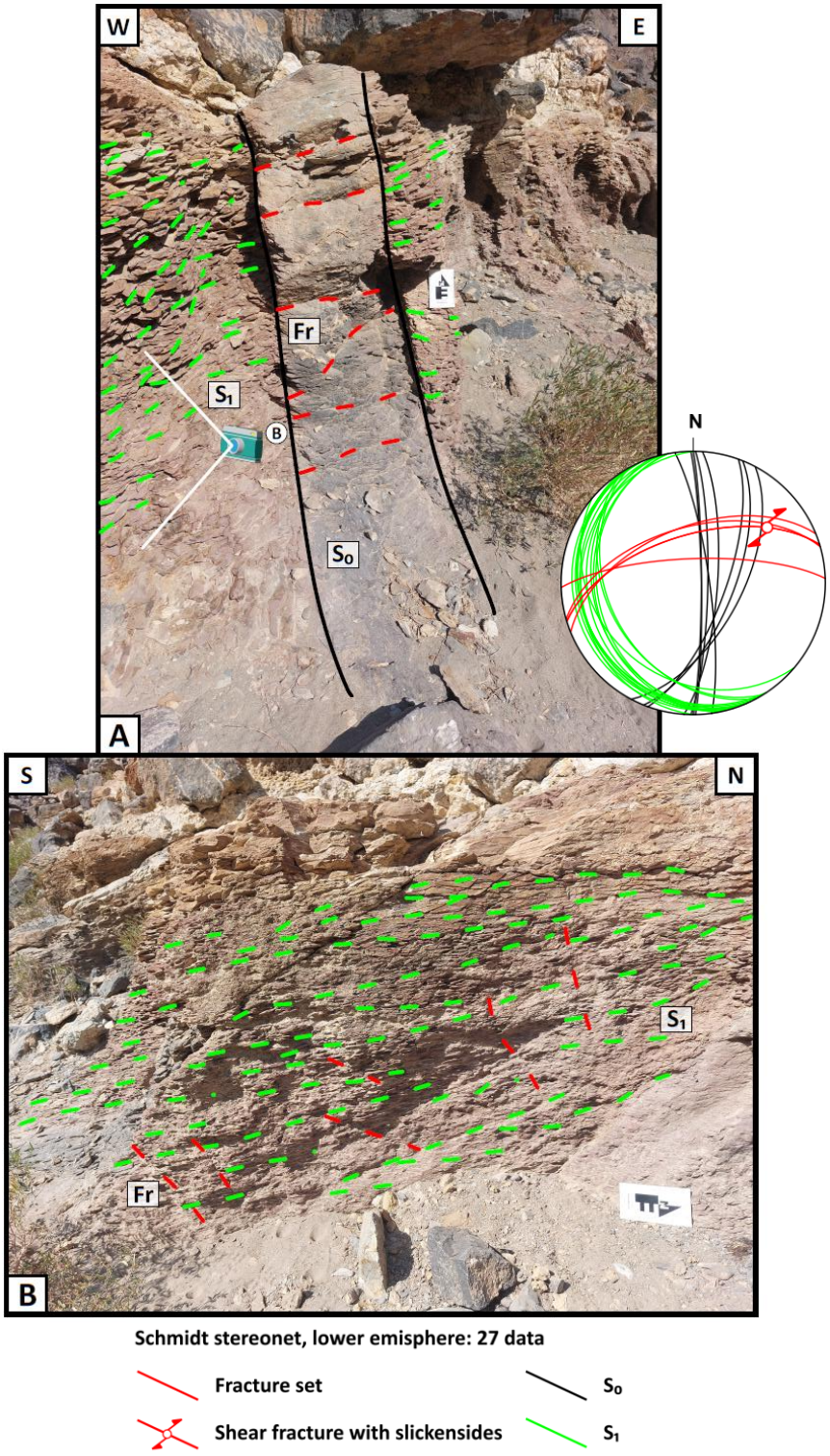

***Figure 26**: Stop 06 - **A**, Spatial relationship between S_0 (black), S_1 (green), and Fr (red); **B**, Focus on the angular relationship between S_1 and Fr.*

3.1.7 - STOP 07 (23°14’57.35’’N; 57°25’59.23’’E)

Bedding dips steeply toward the ESE. Carbonate layers increase in thickness, reaching up to 1 m, and siliciclastic intervals are interlayered with thin carbonate beds up to a few centimeters thick.

Siliciclastic layers are still characterized by the pervasive, low dip-angle foliation S_1. Here, vein frequency accounts for almost the 50% of the total rock volume (Fig. 27C).

Brittle deformation dominates the carbonate units (Fig. 27A), with numerous fractured blocks and higher S_1 foliation angles, most likely due to refraction in more competent layers (Fig. 27A). The angle between S_0 and S_1 is approximately orthogonal. Top-to-NE extensional kinematics is still ascribed to Fr. Furthermore, a NE-verging duplex, likely formed during layer-parallel shortening (LPS) and later verticalized as a result of folding, has been documented (Fig. 27B).

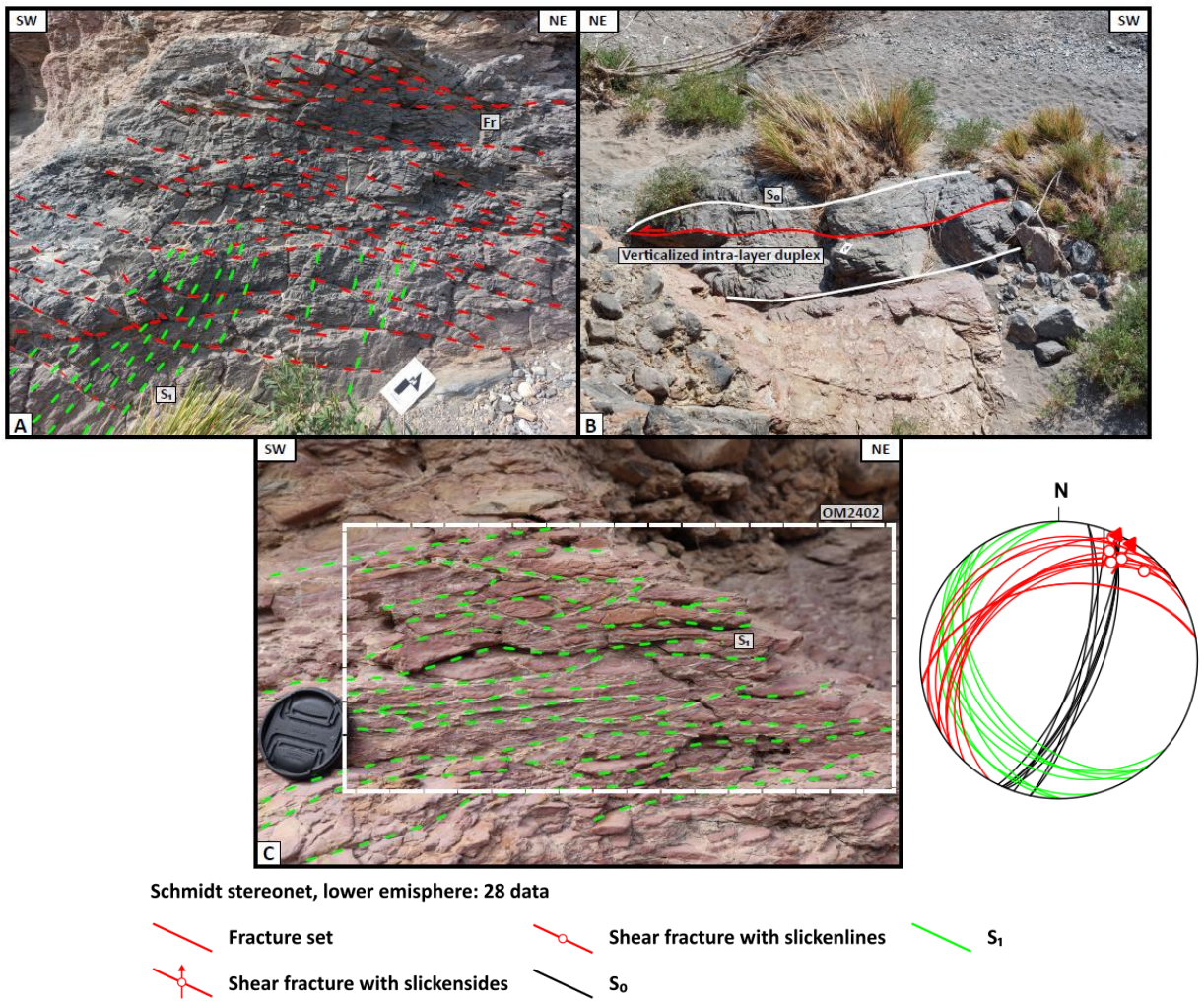

***Figure 27**: Stop 07 - **A**, Angular relationship between Fr and the refracted, high angle S_1 in the carbonate layers; **B**, LPS-related, NE-verging duplex subsequently verticalized due to folding; **C**, Sample OM2402 collected from the densely foliated siliciclastic layers.*

Sample OM2402 was collected from this location (Fig. 27C and Fig. 28A, B). Petrographic analyses revealed that veins mostly contain carbonates, with only minor amounts of quartz. Quartz is instead abundant within the fine, foliated matrix, defined by the alignment of phyllosilicates and opaque minerals, most likely oxides.

The carbonate veins are characterised by common acicular textures, which, based on the commonly reported habit of aragonite in veins, might suggest its presence (Fig. 28C). This has been observed exclusively within the veins that are sub-parallel to the foliation (Fig. 28D). Additionally, crack-and-seal textures are common in the largest veins, showing that older aragonite veins have been reopened, with calcite sealing the later dilation increments (Fig. 28E). Finally, different generations of later, calcite veins crosscut each other, suggesting that calcite veins perpendicular to S_1 cut across calcite veins parallel to it (Fig. 28F).

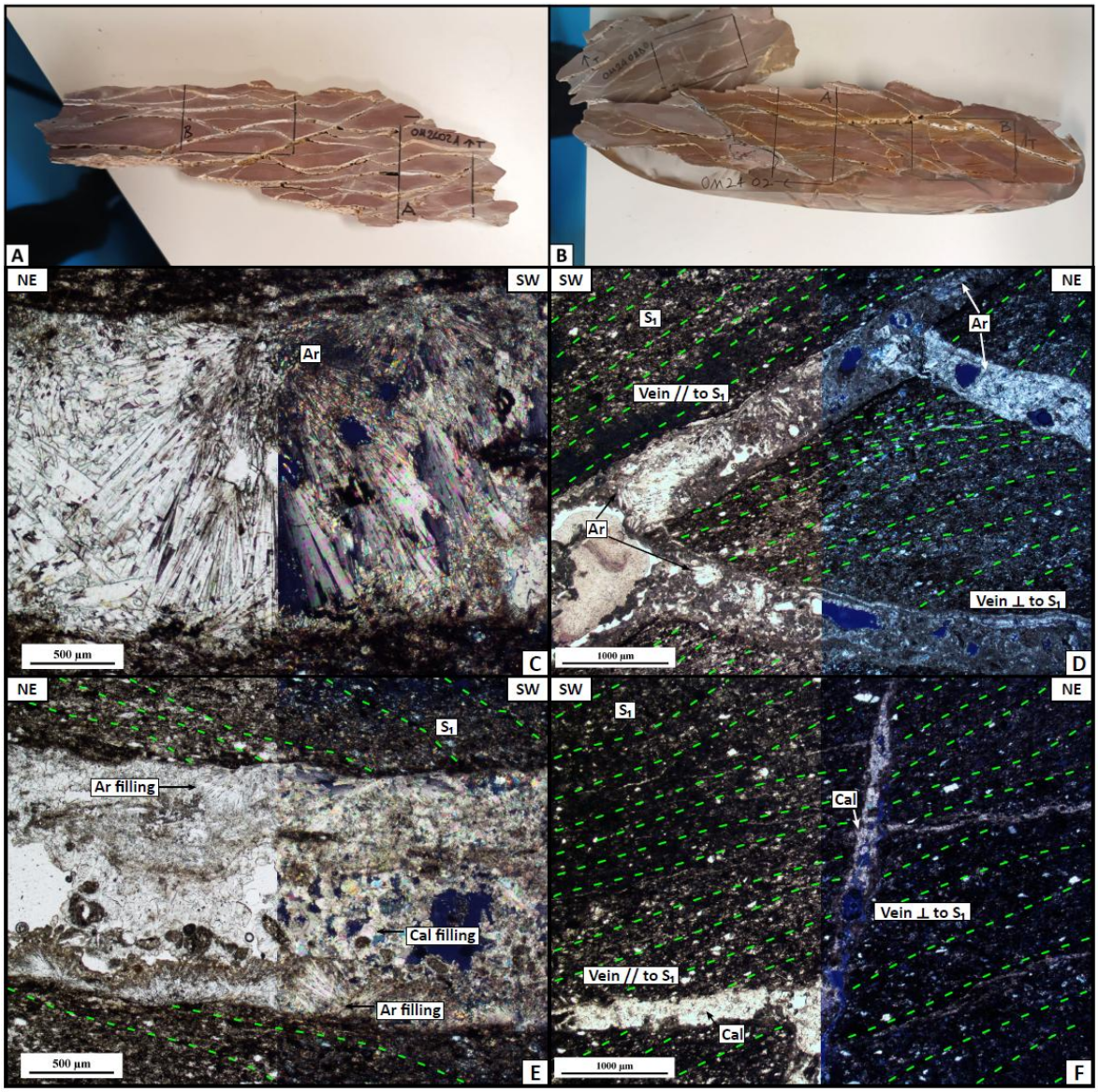

***Figure 28**: **A**, Thin section positions for sample OM2402A; **B**, Thin section positions for samples OM2402C and OM2402D; **C-F**; Thin section photos, plane (left) and crossed-polarized light (right), thin sections were cut perpendicular to S_1 (Z parallel to the pole of the foliation); **C**, Aragonite crystals characterized by the typical acicular texture, from thin section OM2402Ab; **D**, Spatial relationship between veins running parallel and perpendicular to S_1 (green), both containing aragonite, from thin section OM2402D; **E**, Crack-and-seal textures with older aragonite veins associated with younger calcite-vein, from thin section OM2402Ab; **F**, Later calcite vein generations, with those approximately perpendicular to S_1 cutting across those ones subparallel to it.*

3.1.8 - STOP 08 (23°14’57.17’’N; 57°25’58.76’’E)

Here the Mu’aydin Formation lithotype is similar to that observed at Stop 07, and a gentle fold with a gently NE-plunging axis is documented (Fig. 29D). To the SW of the hinge zone, the angle between S_0 and S_1 decreases (Fig. 29A), while the refraction of S_1 in the more competent carbonate beds is once again evident (Fig. 29B). Another vertically reoriented, NE-verging duplex structure is present (Fig. 29C). A tectonic contact is suspected where carbonate layers terminate abruptly (Fig. 29D).

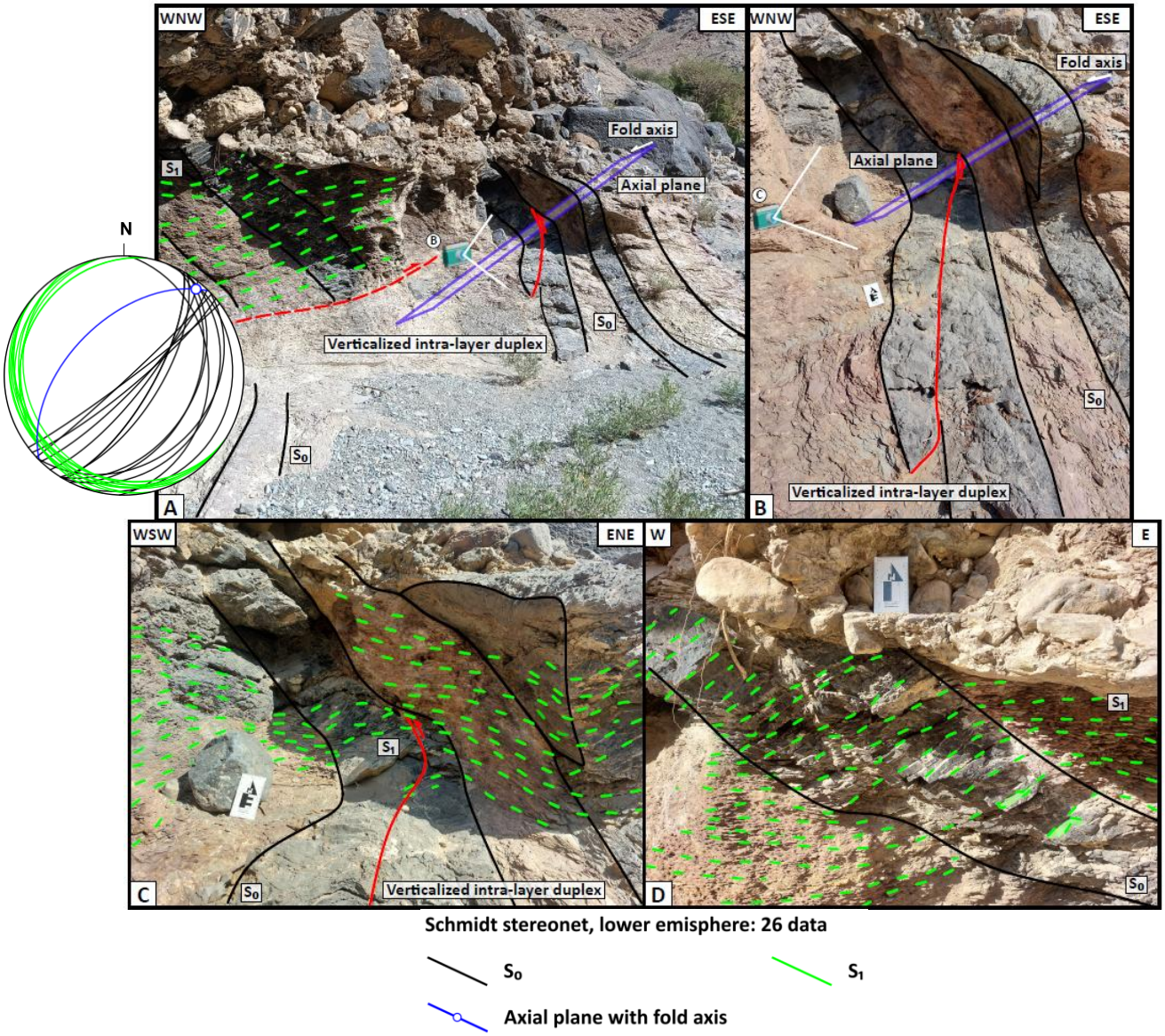

***Figure 29**: Stop 08 - **A**, Fold with a gently NE-plunging axis associated with a possible tectonic contact responsible for the interruption of the carbonate layers; **B**, NE-verging duplex, now verticalized due to post-thrusting folding; **C**, Spatial relationship between S_0 (black) and S_1 (green); **D**, High angle S_1 refracted in more competent carbonate layers.*

3.1.9 - STOP 09 (23°14’56.84’’N; 57°25’58.10’’E)

Here, the lack of distinguishable carbonate layers and the similarity in orientation between S_0 and S_1 complicate the structural analysis at the outcrop. Two distinct sets of conjugate veins have been observed (Fig. 30). Structurally, these veins are consistent with the orientation of the S_1 cleavage, suggesting synchronous formation under the effects of a horizontal σ_1 stress axis (that is, thrusting, in this case).

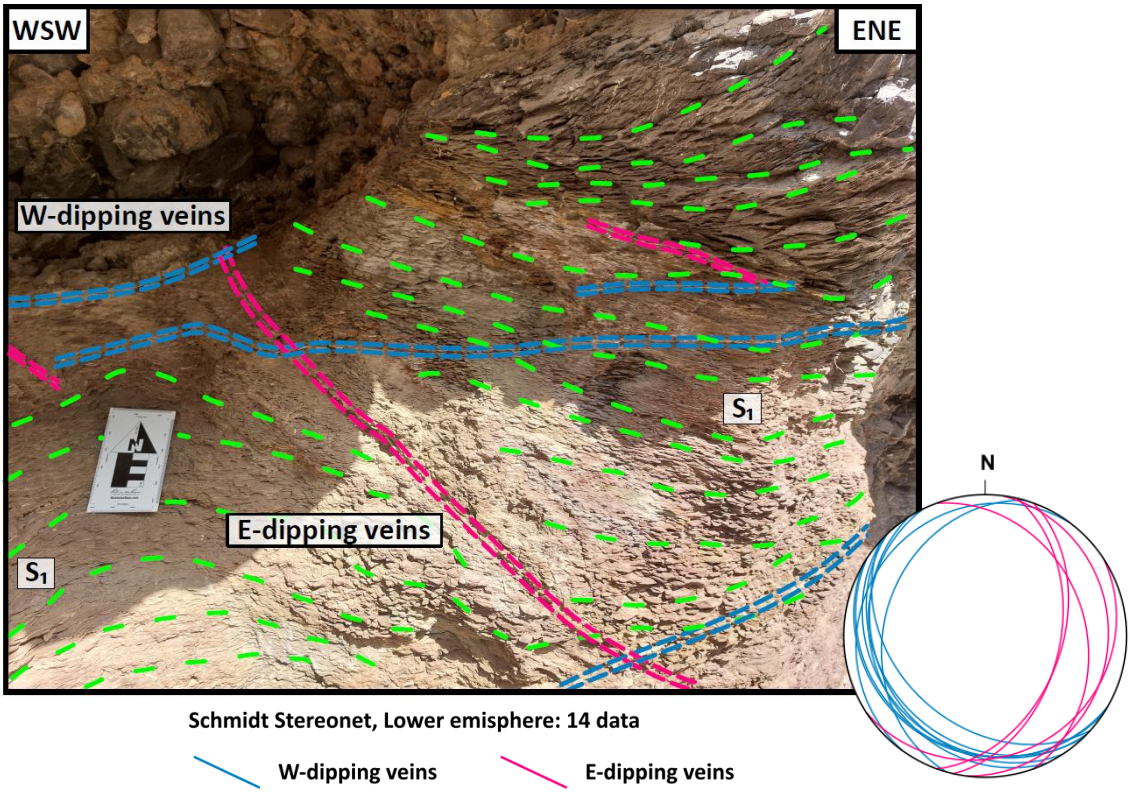

***Figure 30**: Stop 09 - Conjugate vein sets characterized by W-dipping veins (blue) and E-dipping veins (pink), respectively, associated with S_1.*

3.1.10 - STOP 10 (23°14’56.58’’N; 57°25’57.50’’E)

Here, close to the contact with the Hajir Formation, carbonates become once again the dominant lithotype of the Mu’aydin Formation, characterized by pervasively foliated, terrigenous-rich calcilutites. The easternmost part of the station is characterized by subvertical bedding (Fig. 31B). Instead, in the westernmost part of the outcrop S_0 becomes nearly indistinguishable within the siliciclastic layers, and a single visible thin competent carbonate layer helps distinguish S_0 at the outcrop (Fig. 31A). Another asymmetric fold, similar to that reported from Stop 08, has been found here, featuring a gently NNE-plunging fold axis, a long back-limb, and a short front-limb. This fold set will be referred to as “F_1” in the subsequent discussion. Moreover, parasitic folds are well developed, arising from the rheological contrast between adjacent layers (Fig. 31C).

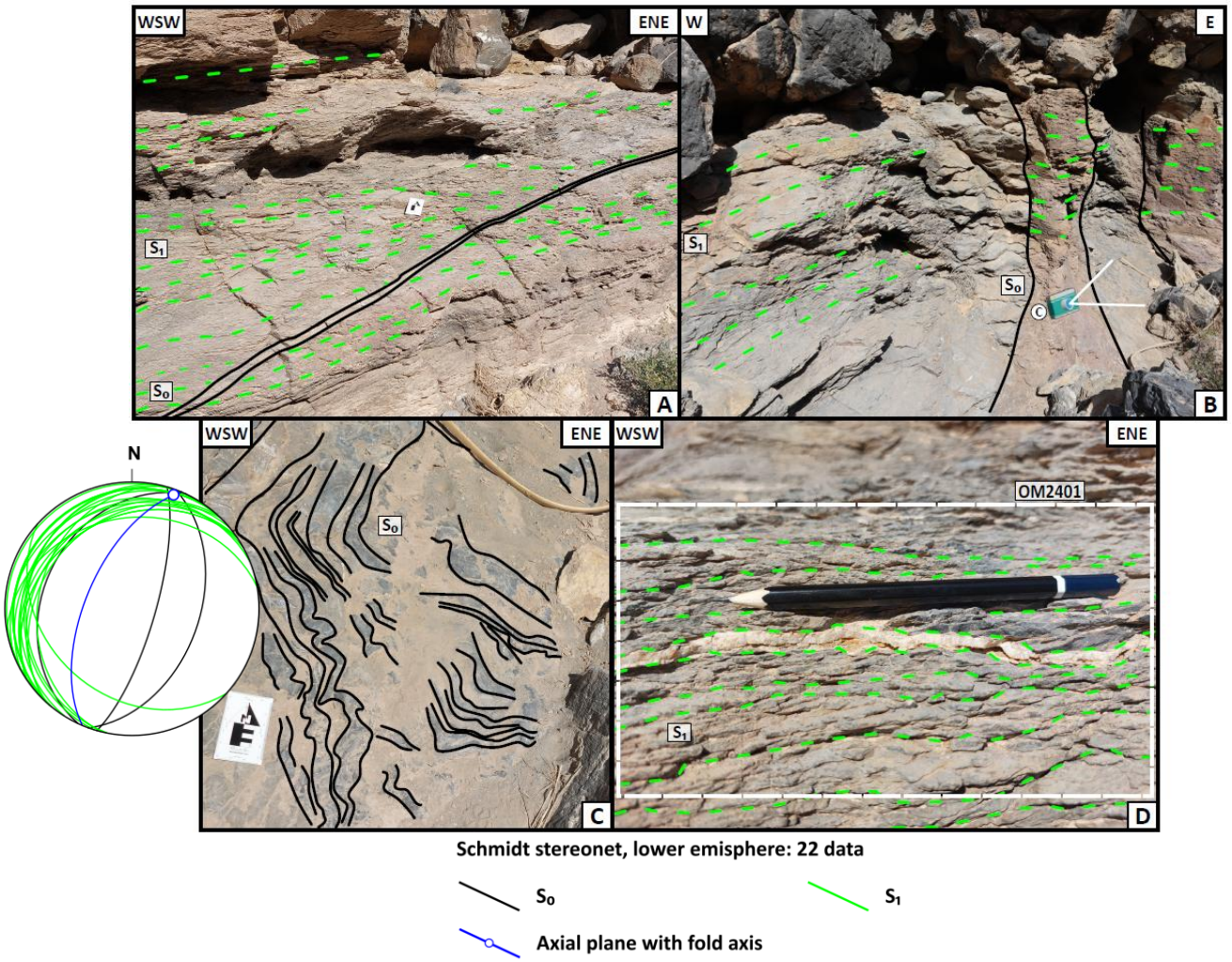

***Figure 31**: Stop 10 - **A**, Thin, competent carbonate layer evident in the westernmost part of the Stop; **B**, Subvertical layers located in the easternmost part of the stop; **C**, Secondary, parasitic folds due to the rheological contrast between siliciclastic and more competent carbonate layers; **D**, Sample OM2401, collected from the pervasively foliated siliciclastic layers.*

Sample OM2401 comes from this location (Fig. 31D and Fig. 32A, B). Petrographic analyses revealed the presence of carbonate veins containing also microcrystalline and fibrous quartz, all hosted within a foliated matrix rich in carbonate clasts, quartz, and oxides. Isolated mica crystals occur both within the matrix and along the vein boundaries.

The characteristic acicular aspect of carbonates again suggests the presence of aragonite. However, this appears to be less abundant compared to the samples from Stop 07. Additionally, crack-and-seal textures with older aragonite infilling coupled with younger calcite have been observed, both associated with younger fibrous quartz-filled veins (Fig. 32C). Calcite veins are more abundant, usually parallel to S_1, and exhibit a massive to elongate-massive texture, likely the result of syntaxial growth (Fig. 32E); finally, they are occasionally cross-cut by younger quartz veins (Fig. 32D).

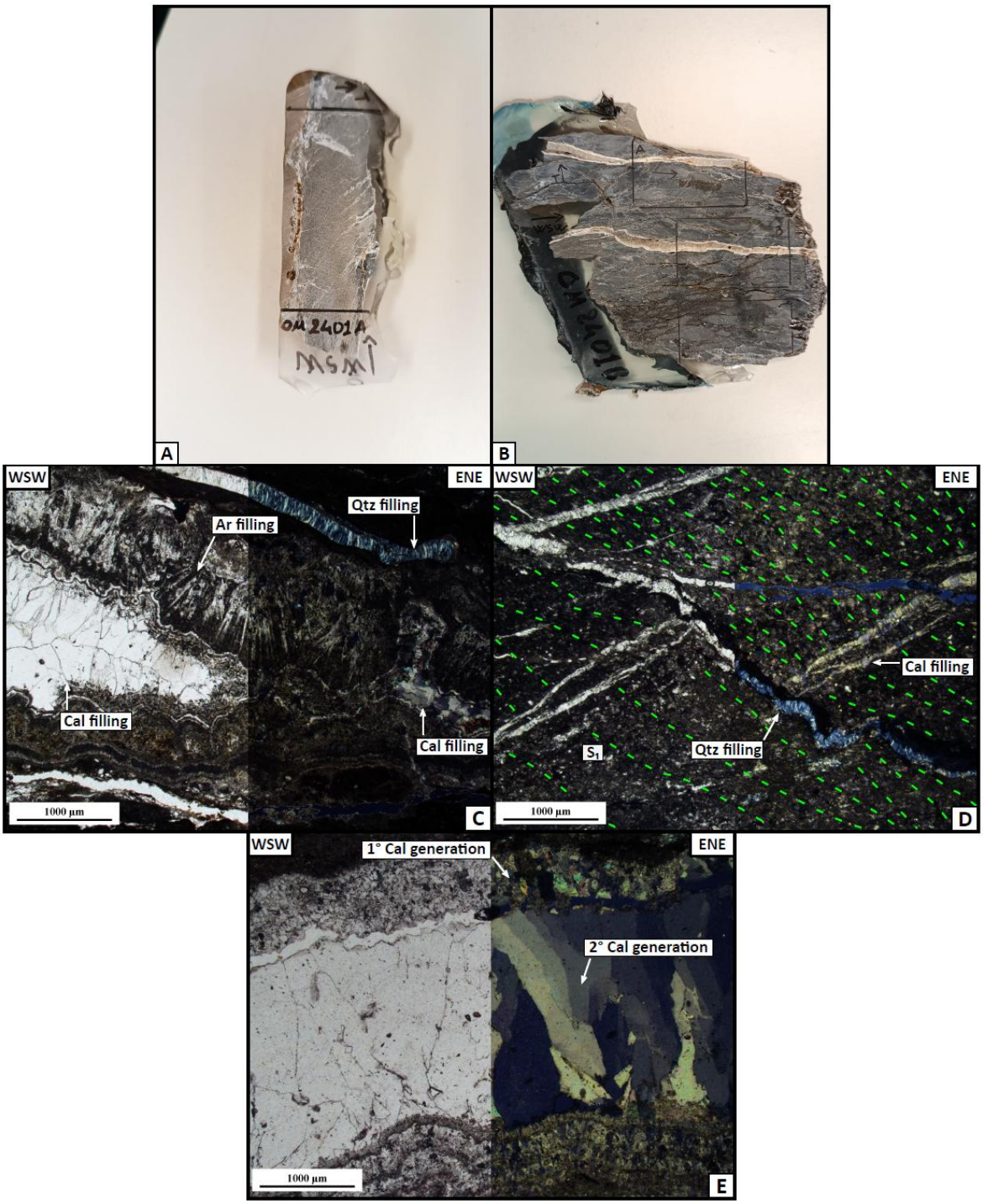

***Figure 32**: **A**, Thin section position for sample OM2401A; **B**, Thin section positions for sample OM2401B; **C-E**; Thin section photos, plane (left) and crossed-polarized light (right), thin sections were cut perpendicular to S_1 (Z parallel to the pole of the foliation); **C**, Crack-and-seal textures with older aragonite associated with younger calcite, both associated with younger fibrous quartz veins, from thin section OM2401Ba; **D**, Quartz veins, parallel to S_1 (green), crosscut older calcite-filled veins perpendicular to S_1, from thin section OM2401Ba; **E**, Crack-and-seal textures evident within calcite veins, with older massive filling associated with elongated-massive younger filling, from thin section OM2401Bb.*

3.1.11 - STOP 11 (23°14’55.13’’N; 57°25’56.54’’E)

At this location, the Hajir Formation crops out. Although the contact with the Mu’aydin Formation is not exposed at the surface, as it remains buried below slope deposits, the fact that the Hajir Formation, which is stratigraphically older than the Mu’aydin Formation, is there structurally above it suggests that the contact between the two units is tectonic in nature and, specifically, a thrust fault. The latter has been renamed ‘Little Snake Gorge Thrust.’ Furthermore, a second subsidiary thrust sharply cuts through the folded carbonate layers within the Hajir Formation, which define a large-scale, NE-verging, tight anticline (Fig. 33A, B). More than one small-scale shear zone has been observed near the tectonic contact, both on the western and eastern flanks of the Little Snake Gorge. These are associated with asymmetric folds and multiple vein sets (Fig. 33C, D). On the western flank, sigmoidal structures (Fig. 33C) and slickensides are associated with small-scale, SW-dipping shear zones, indicating a dextral sense of shear and a top-to-NE transport direction. On the eastern flank, asymmetric, NE-verging folds are characterized by long back limbs, short front limbs, and gently SSW to SE-dipping axial planes, thus being geometrically compatible with the F_1 folds. They are often associated with NE-verging mylonitic to ultra-mylonitic shear zones (Fig. 33D).

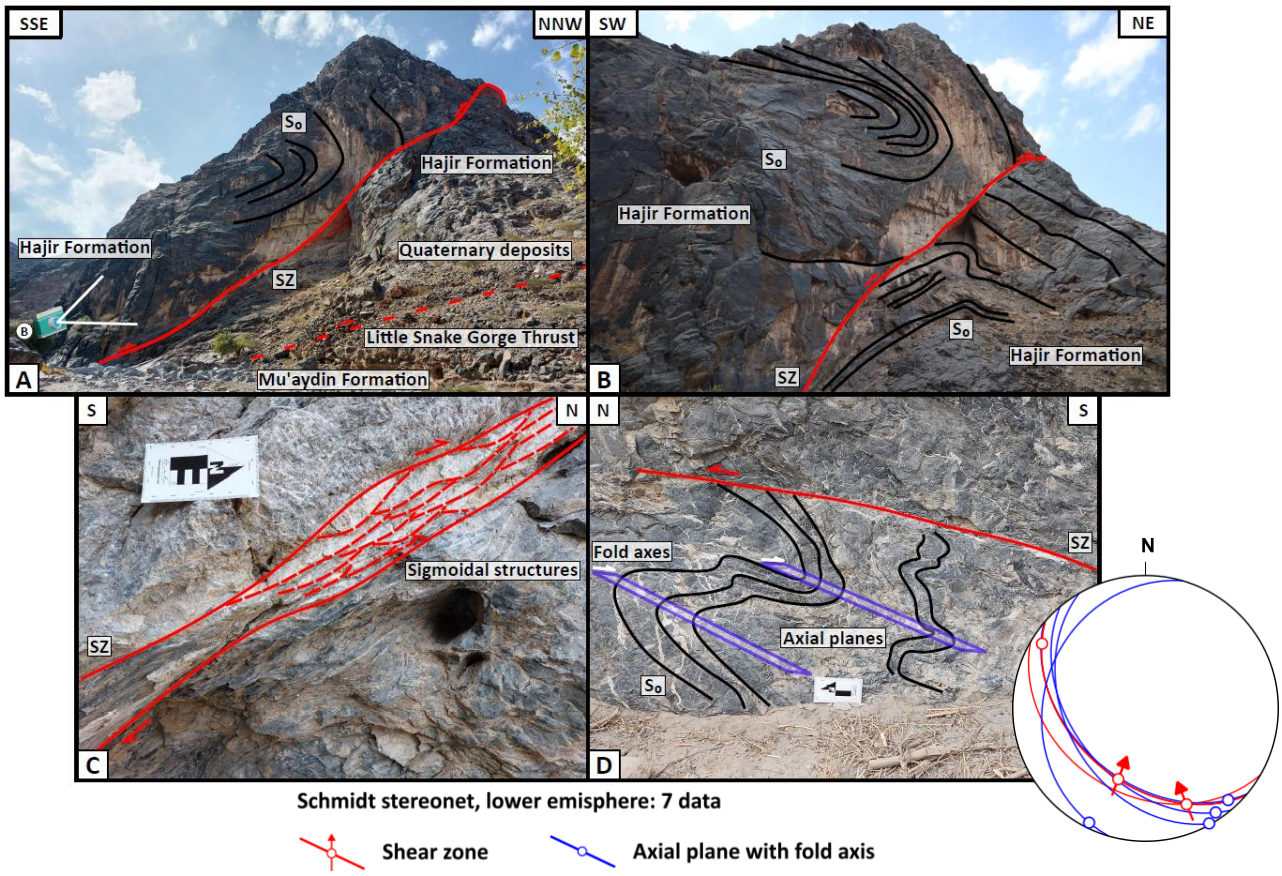

***Figure 33**: Stop 11 - **A**, Location of the Little Snake Gorge Thrust, buried beneath slope deposits and associated with a large-scale subsidiary thrust; **B**, Detail of the subsidiary thrust and the folded S_0; **C**, Small-scale NE-verging shear zone (SZ) at the base of the subsidiary thrust within the Hajir Formation on the western bank of the wadi; **D**, NE-verging shear zone (SZ) within the Hajir Formation on the eastern bank of the wadi, associated with NE-verging folds characterized by axial planes gently dipping toward the SW.*

Four sets of veins were distinguished based on their orientation and cross-cutting relationships. The first set, “V_1”, is oriented NNE-SSW and has been interpreted as associated with shear zones and is subparallel to them.

These veins are often involved in and reactivated by the shear zones themselves (Fig. 34A). The second set, "V_2", crosscuts the first and is oriented approximately NW-SE (Fig. 34A). The third set, "V_3", also approximately perpendicular to the shear zones, appears to cut across both V_1 and V_2, and trends roughly WNW-ESE (Fig. 34B, C, D). The last set, "V_4", appears to be associated with the reactivation of the first one, exploiting pre-existing planes of weakness and resulting in the development of crack-and-seal textures with a new generation of mineral infill (Fig. 34A, B, D). Based on crosscutting relationships and the orientations of the first three vein sets, a progressive clockwise rotation in time of the principal stress axes can be inferred. The transition from the NNE-SSW-oriented veins of set V_1, through the NW-SE-oriented veins of set V_2, to the WNW-ESE-oriented veins of set V_3 suggests a systematic reorientation of the maximum compressive stress axis σ_1, likely within a persistent compressional tectonic regime. The fourth set V_4, sub-parallel to the first, instead appears to exploit pre-existing weaknesses within the rock volume.

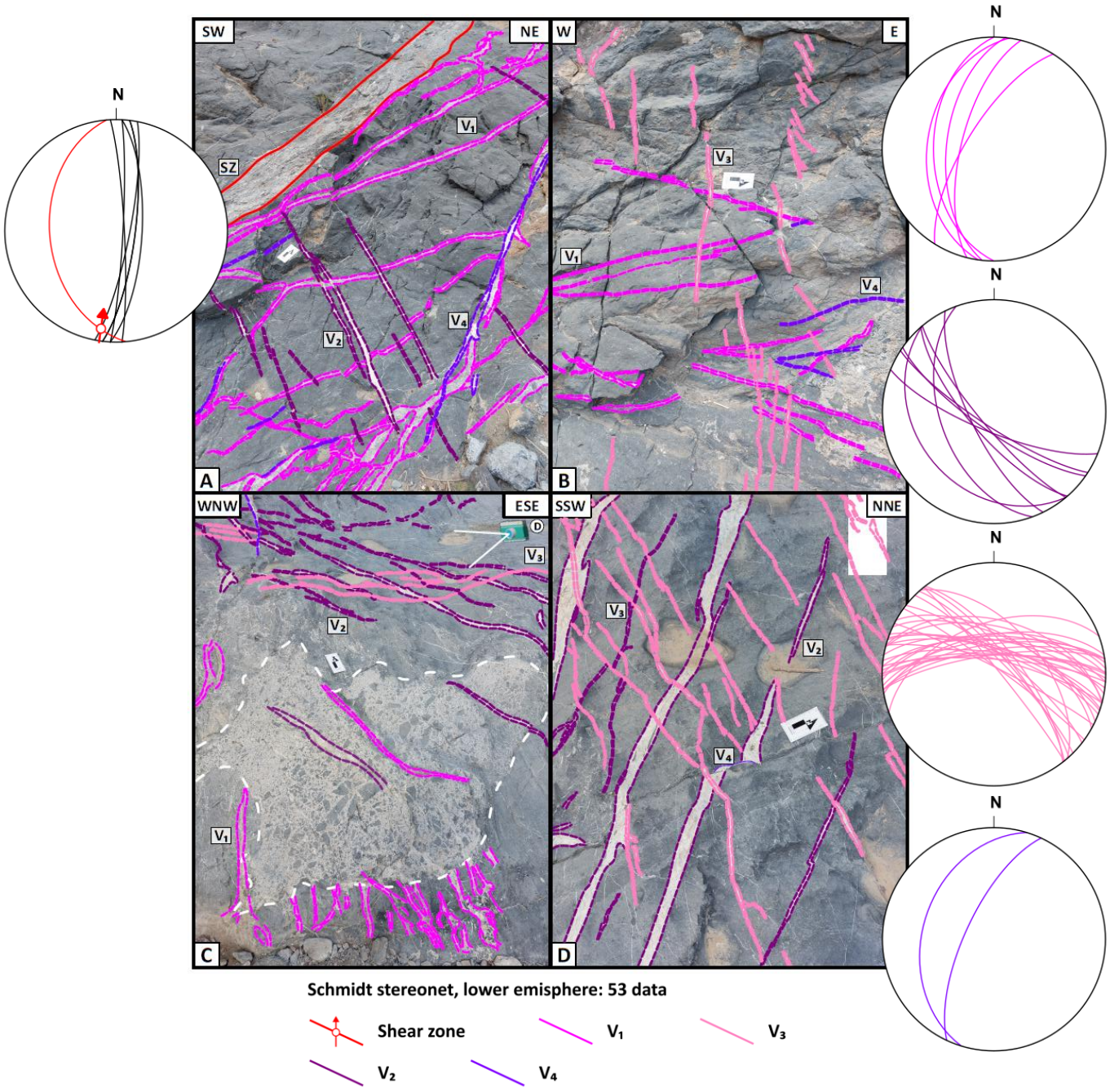

***Figure 34**: Stop 11 - **A**, Spatial relationships between a mylonitic shear zone (SZ), V_1, V_2, and V_4; **B**, Spatial relationships between V_1, V_3, and V_4; **C**, Spatial relationships between V_1, V_2, and V_3, associated with an hydrofracture breccia; **D**, Spatial relationships between V_2, V_3, and V_4.*

Additionally, the role of fluids and associated pore pressure conditions during tectonic deformation is highlighted by the presence of chaotic hydro fracture breccias, whose formation was likely favoured by the permeability contrast between the Hajir and the Mu'aydin Formation (Fig. 34C).

3.2 - RAMAN ANALYSES

Raman spectroscopy analyses were conducted to verify the presence of aragonite in the selected samples from the Mu'aydin Formation of the Little Snake Gorge outcrop (reported for the first time by Zuccari et al., 2023) and to estimate the peak temperature recorded by graphite. Specifically, RSCM (Raman Spectroscopy on Carbonaceous Material) has been performed on microscopic graphite flakes that coexist with and are included in quartz and carbonate crystals within the host rock or veins parallel to the foliation. The inspected thin sections are OM2401A, OM2401Ba, OM2401Bb, OM2401Bc, OM2402Aa, OM2402Ab, OM2402Ca, OM2402Cb. Since the estimated temperatures of the samples reside within the classification of "medium-grade carbonaceous material", as defined by Kouketsu et al. (2014), two methods have been utilised to calculate the peak temperature of the samples.

Estimates derived from the low-temperature calibration of Lahfid et al. (2010) yielded an average temperature of 365 ± 8 °C, whereas application of the high-temperature calibration of Aoya et al. (2010) produced an average estimate of 330 ± 6 °C. All graphite Raman spectra and their corresponding temperature estimates are provided in Appendix (Appx. 1-21), while the table summarizing the average temperature values obtained from each thin section, with both methods, is shown below (Table 2):

	Method by Lahfid et al. (2010)	**Method by Aoya et al. (2010)**
OM2401A	367 ± 14	327 ± 10
OM2401Ba	361 ± 14	313 ± 18
OM2401Bb	324 ± 5	335 ± 17
OM2401Bc	341 ± 9	363 ± 16
OM2402Aa	390 ± 26	329 ± 19
OM2402Ab	395 ± 32	323 ± 14
OM2402Cb	375 ± 26	330 ± 12
Average	365 ± 8	330 ± 6

***Table 2**: Summary table of the analyzed thin sections and of the temperatures calculated through the low-temperature method proposed by Lahfid et al. (2010) and the high-temperature method proposed by Aoya et al. (2010), with the calculated standard deviations being ± 2σ.*

The probability distribution functions, calculated for each thin section, are shown below (Fig. 35A, B, C, D, E, F, G). The dispersion in the calculated temperatures can be attributed to both experimental uncertainties during the spectra acquisition and during the peak-fitting process with Lorentz and Voigt functions, which are used for the low-temperature and high-temperature methods, respectively.

The results of both methods fall in the "medium-grade carbonaceous material" category as defined by Kouketsu et al. (2014). These temperature values range between the respective reliability intervals of the two employed analytical methods, thereby reducing the precision of the estimates. Consequently, the discussion below will consider an average of 350 °C derived from the temperature values obtained using the two distinct methods, while an uncertainty margin of ± 50 °C, usually associated with RSCM, should be considered in the interpretation of the data, regardless of the smaller intrinsic deviation of each thin section.

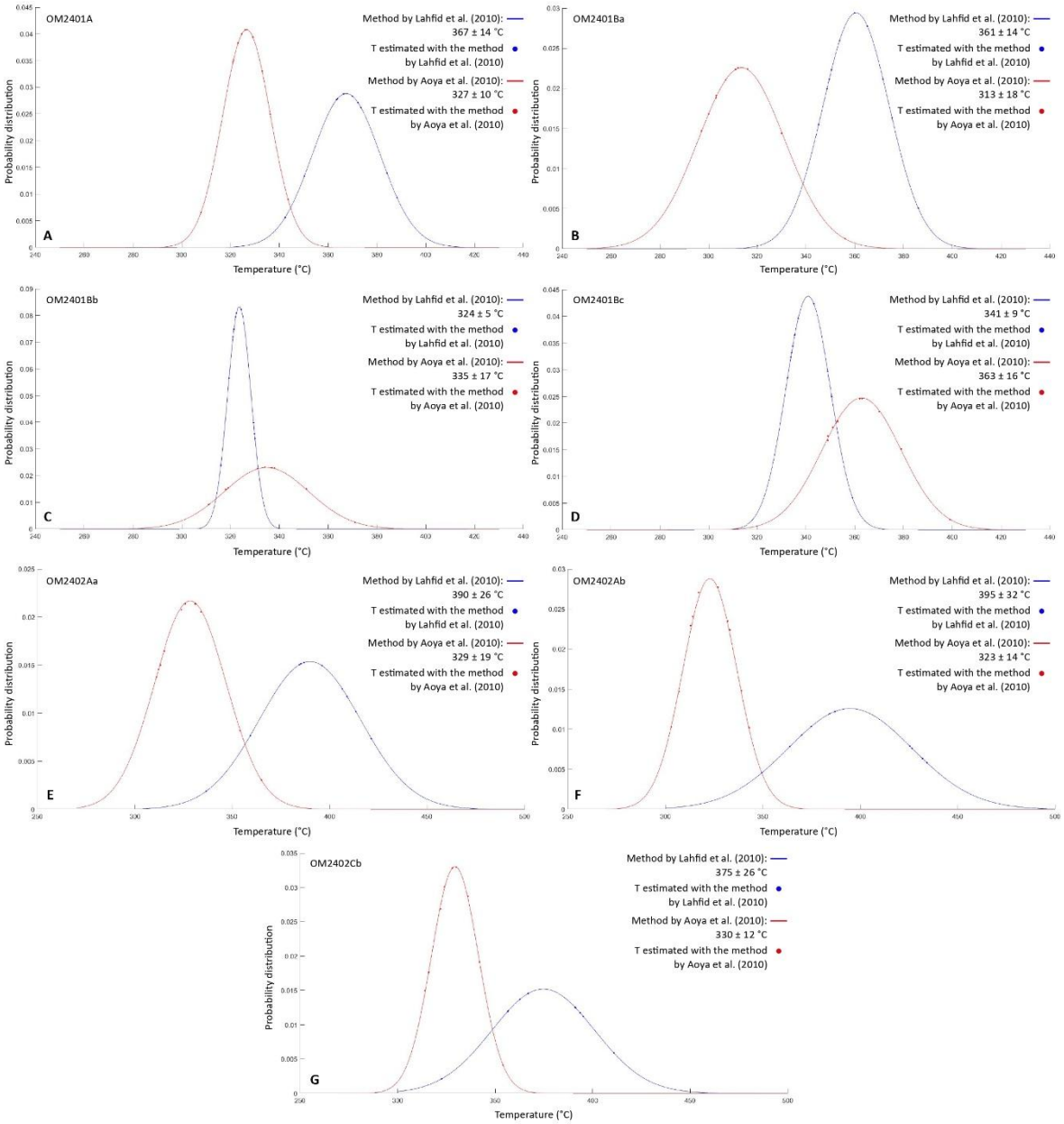

Figure 35*: Probability distributions of the RSCM estimated temperatures, calculated with the methods by Lahfid et al. (2010) (blue curve) and Aoya et al. (2010) (red curve), for the following thin sections:* ***A****, OM2401A;* ***B****, OM2401Ba;* ***C****, OM2401Bb;* ***D****, OM240Bc;* ***E****, OM2402Aa;* ***F****, OM2402Ab;* ***G****, OM2402Cb.*

Similar qualitative techniques have been applied to verify the presence of aragonite in several samples. Every thin section has been checked: however, aragonite occurrence has been confirmed only in the following thin sections: OM2402Aa, OM2402Ab, OM2402Ca, OM2402Cb (Fig. 36B, C, D, E, F, G, H, I). Spectrum acquisition has been problematic for thin section OM2401Ba most likely because of the mechanical interference generated while cutting the thin section and because of the chemical weathering of the veins, leading to intense fluorescence. Even if no useful Raman spectra were obtained, its presence in this thin section can be concluded due to the occurrence of the typical acicular texture of the carbonate (Fig 36A).

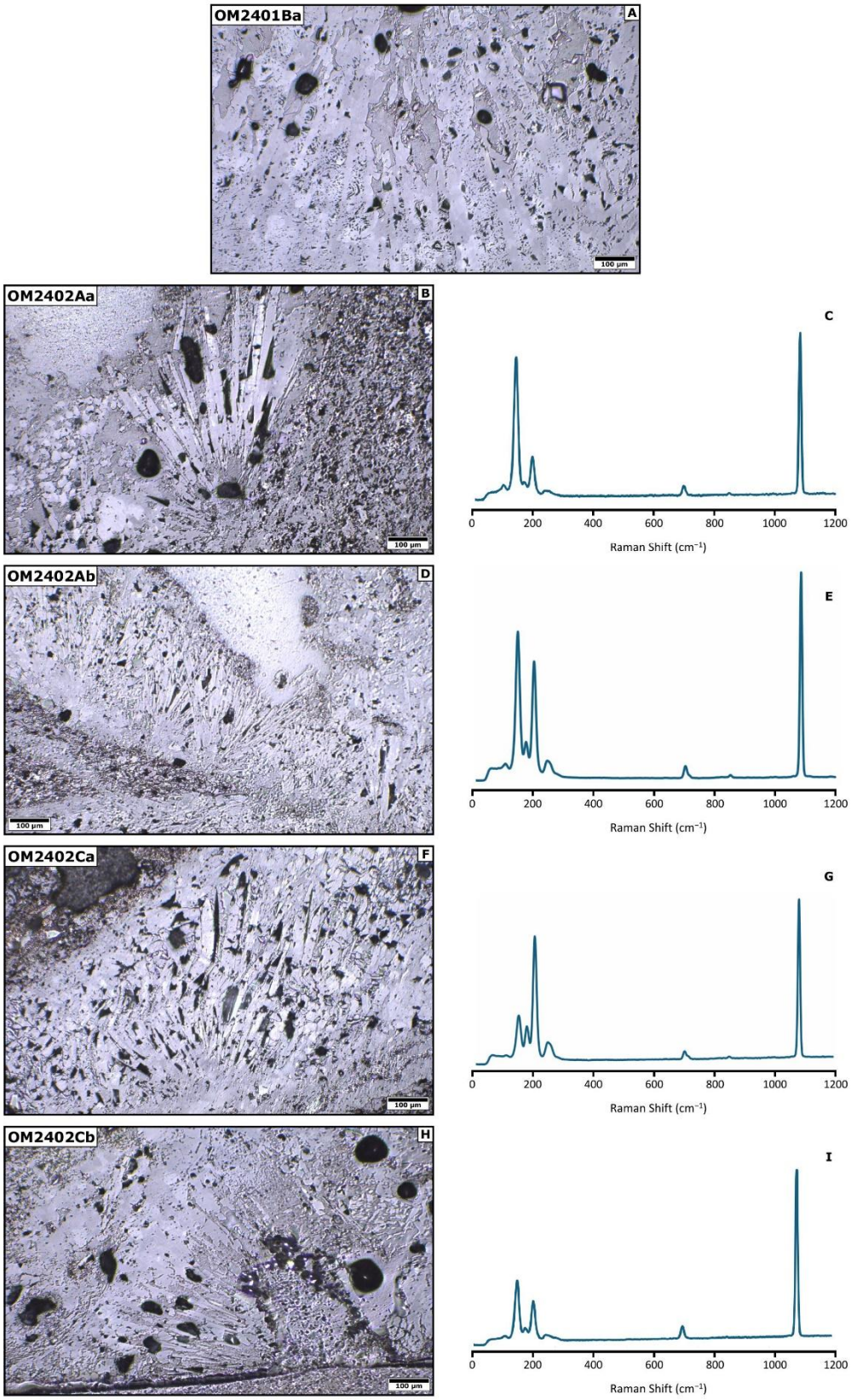

***Figure 36**: **A**, Raman image of the possible aragonite present in the thin section OM2401Ba; **B**, Raman image of the aragonite present in the thin section OM2402Aa; **C**, Related Raman spectrum for the thin section OM2402Aa; **D**, Raman image of the aragonite present in the thin section OM2402Ab; **E**, Related Raman spectrum for the thin section OM2402Ab; **F**, Raman image of the aragonite present in the thin section OM2402Ca; **G**, Related Raman spectrum for the thin section OM2402Ca; **H**, Raman image of the aragonite present in the thin section OM2402Cb; I, Related Raman spectrum for the thin section OM2402Cb.*

Assuming a metamorphic rather than sedimentary origin for the documented aragonite, this finding not only provides important constraints on the pressure conditions prevailing during the formation of the veins but also places relative geochronological constraints upon the deformation phase responsible for their development.

Considering the stability range of calcite and aragonite, alongside the identification of possible metamorphic aragonite within veins in the Mu'aydin Formation of the Little Snake Gorge area and thermal insights obtained from graphite within the latter, my results provide the basis for inferring the minimum pressure–temperature conditions under which the foliation planes-filling veins developed.

With the temperature estimate of c. 365 ± 8 °C obtained from the method by Lahfid et al. (2010), a pressure of c. 0.89 ± 0.04 GPa would be required to transform calcite in aragonite. Differently, with the temperature estimate of c. 330 ± 6 °C obtained from the method by Aoya et al. (2010), a pressure of c. 0.82 ± 0.04 GPa would allow the transformation.

Considering c. 348 ± 50 °C as the average value between temperatures obtained from both methods, calcite would have required c. 0.85 ± 0.12 GPa to transform into aragonite (Fig. 37). Minimum depth estimates between 32 and 42 km can, therefore, be inferred from the estimated pressure values, under the assumption of standard lithostatic gradients.

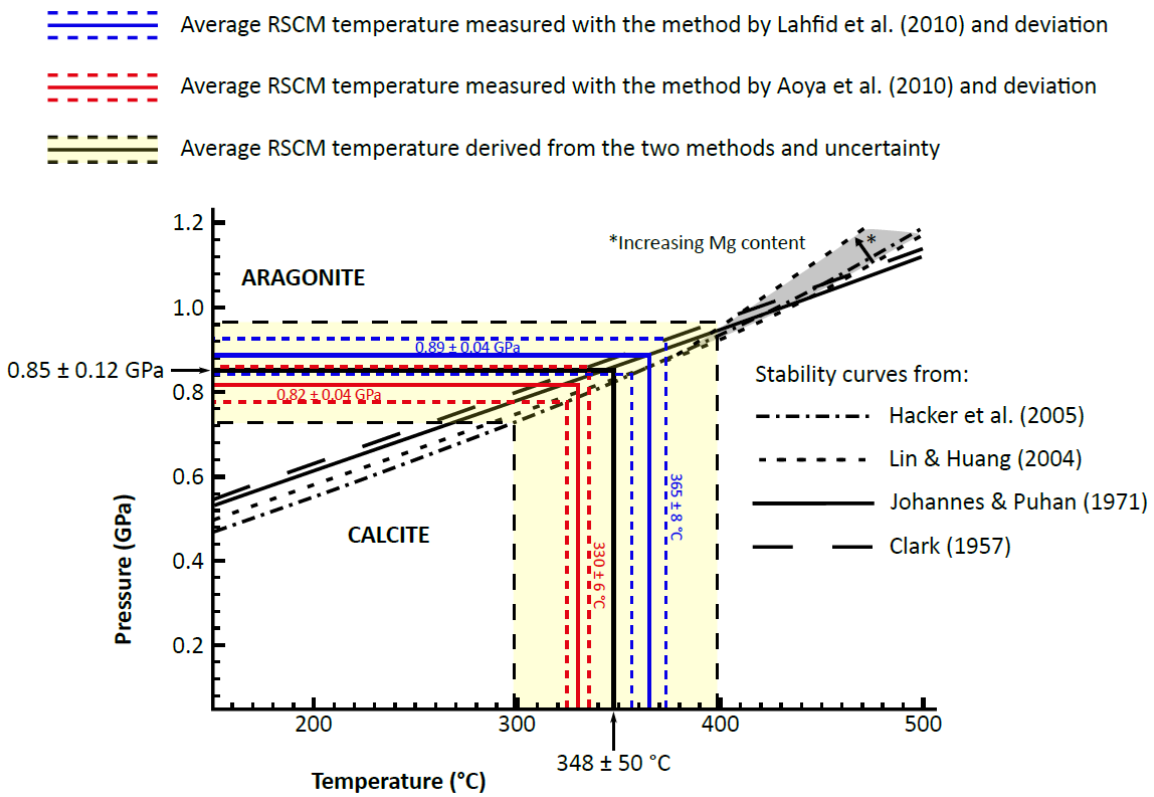

***Figure 37**: Stability diagram of calcite and aragonite with the plotted average RSCM temperature measured with the Lahfid et al. (2010) (blue line) and the Aoya et al. (2010) (red line) methods and the average of the single temperatures obtained from both methods (black line), associated with their relative deviations (redrawn and modified after Zuccari et al., 2023).*

The estimated P-T conditions thus constrain the Mu'Aydin Formation in the footwall of the Little Snake Gorge thrust to the lower blueschist metamorphic facies field (Fig. 38), at conditions virtually identical to those obtained by Zuccari et al. (2023) for the Hajir carbonates in the immediate hanging wall.

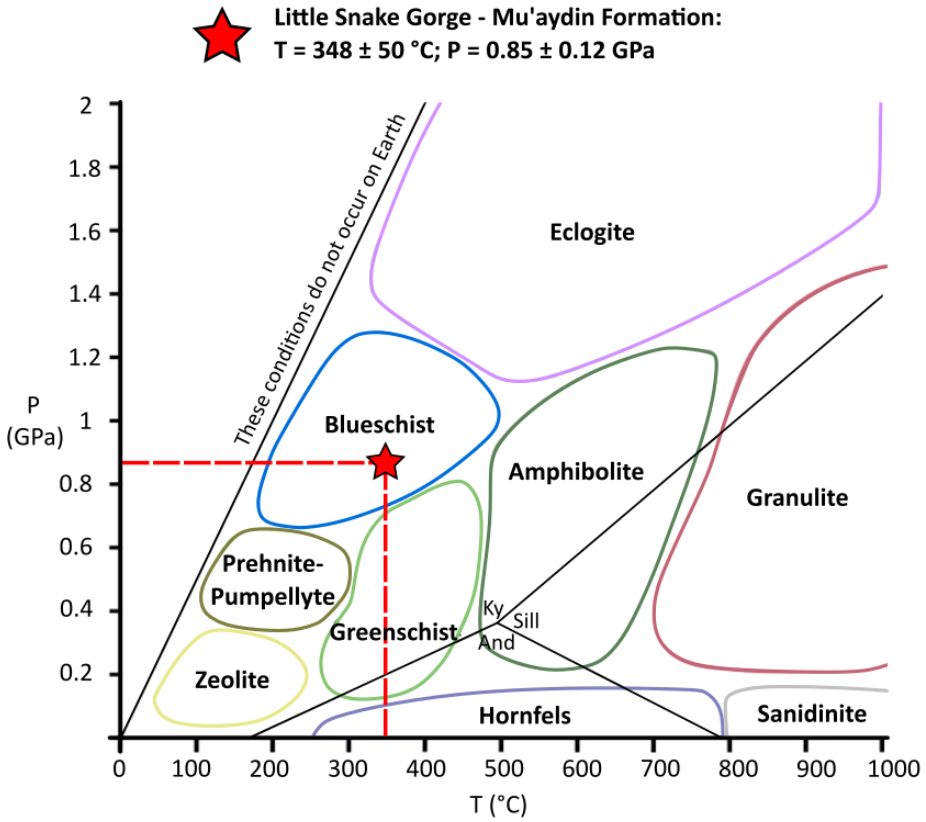

***Figure 38**: P-T diagram of the different metamorphic facies, with the red star indicating the pressure-temperature conditions measured in the Little Snake Gorge outcrop (redrawn and modified after Ozcan et al., 2019).*

CHAPTER 4 - INTERPRETATION OF THE OBTAINED RESULTS AND DISCUSSION

The principal aim of the field study of the Little Snake Gorge Thrust was to conduct the high-resolution structural characterization of deformation features preserved across the entire outcrop (Fig. 39), integrating observations at both microstructural and mesoscale levels. Systematic structural data on the geometry and kinematics of all identified tectonic structures were acquired and subsequently integrated with Raman Spectroscopy of Carbonaceous Material (RSCM) thermometry to constrain peak metamorphic temperatures and infer the associated pressure conditions during deformation.

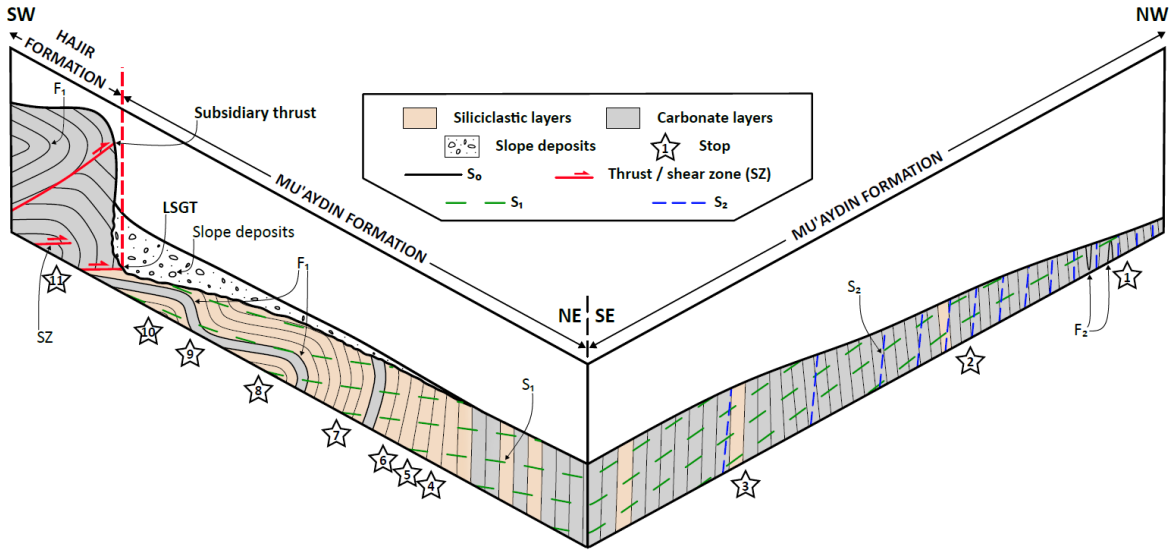

***Figure 39**: Fence diagram of the Little Snake Gorge section, summarizing the main deformation features documented during the structural survey, not to scale; LSGT: Little Snake Gorge Thrust.*

The ultimate objective of this thesis is to compile the structural and metamorphic datasets within a single, unified interpretative framework to constrain the metamorphic and deformational conditions that governed the emplacement of the Hajir Formation over the Mu'aydin Formation via thrusting, as well as the development of aragonite vein networks that exploited the foliation formed during the high-pressure thrusting-related metamorphic stages. Furthermore, given the remarkable bearing of documenting HP conditions within the Jabal Akhdar Dome, a consistent geodynamic model that reconciles the observed deformation patterns with the recorded metamorphic evolution of the Little Snake Gorge Thrust is provided. These observations and interpretations are thus used to further elaborate upon the regional-scale implications of the results obtained to achieve a more comprehensive understanding of the tectonometamorphic evolution of the Jabal Akhdar Dome during the long geological history of the Arabian passive margin.

4.1 - LITTLE SNAKE GORGE THRUST EVOLUTION AND VEIN FORMATION UNDER BLUESCHIST FACIES CONDITIONS

Recognizing and analysing evidence of high-pressure mineral assemblages in exhumed metamorphic rocks is essential for reconstructing the pressure-temperature paths and deformation mechanisms associated with subduction zones (e.g., Agard et al., 2009; Rubatto et al., 2011; Zuccari et al., 2023), which are otherwise impossible to observe directly. The preservation potential of these assemblages depends on a complex interplay of factors, including the exhumation dynamics and the regional thermal regime, both of which influence the extent of retrograde transformations (Zuccari et al., 2023).

Additionally, fluid availability and composition can facilitate mass transfer and drive/enhance mineral reactions throughout metamorphic evolution, while strain intensity and the specific mineral assemblages involved also govern the potential for relict preservation (e.g., Goffé & Velde, 1984; Zuccari et al., 2023).

Structural evidence from exhumed subduction complexes demonstrates that thrust zones developed under blueschist-facies conditions may accommodate the coexistence of brittle and ductile deformation features. Brittle shear veins, locally embedded within a blueschist continuous matrix, frequently grade into discrete ductile shear zones, indicating synchronous frictional-viscous deformation processes (e.g., Behr & Burgmann, 2021; Muñoz-Montecinos et al., 2021; Zuccari et al., 2023). Alternating episodes of fracturing and viscous flow under high-pressure conditions, along with the development of a pervasive foliation-parallel permeability structure, generally enhance fluid mobility along the shear zones, which consequently acted as transient high-permeability pathways (e.g., Molli et al., 2017; Zuccari et al., 2023). These data support a deformation model wherein alternating brittle failure and viscous creep are accommodated along thrust interfaces under high-pressure, low-temperature conditions, facilitated by elevated pore-fluid pressures. This typically results in a complex structural fabric characterized by the mutual and cyclic overprinting of metamorphic foliations, cataclastic zones, and vein networks within blueschist-facies shear zones (Muñoz-Montecinos et al., 2021).

The Little Snake Gorge Thrust, along with its associated tectono-metamorphic conditions, has not previously been investigated in these terms, but stands as an extraordinary example of this complexity. As outlined in the previous chapters, occurrences of aragonite have been documented in both the hanging wall and the footwall of the thrust, within the Hajir and the Mu'aydin Formations, respectively. Considering the metamorphic origin of aragonite as documented by Zuccari et al. (2023), it is reasonable to attribute the aragonite found in the Mu'aydin Formation to the same formation mechanism, excluding an Ediacaran sedimentary origin because of its unlikely preservation over such a long period due to the rapid kinetics of the aragonite-calcite transformation (e.g., Hacker et al., 2005; Zuccari et al., 2023).

Thanks to Raman spectroscopy on carbonaceous material (RSCM), temperature and pressure estimates constrain synkinematic blueschist facies metamorphic conditions for both the hanging wall and the footwall of the Little Snake Gorge Thrust, that likely reached these metamorphic conditions during the same deformation phase. The latter has been constrained through U-Pb isotopic dating to the Late Cretaceous subduction of the Arabian passive margin below the Eurasian plate (Zuccari et al., 2023).

The actual offset or the fault trace corrugation are typically required to assess the maturity of a fault (e.g., Manighetti et al., 2021). However, even if the Little Snake Gorge Thrust cannot be directly observed in the field, the latter has been classified as immature and incipient, as it largely preserves the original contact between the two formations without involving any younger units. Both earlier studies and the present work have identified a range of deformation features attributable to the main thrust zone. These structures exhibit, as expected, a broad rheological spectrum, encompassing ductile, semi-ductile, and brittle deformation, consistent with strain localization under blueschist facies conditions. However, the hanging wall and footwall of the thrust have responded differently to the stress regime and are currently characterized by distinct deformation structures and styles.

This thesis confirms the presence of NE-verging shear zones as well as asymmetric folds within the Hajir Formation, as reported by Zuccari et al. (2023). Additionally, further veins have been documented, some of which are associated with earlier shear zones and were subsequently overprinted by them, supporting the hypothesis of cyclic brittle-ductile deformation. The presence of a well-developed network of secondary mylonitic shear zones at the base of the Little Snake Gorge Thrust, combined with at least one subsidiary thrust within the Hajir Formation, allowed for the reconstruction of the geometry and kinematics of the main tectonic contact, which accommodated a top-to-NE transport.

Both the subsidiary thrust and the underlying mylonitic zone are associated with the F_1 folds affecting the carbonate layers of the Hajir Formation. In particular, the subsidiary thrust appears to cut across the limbs of a large-scale, asymmetric anticlinal fold characterized by a subhorizontal axial plane gently dipping toward the SW. The cross-cutting relationships between the thrust and bedding planes, together with the previously discussed pressure and temperature conditions recorded by the Hajir and Mu'aydin Formations, suggest that active folding played a significant role in accommodating crustal shortening before thrust development at deep crustal levels. As strain progressively localized and cumulated, deformation likely became more ductile, allowing folding to absorb the majority of the shortening. This evolution ultimately produced a stretched fold thrust geometry, wherein the ductile, overturned limb of a growing fold became progressively thinned and elongated until it eventually failed along the thrust surface (e.g., Boyer & Elliott, 1982).

Deformation within the Mu'aydin Formation is primarily accommodated by folding and associated axial planar cleavage sets, except for localized brittle features that offset the more competent layers or that occur within them, such as immature duplex structures; nevertheless, regardless of any possible subsequent refolding, both the latter and earlier F_1 folds within the Mu'aydin Formation have a NE-to-SE-directed vergence, thus suggesting compatibility with the kinematics of the main tectonic contact. In both the Hajir and Mu'aydin Formations, F_1 folds exhibit markedly asymmetric geometries, with thick, short forelimbs and thin, elongated back limbs, consistent with flexural slip/flow folding under ductile deformation conditions. However, flexural slip did not lead to the development of shear zones within the Mu'aydin Formation, likely due to a different lithology and a contrasting rheological response to stress.

Folding is commonly closely associated with the development of metamorphic fabrics. In particular, tectonic contacts along thrust sheets are commonly characterized by folds whose axial planes are parallel to a coeval foliation (e.g., Roda et al., 2021), here formed under blueschist-facies conditions. However, despite the fact that folding and veining affected both formations, the collected data indicate that the Hajir Formation is characterized by more localized and continuous deformation, expressed by a higher number of shear zones, whereas the Mu'aydin Formation displays more pervasive deformation structures throughout the rock volume, particularly within the sandy and silty layers, such as the S_1 and S_2 cleavage sets which, however, were not documented within the hanging wall of the main thrust. This difference is attributed to the contrasting rheology and mechanical competence of the two formations, which responded differently to the imposed deformation.

The generally NE-verging structures within the Hajir and Mu'aydin formations and the Little Snake Gorge Thrust itself are consistent with the S_1 cleavage set, which in the fault core also acted as pathway for circulating metamorphic fluids inducing the precipitation of metamorphic aragonite.

This cleavage, interpreted as the axial planar cleavage associated with F_1 folds, is pervasive throughout the Mu'aydin Formation within the study area, affecting the rock volume to varying degrees of intensity, and is significantly more penetrative within the silty and sandy layers. The schistose fabric that developed under blueschist-facies conditions is usually defined by the parallel alignment of glaucophane, lawsonite, and white mica (e.g., Roda et al., 2021; De Caroli et al., 2024). In contrast, the spaced S_1 cleavage set displays undulating and anastomosing geometries typical of sandy lithologies but remains devoid of the typical index minerals indicative of blueschist-facies conditions.

Fluids exert a fundamental control on both the metamorphic evolution and the deformation behaviour of rocks subjected to blueschist-facies conditions. Microstructural and rheological analyses of natural blueschist shear zones suggest deformation consistent with thin-film pressure-solution creep, where the creep rate is controlled by the presence and continuity of intergranular fluid films (e.g., Schmidt & Platt, 2021). The transformation of oceanic crustal protoliths and associated sedimentary sequences into blueschists requires pervasive hydration, typically through interaction with seawater or fluids derived from the subducting slab, which enables the formation of hydrous mineral assemblages, such as glaucophane and lawsonite. Consequently, the thermodynamic stability of these index minerals is strictly constrained by the presence of H_2O-rich conditions (e.g., Schumacher et al., 2008). However, the preservation of metamorphic aragonite is compromised by the presence of excess fluids, as it rapidly transforms back into calcite when exposed to water at high temperatures (e.g., Blake et al., 1969). Thus, the absence of index minerals within the Mu'aydin Formation, generally characterized by a refractory and chemically depleted lithotype, could be explained by water-deficient conditions in a dry subduction zone, which would have also favoured the preservation of metamorphic aragonite.

Moreover, the geometry and the mineralogy of the veins exploiting the S_1 cleavage provide insights into the stress conditions governing the formation of the documented tensile failures. The vein sets associated with the Little Snake Gorge Thrust are summarized in the figure below (Fig. 40).

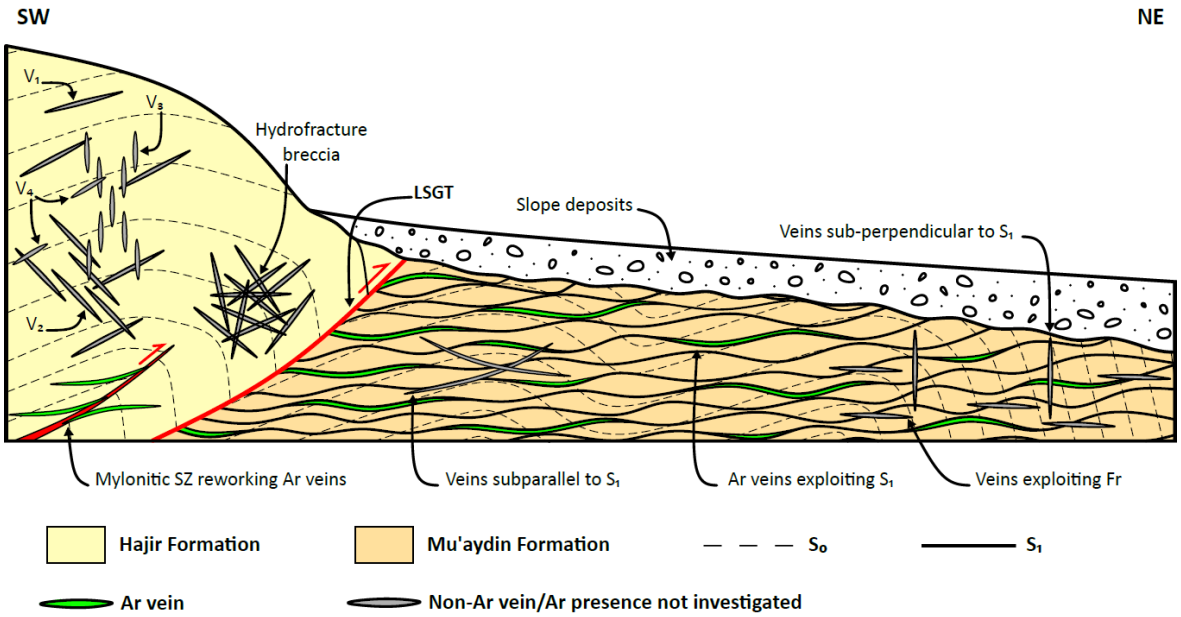

***Figure 11**: Schematic outcrop sketch of the Little Snake Gorge Thrust (LSGT), summarizing vein sets, associated aragonite (Ar) occurrences, and their spatial distribution, not to scale.*

Having preserved aragonite with the typical acicular texture for millions of years, the tensile failures exploiting S_1 must have been subjected to extremely low shear stress values. For this reason, explaining the formation and style of the aragonite veins requires the involvement of purely extensional, Mode I fractures. Tensile fracturing, a fundamental process governing the formation of veins with potential economic significance, can only take place when the Mohr circle becomes tangent to the failure envelope at $\tau = 0$ and $\sigma_3 = T$, with T representing the rock's tensile strength. Due to the geometry of the failure envelope, this condition is only met when the differential stress (σ_1 - σ_3) remains below 4T (Fig. 41) (Cosgrove, 1995; Belayneh & Cosgrove, 2010).

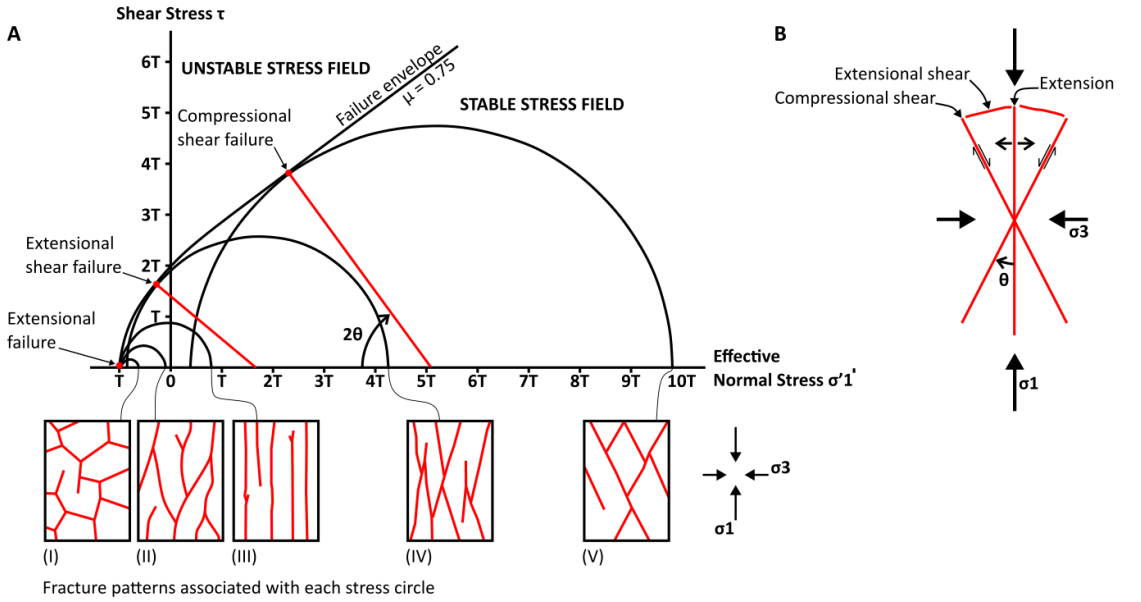

***Figure 41**: **A**, Combined Navier-Coulomb-Griffith failure envelope illustrating various failure modes associated with five distinct stress states: (I)-(III) are characterized by differential stresses below the 4T threshold, resulting in extensional failure, (IV), with a differential stress approximating 4T, produces a transitional or hybrid failure mode, (V), marked by high differential stress, leads to shear failure; **B**, Schematic overview depicting the correlation between failure mechanisms and the corresponding stress regimes (redrawn and modified from Belayneh & Cosgrove, 2010).*

Increasing the pore fluid pressure counteracts lithostatic compression, reducing the total stress to the effective stress, thereby facilitating ductile deformation and enhancing mechanical weakening (Cosgrove, 1995; Schmidt & Platt, 2021). As a result, the Mohr circle shifts leftward by a value equivalent to the fluid pressure. This displacement may bring the circle into contact with the failure envelope at $\tau = 0$ and $\sigma_3 = T$, provided that the differential stress remains below the 4T threshold (Cosgrove, 1995). Fracturing induced by elevated fluid pressure is referred to as hydraulic fracturing, and the resulting deformation style is strongly dependent on the magnitude of the differential stress (Cosgrove, 1995). Hydraulic fracturing does not always result in randomly distributed tensile cracks or chaotic breccias. Instead, its expression varies as a function of the stress regime, ranging from disordered tensile fractures to systematically oriented tensile cracks, and, under higher differential stresses, even to shear fractures (Cosgrove, 1995). The anastomosed geometry of the cleavage set S_1 could be attributed to the stress conditions associated with case (II) in Figure 41, where the differential stress is low but not sufficiently to generate randomly oriented structures. Thus, the spatial distribution and the types of veins documented in the footwall of the main thrust demonstrate that the deformational phases responsible for its formation were characterized by low differential stress. Evidence of chaotic brecciation, ascribable to case (I) in Figure 41 and probably coeval with the formation of the veins exploiting S_1 within the Mu'aydin Formation, has been reported within the Hajir Formation.

A lower differential stress, which is required for the formation of randomly oriented structures, can be explained by the permeability contrast at the interface between the nearly impermeable carbonate layers of the rather isotropic Hajir Formation and the more permeable sandy and silty layers of the greatly anisotropic Mu'aydin Formation, as well as by the subsequent fluid overpressure. Indeed, a pre-existing planar anisotropy within the rock volume exerts a primary control on vein development, acting as planes of mechanical weakness that can be preferentially reactivated or dilated by the prevailing stress regime, thereby facilitating fluid ingress, migration and, possibly, mineralization.

Thus, the pervasive S_1 cleavage set, reported only within the Mu'aydin Formation, has likely influenced the spatial distribution and geometry of the aragonite veins within this formation, with only less frequent occurrences of veins crosscutting the cleavage in orientations consistent with the ambient stress field. Other vein sets, devoid of aragonite, have also been documented within the Mu'aydin Formation. Younger veins exploit sets of NNE-to-NE-verging extensional shear fractures, referred to as "Fr," which are likely ascribable to later extensional deformation phases related to doming processes. In addition, quartz and calcite veins cut across S_1 both sub-parallel and sub-perpendicular to its orientation, supporting the hypothesis by Scharf et al. (2025) of an overprinting related to a late Miocene to Pleistocene hydrothermal event.

Considering the compatibility between the results of this study and those by Zuccari et al. (2023), and in light of the absence of geochronological data supporting a Cadomian or Angudanian age, the aragonite-rich S_1 cleavage set is interpreted in here as Cretaceous in age, coeval with the generally NE-verging structures reported in the study area, the Little Snake Gorge Thrust, and with the blueschist-facies metamorphism. Furthermore, the occurrence of aragonite in both the hanging wall and the footwall of the main thrust suggests that the latter likely acted, during its formation, as a primary pathway under blueschist facies conditions for the transport of the fluids responsible for aragonite precipitation, and that the fault core did not act as a barrier during fluid circulation.

Evidence of refolding is, however, observed at both the outcrop scale, within the Mu'aydin Formation, and at the regional scale, affecting the Little Snake Gorge Thrust itself. Specifically, this evidence has been found in the form of F_2 folds, responsible for the F_1 folds axes rotation and for the verticalization of the bedding and earlier structures, such as intra-layer duplexes. Since the S_2 foliation has been identified exclusively in proximity to the F_2 hinge zones, which were observed in the northernmost part of the study area, and is absent farther from these zones, this foliation set has been interpreted as the axial plane cleavage to these aforementioned folds. Given that even the reactivated contact between the Mu'aydin and the Hajir Formations exhibits clear evidence of later folding, plainly observable from the structure trace on the geological maps of the area, the re-folding event responsible for the F_2 folds must postdate, or at the earliest, be coeval with the Cretaceous thrusting during subduction. However, satellite imagery, previous geological maps, and field evidence have always suggested that only the Precambrian rocks of the Autochthon A appear to be folded.

Considering that lithology and rheology have a major role in the structural evolution of regions, and that rock volumes of different rheological or mechanical properties react differently to imposed stress and strain (e.g., Fossen et al., 2019), the mechanical competence contrast between the Hajir Formation and the Mistal and Mu'aydin Formations may account for the specific localization of folding in this specific area. Buckling takes place when a mechanically competent layer, enclosed within a less competent matrix, undergoes shortening parallel to its principal axis (Nabavi & Fossen, 2021).

Specifically, the massive and competent limestones of the Hajir Formation, enclosed within the highly anisotropic diamictite units of the Mistal Formation and the sandy-silty layers of the Mu'aydin Formation, may represent a prime regional-scale example of single-layer buckling, where the high competence contrast between formations likely allows for effective localization of deformation.

It has been suggested that fold interference patterns should not be taken, by themselves, as evidence of polyphase deformation (e.g., Park, 1969; Fossen et al., 2019). Fossen et al. (2019) recently emphasized the role of progressive deformation, defined as a phase of continuous deformation during which composite structures such as overprinting cleavages, refolded folds, and folds and fabrics, typically with significant variation in style and orientation, may form (Fossen et al., 2019). Furthermore, a temporal framework based exclusively on outcrop-scale geochronological interpretations is no longer sufficient in light of the dating by Zuccari et al. (2023).

Within a subduction zone, stress distribution may be heterogeneous and can be influenced by local boundary conditions, occasionally giving rise to apparent kinematic inconsistencies. Changes in the direction of the stress axes have been documented in seismically active subduction zones. Studies on coseismic and postseismic stress rotations due to large subduction earthquakes demonstrated that stress axes can rotate abruptly in response to seismic events, further modifying the local stress field within the subduction channel (e.g., Hardebeck et al., 2012). Other studies reported depth-dependent rotations of principal stress directions, likely reflecting changes in tectonic forces and fault geometries with depth (e.g., Putri et al., 2025). Such rotation can be linked to complex interactions between plate motions, fault orientations, and mechanical heterogeneities within the subduction channel and the subducting rock packages, causing the stress field to reorient as rocks deform and slip at different depths (Putri et al., 2025). Finally, free subduction zones are defined as settings in which the overriding plate is stationary in the far field and the oceanic subducting plate is freely moving horizontally (e.g., De Franco et al., 2007). In this scenario, even if the stress axes remained constant over time, horizontal displacement or rotation of lithospheric blocks induced, for instance, by the counterclockwise rotation of Arabia, would still lead to the development of interference structures.

The hypothesis of a progressive counterclockwise rotation of the stress field is supported by the vein generations identified within the Hajir Formation. The cross-cutting relationships between vein sets V_1, V_2, and V_3 hint to a systematic rotation pattern in time: V_1 represents early tensile fractures consistent with a maximum principal stress oriented NNE-SSW, followed by V_2, indicative of a NW-SE shortening direction, and culminating in V_3, which records a maximum stress axis oriented WNW-ESE. The V_4 set, likely related to more recent fracturing events, appears to exploit pre-existing weaknesses within the rock volume, possibly reactivating structures initially formed during the V_1 phase. In addition, a progressive rotation of the principal stress axes could also explain why the development of the Little Snake Gorge Thrust has been interrupted, leaving this tectonic contact at an incipient stage.

A schematic representation of a possible tectonic evolution of the Little Snake Gorge Thrust, featuring the progressive rotation of the maximum stress axes, is shown below (Fig. 42A, B, C, D):

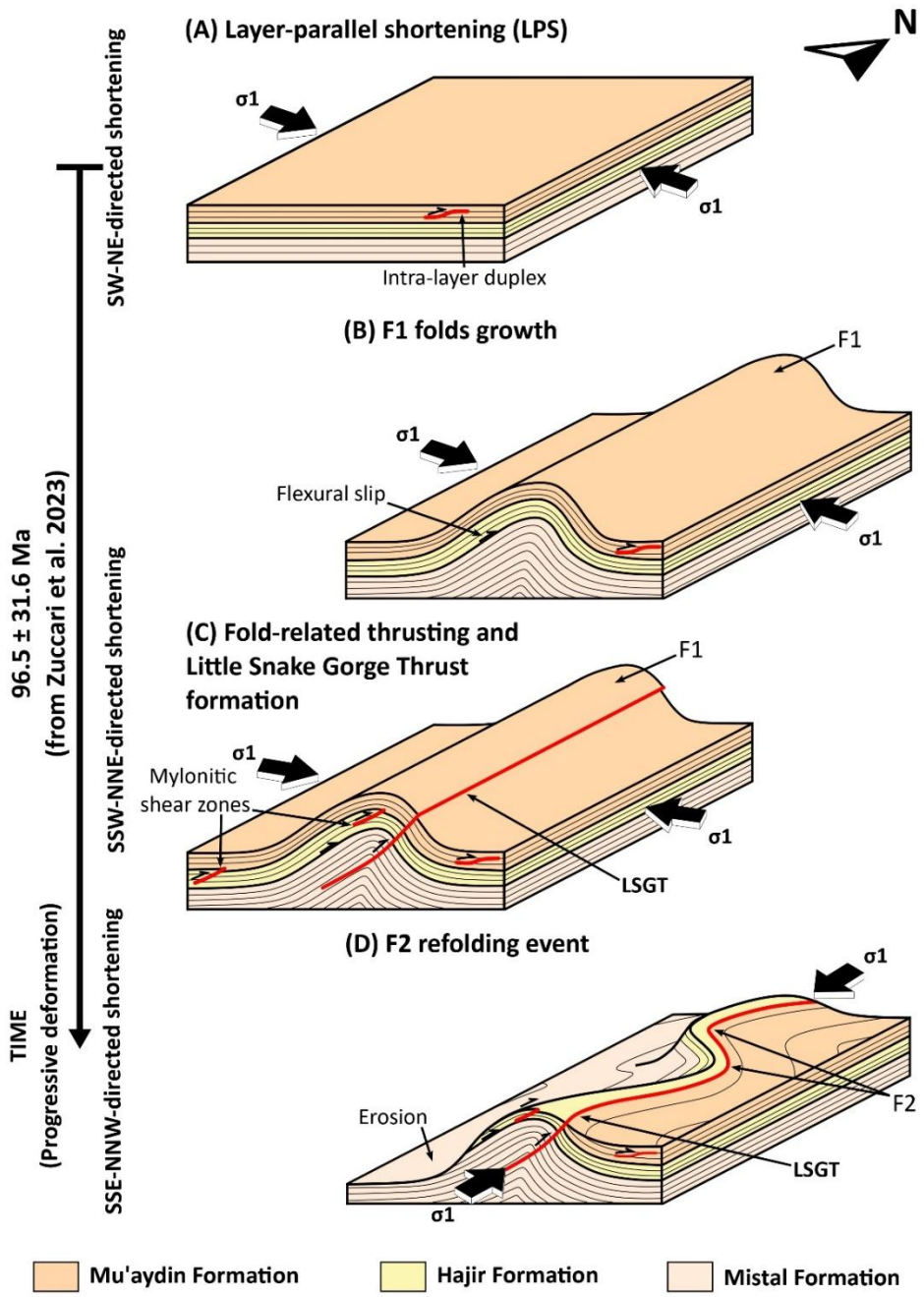

***Figure 42**: Schematic tectonic evolution of the Little Snake Gorge Thrust, not to scale; **A**, Onset of the shortening phase, strain is accommodated by LPS, leading to the formation of structures like intra-layer duplexes; **B**, The prevailing P-T conditions and ductile deformation allow active folding to accommodate most of the strain as it increases, resulting in the formation of F_1 folds and mylonitic shear zones developing at layer interfaces due to flexural slip; **C**, Folding can no longer accommodate all the strain, and thrusting becomes the dominant deformation mechanism, associated with the development of new mylonitic and ultra-mylonitic shear zones and of the LSGT (Little Snake Gorge Thrust); **D**, The rotation of the principal stress axes leads to interference structures, resulting in the refolding of previously formed features, such as the verticalization of intra-layer duplexes, and the formation of F_2 folds (the erosion resulting from doming leads to the present-day geometries).*

Therefore, although a polyphase evolution of the Sahtan Window cannot yet be ruled out, scenarios in which progressive deformation plays a key role in the tectonic evolution of the Little Snake Gorge Thrust should not be excluded. Isotopic dating is ultimately necessary to corroborate or refute these hypotheses, and to shed light on the deformational history of the Sahtan Window and the entire Jabal Akhdar Dome.

4.2 - REGIONAL-SCALE IMPLICATIONS OF BLUESCHISTS FACIES METAMORPHISM

The obtained pressure estimates exceed the lithostatic values due to the weight of the ophiolitic sheet emplaced over the sedimentary cover of the Arabian autochthonous units, considering that the combined thickness of the Semail Ophiolite and Hawasina nappes above the area corresponding to the present day Jabal Akhdar Dome did not exceed 6.5 km (Aldega et al., 2017). If the deformation structures observed within the Mu'aydin Formation at the Little Snake Gorge share the same origin as those dated by Zuccari et al. (2023), this would require their formation to have occurred during a Cretaceous tectonic regime marked by a generally NE-SW-oriented crustal shortening.

This compressional regime can be attributed exclusively to the Late Cretaceous subduction of the Arabian passive margin beneath the Eurasian Plate, corroborating recent studies that report deformation structures within the Permian and post-Permian successions of the Autochthon B in the Jabal Akhdar Dome (Degl'Innocenti, 2024), which could not have been influenced by earlier Cadomian or Angudan orogenic events. The discovery of high-pressure metamorphic conditions within the Precambrian rocks of the Little Snake Gorge, along with the subsequent involvement of the kilometre-thick metasedimentary cover of Jabal Akhdar in the Cretaceous subduction phase, necessitates a reassessment of existing models concerning the subducting slab dynamics, as well as a re-evaluation of the metamorphic evolution that characterizes the tectonic window.

The discussion about both the direction and number of subducting slabs in the region remains open to debate. Based on the data and measurements collected in the present study, the vergence of the observed structures supports the hypothesis of the progressive NE-ward stacking of nappes in the context of accretionary wedge development associated with an early SW-dipping subduction zone, subsequently followed by the northward shift of the active margin and the development of the present-day NE-dipping Makran subduction zone (Fig. 43) (e.g., Gregory et al., 1998; Degl'Innocenti, 2024).

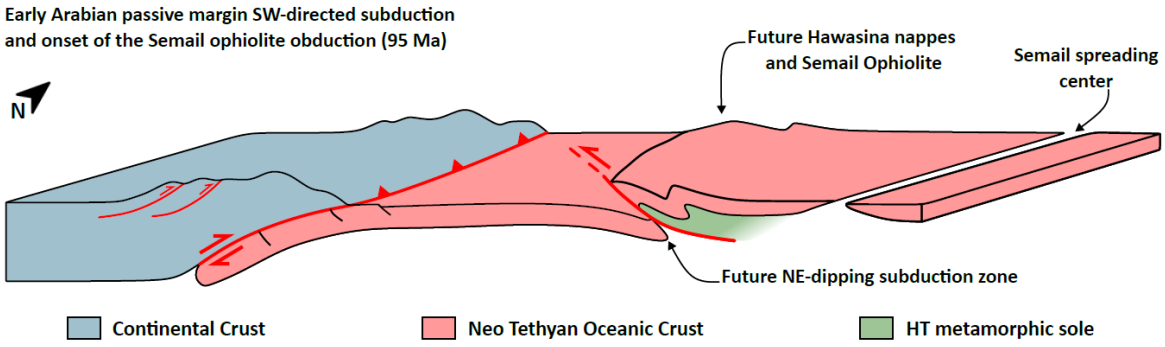

***Figure 43**: Simplified model involving an initial Cretaceous subduction directed towards the SW at the time of the onset of the obduction of the Semail Ophiolite and the Hawasina Nappes which was subsequently replaced by the current subduction directed towards the NE (redrawn and modified after Degl'Innocenti, 2024).*

However, regardless of the adopted model, a significant difference exists between the pressure-temperature conditions recently described in the Jabal Akhdar Dome and those derived from Saih Hatat, the latter having reached eclogite-facies conditions. This discrepancy warrants further considerations.

If an earlier, southwest-directed intra-continental subduction zone is considered, the succession currently exposed in Jabal Akhdar might have been subducted to depths corresponding to blueschist facies conditions. This subduction would have subsequently been aborted due to unfavourable buoyancy conditions. In this perspective, Saih Hatat would represent a later phase of subduction toward the northeast.

Alternatively, if a single northeast-directed subduction is assumed, the contrasting metamorphic conditions of the two domes may be attributed to oblique subduction and their different positions along the margin. In this scenario, Saih Hatat would have been located in a more external position from the outset, farther from Arabia and closer to the trench (Fig. 44A).

In fact, the presence of the Semail Gap, a NNE-SSW-directed tectonic feature that presently separates the two domes, has been proposed as a potential cause of their different subduction histories, by acting as a structural divide. Recent studies on the offshore continuation of the Semail Gap suggest that it represents a major transfer zone, which reactivated an older Pan-African suture in the context of a single NE-dipping subduction system (Ninkabou et al., 2021). Furthermore, they demonstrated that this structure separates two contrasting offshore domains of the Semail Ophiolite, each recording distinct stages of the obduction process (Ninkabou et al., 2021).

This suggests that the Semail Gap may have acted as a transfer zone during the Cretaceous, accommodating differential convergence-related stresses and likely contributing to segmentation of the subducting slab. Therefore, this major tectonic feature could have enabled the Jabal Akhdar and Saih Hatat Domes to reach different depths and experience contrasting metamorphic histories during a NNE-directed subduction phase (Fig. 44A, B).

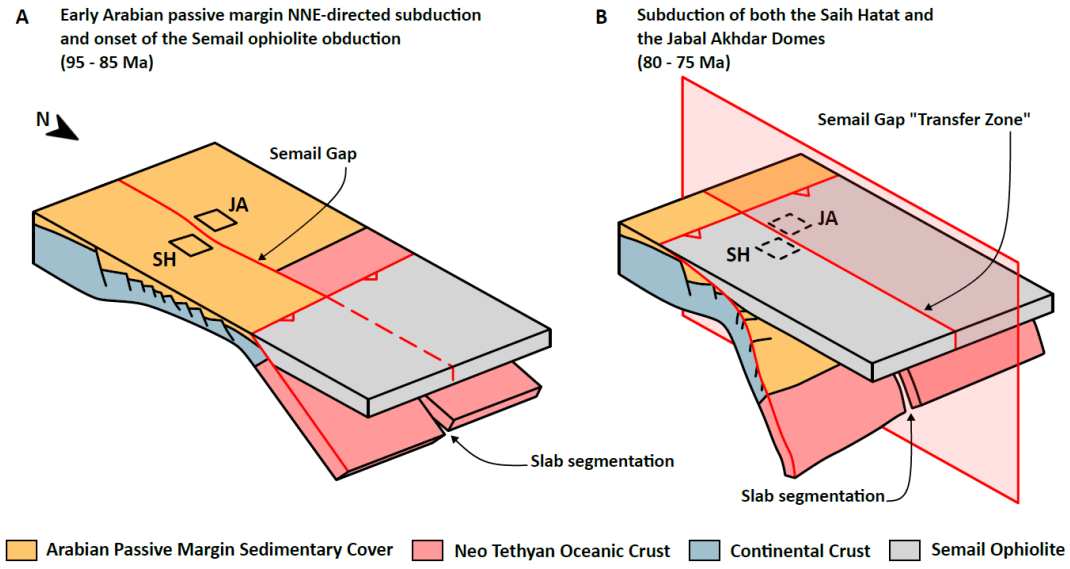

***Figure 44**: Simplified model of the role of the Semail Gap during Lower-Upper Cretaceous subduction; **A**, Early subduction of the Arabian passive margin and initiation of Semail Ophiolite obduction; **B**, the Semail Gap functions as a transfer zone during the subduction of the Jabal Akhdar and Saih Hatat Domes (redrawn and modified after Ninkabou et al., 2021).*

Consequently, although structural field data support a geodynamic scenario involving an initial SW-directed subduction phase, only later followed by the initiation of the present-day NE-dipping subduction, available pressure-temperature constraints are also associated with a model invoking a single NE-dipping subduction zone, with the direct involvement of the Semail Gap as a tectonic transfer zone responsible for imparting contrasting metamorphic evolutions to the two tectonic windows.

The estimated pressure-temperature conditions in the Little Snake Gorge and the increasing metamorphic thermobarometric gradient from the SSW to NNE within the Jabal Akhdar Dome and from SW to NE within the Saih Hatat Dome (Fig. 45) could indeed find an explanation in the geodynamic model proposed by Ninkabou et al. (2023), involving different depths reached by the two proto-tectonic windows as a result of the segmentation of the subducting slab.

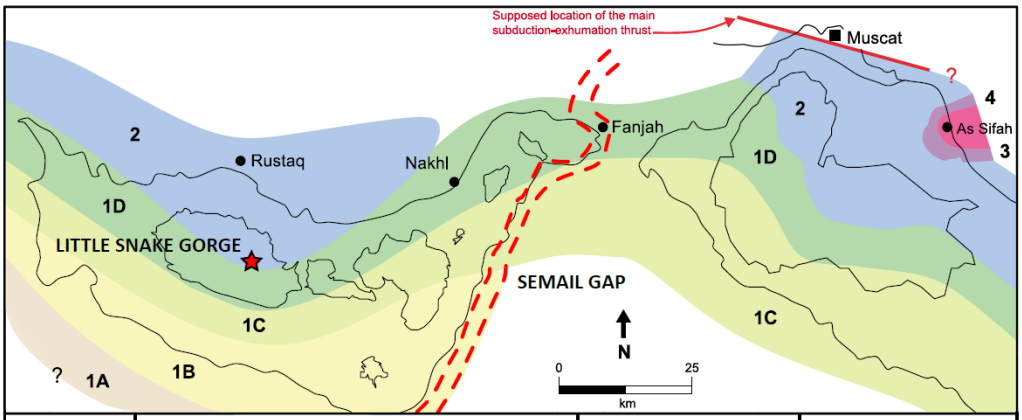

Zone		Metamorphic facies	Pressure	Temperature
EXTERNAL	1A	Upper Anchizone	0.2 - 0.4 GPa	<200°C
	1B			
	1C	Deep Anchizone		
	1D	Greenschist	0.4 - 0.7 GPa	200 - 300°C
INTERNAL	2	Blueschist	0.6 - 1 GPa	250 - 435°C
	3	Glaucophane-Almandine Blueschist	0.6 - 1.5 GPa	380 - 500°C
	4	Glaucophane Eclogite	1.5 - 2 GPa	500 - 580°C

***Figure 45**: Metamorphic gradient map of the Jabal Akhdar and Saih Hatat Domes, based on data from Zuccari et al. (2023) and the present study (redrawn and modified after Breton et al., 2004).*

Consequently, during a NE-directed subduction, the slab segment located west of the Semail Gap would have undergone lower-grade metamorphism compared to the eastern segment, resulting in differences in the metamorphic gradient between the Jabal Akhdar and Saih Hatat Domes. Nonetheless, the lack of SSW-verging structural features, which would be expected in response to such a geodynamic framework, corroborates the hypothesis of an earlier phase of SW-dipping subduction.

In any case, the rocks exposed in the Little Snake Gorge were still subjected to high-grade metamorphism, reaching minimum estimated depths of c. 30 km, thus providing evidence that this tectonic window was likewise involved in the Late Cretaceous subduction of the Arabian passive margin.

CHAPTER 5 - CONCLUSIONS

The primary objective of examining the Little Snake Gorge Thrust in the field was to achieve a detailed structural analysis of the deformation features thereof, combining insights from both microstructural and mesoscale observations. This study aimed to integrate structural and metamorphic information into a comprehensive interpretive model to clarify the pressure-temperature-deformation conditions that facilitated the tectonic placement of the Hajir Formation above the Mu'aydin Formation through thrusting. Additionally, attention focused on understanding the genesis and spatial arrangement of aragonite-bearing vein systems along foliation planes formed at synkinematic high-pressure metamorphic conditions. RSCM analyses have been used to reconstruct the metamorphic conditions associated with the syn-thrusting deformation of the Mu'aydin Formation in the footwall of the Little Snake Gorge Thrust. There, temperature and pressure conditions of c. 348 ± 50 °C and 0.85 ± 0.12 GPa, respectively, have been recorded. Therefore, blueschists facies metamorphic conditions have been constrained also in the Mu'aydin Formation within the Jabal Akhdar Dome. Structural data integrated with P-T conditions and with recent isotopic dating by Zuccari et al. (2023) suggest a HP-LT metamorphic imprint within both the footwall and the hanging wall of the Little Snake Gorge Thrust, associated with the Cretaceous subduction of the Arabian continental passive margin, where the metasedimentary succession was subducted to minimum depths of c. 30 km, reaching blueschists facies conditions. The involvement in this tectonic phase would also explain the origin of the deformation structures recently identified by Degl'Innocenti (2024) in the Permian and post-Permian rocks of Autochthon B within the tectonic window.

Field investigations and structural analyses of deformation features ranging from brittle to ductile were performed to reconstruct the tectonic evolution of the Little Snake Gorge Thrust, the key aspects of which are summarised below:

- During the Late Cretaceous subduction, shortening initiated an early phase of LPS, resulting in the formation of incipient structures such as layer-parallel duplexes.

- Subsequently, active folding under ductile conditions began to accommodate strain, giving rise to NE-verging asymmetric F_1 folds by flexural flow and slip and characterized by the subhorizontal axial planar cleavage S_1.

- Once folding could no longer accommodate shortening-related deformation, discrete thrusting started to localize deformation leading to the development of the Little Snake Gorge Thrust. This was accompanied by a suite of NE-verging structures such as mylonitic shear zones within the more competent Hajir Formation. The main thrust acted as the primary pathway for fluid circulation responsible for the formation of aragonite-bearing veins, which exploited the pre-existing S_1 cleavage planes.

- Field results also show that the Hajir and Mu'aydin Formations in the Sahtan Window underwent a second folding event that generated complex interference structures, associated with F_2 folds and with the axial planar cleavage S_2.

Despite previous outcrop-scale geochronological interpretations, the lack of isotopic dating does not allow for the definition of a distinct second deformational phase. Therefore, these interference structures are attributed to progressive deformation linked to changes in the stress field orientation within the subduction channel, which likely appear to have arrested the development of the main thrust at an incipient stage and may have affected both Autochthon A and B within the tectonic window.

The evidence of cyclic brittle-ductile deformation, along with the estimates of HP metamorphism in the Precambrian rocks of both the hanging wall and the footwall of the Little Snake Gorge Thrust calls for a revision of current interpretations regarding the dynamics of the Arabian subducting plate, as well as a re-evaluation of the metamorphic gradient recorded in the exposed rocks of the Jabal Akhdar Dome.

The data collected from the field are compatible with the tectonic scenario proposed by Degl'Innocenti (2024), involving an Upper Cretaceous, generally NE-verging orogenic prism developing above an initial SW-dipping subduction zone along the northeastern Arabian passive margin, prior the onset of the present-day NE-directed subduction. However, the difference in metamorphic imprint between the Jabal Akhdar and the Saih Hatat Domes, with the latter reaching eclogite facies conditions, supports the hypothesis by Ninkabou et al. (2021) of a single NNE-directed subduction zone associated with the active role of the Semail Gap, which may have acted as a transfer zone during the Cretaceous by accommodating variations in convergence-related stress and contributing to the segmentation of the subducting slab, exposing the two tectonic windows to distinct pressure-temperature regimes.

Nevertheless, the rocks outcropping in the Little Snake Gorge experienced high-grade metamorphism, reaching minimum estimated depths of c. 30 km, thus providing evidence that the Jabal Akhdar Dome was involved in the Late Cretaceous subduction of the Arabian passive margin as well.

In conclusion, reconstructing the tectonic and structural evolution of the Autochthon A may greatly benefit from constraints and data from the Little Snake Gorge section, which has proven essential for understanding the development of the Jabal Akhdar Dome and for advancing knowledge of deformation processes under blueschist-facies conditions, fluid circulation, and the precipitation of minerals that, while not economically relevant here, may hold economic significance elsewhere.

An extensive examination of all exposed sections and structures in the Jabal Akhdar Dome and a detailed assessment of how metamorphic grade and gradients vary spatially within the latter is crucial to ultimately constrain the number and orientation of the slabs involved in this subduction phase, and to define more accurate metamorphic gradient maps. Furthermore, dedicated studies aimed at investigating the role of the Semail Gap during the Cretaceous subduction of the Arabian passive margin are essential to better understand the reasons behind the different evolutionary paths of the two tectonic windows. Geophysical investigations, including seismic tomography and gravity surveys, may serve as valuable complementary tools to support these efforts by providing additional subsurface constraints.

Finally, implementing isotopic dating on minerals that are syn-kinematic with specific deformation phases is essential to precisely constrain the timing of the principal tectonic phases that affected the Jabal Akhdar Dome, including testing whether the compressive events responsible for the refolding of Precambrian rocks within the Sahtan Window indeed occurred during the Cretaceous.

BIBLIOGRAPHY

Abbo A., Avigad D., Gerdes A., 2018. *The lower crust of the Northern broken edge of Gondwana: Evidence for sediment subduction and syn-Variscan anorogenic imprint from zircon U-Pb-Hf in granulite xenoliths*. Gondwana Research 64: 84-96.

Agard P., Searle M. P., Alsop G. I., Dubacq B., 2010. *Crustal stacking and expulsion tectonics during continental subduction: P-T deformation constraints from Oman*. Tectonics 29 (5): 19 pages.

Agard P., Yamato P., Jolivet L., Burov E., 2009. *Exhumation of oceanic blueschists and eclogites in subduction zones: Timing and mechanisms*. Earth-Science Reviews 92 (1-2): 53-79.

Al-Husseini M. I., 2014. *Proposed correlation of Oman's Abu Mahara Supergroup and Saudi Arabia's Jibalah Group*. GeoArabia 19 (2): 17–48.

Allen P. A., 2007. *The Huqf Supergroup of Oman: Basin development and context for Neoproterozoic glaciation*. Earth-Science Reviews 84 (3-4): 139-185.

Allen P. A., Leather J., 2006. *Post-Marinoan marine siliciclastic sedimentation: The Masirah Bay Formation, Neoproterozoic Huqf Supergroup of Oman*. Precambrian Research 144 (3-4): 167-198.

Allen P. A., Leather J., Brasier M. D., 2004. *The Neoproterozoic Fiq glaciation and its aftermath, Huqf supergroup of Oman*. Basin Research 16: 507-534.

Allen P. A., Leather J., Brasier M. D., Rieu R., Mccarron M., Le Guerroué E., Etienne J. L., Cozzi A., 2011. *The Abu Mahara Group (Ghubrah and Fiq formations), Jabal Akhdar, Oman*. In: Arnaud E., Halverson G. P., Shields-Zhou G. (Eds), *The Geological Record of Neoproterozoic Glaciations*, Geological Society, London, U. K., Memoirs, 36: 251-262.

Aoya M., Kouketsu Y., Endo S., Shimizu H., Mizukami T., Nakamura D., Wallis S., 2010. *Extending the applicability of the Raman carbonaceous-material geothermometer using data from contact metamorphic rocks*. Journal of Metamorphic Geology 28 (9): 895-914.

Augustin N., Devey C. W., van der Zwan F. M., Feldens P., Tominaga M., Bantan R. A., Kwasnitschka T., 2014. *The rifting to spreading transition in the Red Sea*, Earth and Planetary Science Letters 395: 217-230.

Baud A., Beauchamp B., Henderson C. M., Richoz S., 2010. *The Permian-Triassic transition on the Saiq Plateau*. In: Baud A. & Bernecker M. (Eds), *IGCP 572 Field Guide Book 2: The Permian-Triassic transition in the Oman Mountains*, GUtech, Muscat, Oman, 34-47.

Behr W. M., Burgmann R., 2021. *What's down there? The structures, materials and environment of deep-seated slow slip and tremor*. Philosophical Transactions of the Royal Society A 379: 44 pages.

Belayneh M., Cosgrove J. W., 2010. *Hybrid veins from the southern margin of the Bristol Channel Basin, UK*. Journal of Structural Geology 32 (2): 192-201.

Beurrier M., Bechennec F., Rabu D., Hutin G., 1986. *Geological Map of Rustaq - Sheet NF 40-3D - Scale 1.100.000 - Explanatory Notes*. Directorate General of Minerals, Sultanate of Oman Ministry of Petroleum and Minerals.

Beyssac O., Goffe B., Chopin C., Rouzaud J. N., 2002. *Raman spectra of carbonaceous material in metasediments: a new geothermometer*. Journal of Metamorphic Geology 20 (9): 859-871.

Blake M., Irwin W., Coleman R., 1969. *Blueschist-facies metamorphism related to regional thrust faulting*. Tectonophysics 8 (3): 237-246.

Boudier F., Nicolas A., 2018. *Synchronous Seafloor Spreading and Subduction at the Paleo-Convergent Margin of Semail and Arabia*. Tectonics, 37 (9): 2961-2982.

Bowring S. A., Grotzinger J. P., Condon D. J., Ramezani J., Newall M. J., Allen P. A., 2007. *Geochronologic constraints on the chronostratigraphic framework of the Neoproterozoic Huqf Supergroup, Sultanate of Oman*. American Journal of Science 307: 1097-1145.

Boyer S. E., Elliott D., 1982. *Thrust Systems*. American Association of Petroleum Geologists Bulletin 66: 1196-1230.

Brasier M., McCarron G., Tucker R., Leather J., Allen P., Shields G., 2000. *New U-Pb zircon dates for the Neoproterozoic Ghubrah glaciation and for the top of the Huqf Supergroup, Oman*. Geology 28 (2): 175-178.

Breton J., Béchennec F., Le Métour J., Moen-Maurel L., Razin R., 2004. *Eoalpine (Cretaceous) evolution of the Oman Tethyan continental margin: insights from a structural Field study in Jabal Akhdar (Oman Mountains).* GeoArabia 9 (2): 41-58.

Callegari I., Scharf A., Mattern F., Bauer W., Pinto A. J., Rarivoarison H., Scharf K., Al Kindi., 2020. *Gondwana accretion tectonics and implications for the geodynamic evolution of eastern Arabia: First structural evidence of the existence of the Cadomian Orogen in Oman (Jabal Akhdar Dome, Central Oman Mountains)*. Journal of Asian Earth Sciences 187: 12 pages.

Carlson W. D., 1980. *The calcite-aragonite equilibrium: effects of Sr substitution and anion orientational disorder*. American Mineralogist 65 (11-12): 1252-1262.

Carminati E., Aldega L., Smeraglia L., Scahrf A., Mattern F., Albert R., Gerdes A., 2020. *Tectonic Evolution of the Northern Oman Mountains,Part of the Strait of Hormuz Syntaxis: New Structuraland Paleothermal Analyses and U-Pb Datingof Synkinematic Calcite*. Tectonics 39 (4): 25 pages.

Carteret C., De La Pierre M., Dossot M., Pascale F., Erba A., Dovesi R., 2013. *The vibrational spectrum of $CaCO_3$ aragonite: A combined experimental and quantum-mechanical investigation*. The Journal of Chemical Physics 138 (1): 13 pages.

Chakrabarty D., Mahapatra S., 1999. Aragonite crystals with unconventional morphologies. Journal of Materials Chemistry 9: 2953-2957.

Clark S. P., 1957. *A Note on Calcite-Aragonite Equilibrium*. American Mineralogist 42 (7-8): 564-566.

Cosgrove J. W., 1995. *The expression of hydraulic fracturing in rocks and sediments*. Geological Society, London, Special Publications 92: 187-196.

Cozzi A., Al-Siyabi H. A., 2004. *Sedimentology and play potential of the late Neoproterozoic Buah Carbonates of Oman*. GeoArabia 9: 11-36.

Cozzi A., Grotzinger J.P., Allen P. M., 2004. *Evolution of a terminal Neoproterozoic carbonate ramp system (Buah Formation, Sultanate of Oman): effects of basement paleotopography*. Geological Society of America Bulletin 116: 1367-1384.

De Caroli S., Fagereng Å., Ujiie K., Blenkinsop T., Meneghini F., Muir D., 2024. *Deformation microstructures of low- and high-strain epidote-blueschist (Ryukyu arc, Japan): Implications for subduction interface rheology*. Journal of Structural Geology 180: 14 pages.

De Franco R., Govers R., Wortel R., 2007. *Numerical comparison of different convergent plate contacts: Subduction channel and subduction fault*. Geophysical Journal International 171 (1): 435-450.

Degl'Innocenti S., 2024. *Architecture and metamorphic imprint of an orogenic wedge and its development during ophiolite obduction: insights from the Jabal Akhdar Dome, Oman*. MSc Thesis, Dipartimento di Scienze Biologiche, Geologiche e Ambientali, Alma Mater Studiorum - Università di Bologna, Bologna, 77 p.

Deif A., 2018. *Seismic Liquefaction Potential in Muscat, Sultanate of Oman*. Journal of Earth Science & Climatic Change 9 (2): 13 pages.

El-Shazly A. E. D., Coleman R. G., Liou J. G., 1990. *Eclogites and blueschists from Northeastern Oman: petrology and P-T evolution*. Journal of Petrology 31 (3): 629-666.

Fossen H., Cavalcante G. C. G., Pinheiro R. V. L., Archanjo C. J., 2019. *Deformation – Progressive or multiphase?*. Journal of Structural Geology 125: 82-99.

Fournier M., Chamot-Rooke N., Petit C., Huchon P., Al-Kathiri A., Audin L., Beslier M., d'Acremont E., Fabbri O., Fleury J., Khanbari K., Lepvrier C., Leroy S., Maillot B., Merkouriev S., 2010. *Arabia-Somalia plate kinematics, evolution of the Aden-Owen-Carlsberg triple junction, and opening of the Gulf of Aden*. Journal of Geophysics Research - Solid Earth 115 (B4): 24 pages.

Glennie K. W., Boeuf M. G. A., Hughes Clarke M. W., Moody-Stuart M., Pilaar W. F. H., Reinhardt B., M., 1973. *Late Cretaceous Nappes in Oman Mountains and Their Geologic Evolution*. AAPG Bulletin 57 (1): 5-27.

Goffé B., Velde B., 1984. *Contrasted metamorphic evolutions in thrusted cover units of the Briançonnais zone (French Alps): A model for the conservation of HP-LT metamorphic mineral assemblages*. Earth and Planetary Science Letters 68 (2): 351-360.

Gomez-Rivas E., Bons P. D., Koehn D., Urai J. L., Arndt M., Virgo S., Laurich B., Zeeb C., Stark L., Blum P., 2014. *The Jabal Akhdar Dome in the Oman Mountains: evolution of a dynamic fracture system*. American Journal of Science 314 (7): 1104-1139.

Goscombe B., Foster D. A., Gray D., Kelsey D., Wade B., 2020. *Metamorphic response within different subduction–obduction settings preserved on the NE Arabian margin*. Gondwana Research 83, 298-371.

Gregory R. T., Gray D. R., Miller J. M., 1998. *Tectonics of the Arabian margin associated with the formation and exhumation of high-pressure rocks, Sultanate of Oman*. Tectonics 17 (5): 657-670.

Gray D. R., Gregory R. T., 2000. *Implications of the structure of the Wadi Tayin metamorphic sole, the Ibra-Dasir block of the Samail ophiolite, and the Saih Hatat window for late stage extensional ophiolite emplacement, Oman*. Marine Geophysical Researches 21: 211-227.

Grobe A., Virgo S., von Hagke C., Urai J. L., Littke R., 2018. *Multiphase structural evolution of a continental margin during obduction orogeny: Insights from the Jebel Akhdar Dome, Oman Mountains*. Tectonics 37: 888-913.

Guilmette C., Smit M. A., Van Hinsbergen D. J., Gürer D., Corfu F., Charette B., Maffione M., Rabeau O., Savard D., 2018. *Forced subduction initiation recorded in the sole and crust of the Semail Ophiolite of Oman*. Nature Geoscience 11 (9): 688-695.

Hacker B. R., Rubie D. C., Kirby S. H., Bohlen S. R., 2005. *The calcite → aragonite transformation in low-Mg marble: Equilibrium relations, transformation mechanisms, and rates*. Journal of Geophysical Research: Solid Earth 110 (B3): 16 pages.

Hanna S. S., 1990. *The Alpine deformation of the Central Oman Mountains.* Geological Society, London, Special Publications 49: 341-359.

Hansman R. J., Ring U., Thomson S. N., Stübner K., 2017. *Late Eocene Uplift of the Al Hajar Mountains, Oman, Supported by Stratigraphy and Low-Temperature Thermochronology*. Tectonics 36 (12): 3081-3109.

Hardebeck J. L., 2012. *Coseismic and postseismic stress rotations due to great subduction zone earthquakes*. Geophysical Research Letters 39 (21): 6 pages.

Henry D. G., Jarvis I., Gillmore G., Stephenson M., 2019. *Raman spectroscopy as a tool to determine the thermal maturity of organic matter: Application to sedimentary, metamorphic and structural geology*. Earth-Science Reviews 198: 19 pages.

Johannes W., Puhan D., 1971. *The calcite-aragonite transition, reinvestigated*. Contributions to Mineralogy and Petrology 31: 28-38.

Koehrer B., Aigner T., Forke H., Pöppelreiter M., 2012. *Middle to Upper Khuff (Sequences KS1 to KS4) outcrop-equivalents in the Oman Mountains:Grainstone architecture on a subregional scale*. GeoArabia 17 (4): 59-104.

Konert G., Al-Hajri S. A., Al Naim A. A., Afifi A. M., de Groot K., Droste H. J., 2001. *Paleozoic Stratigraphy and Hydrocarbon Habitat of the Arabian Plate*. In: Downey M. W., Threet J. C., Morgan W. A. (Eds), *Petroleum Provinces of the Twenty-first Century*. AAPG - The American Association of Petroleum Geologists, Tulsa, Oklahoma, U.S.A.: 483-517.

Kopp C., Fruehn J., Flueh E. R., Reichert C., Kukowski N., Bialas J., Klaeschen D., 2000. *Structure of the Makran subduction zone from wide-angle and reflection seismic data*. Tectonophysics 329 (1–4): 171-191.

Kouketsu Y., Mizukami T., Mori H., Endo S., Aoya M., Hara H., Nakamura D., Wallis S., 2014. *A new approach to develop the Raman carbonaceous material geothermometer for low-grade metamorphism using peak width*. Island Arc 23: 33-50.

Lachize M., Lorand J., Juteau T., 1996. *Calc-alkaline differentiation trend in the plutonic sequence of the Wadi Haymiliyah section, Haylayn massif, Semail ophiolite, Oman*. Lithos 38 (3-4): 207-232.

Lahfid A., Beyssac O., Deville E., Negro F., Chopin C., Goffé B., 2010. *Evolution of the Raman spectrum of carbonaceous material in low-grade metasediments of the Glarus Alps (Switzerland)*. Terra Nova 22 (5): 354-360.

Leather J., Allen P. A., Brasier M. D., Cozzi A., 2002. *Neoproterozoic snowball Earth under scrutiny: Evidence from the Fiq glaciation of Oman*. Geology 30 (10): 891-894.

Le Guerroué E., Allen P., Cozzi A., 2005. *Two distinct glacial succession in the Neoproterozioc of Oman*. GeoArabia 10 (2): 17-34.

Le Guerroué E., Allen P. A., Cozzi A., 2006. *Chemostratigraphic and sedimentological framework of the largest negative carbon isotopic excursion in Earth history: The Neoproterozoic Shuram Formation (Nafun Group, Oman)*. Precambrian Research 146 (1-2): 68-92.

Le Guerroué E., Rieu R., Cozzi A., 2009. *Comment on "Geochronologic Constraints on the Chronostratigraphic Framework of the Neoproterozoic Huqf Supergroup, Sultanate of Oman" by Samuel A. Bowring, John P. Grotzinger, Daniel J. Condon, Jahandar Ramezani, Mark J. Newall and Philip A. Allen, American Journal of Science, v. 307, p. 1097-1145.* American Journal of Science 309: 85-90.

Le Métour J., Rabu D., Tegyey M., Béchennec F., Beurrier M., Villey M., 1990. *Subduction and obduction: two stages in the Eo-Alpine tectonometamorphic evolution of the Oman Mountains*. Geological Society, London, Special Publications 49: 327-339

Lin S., Huang W., 2004. *Polycrystalline calcite to aragonite transformation kinetics: experiments in synthetic systems*. Contributions to Mineralogy and Petrology 147: 604-614.

Loosveld R. J. H., Bell A., Terken J. J. M., 1996. *The Tectonic Evolution of Interior Oman*. GeoArabia 1 (1): 28-51.

Madon M., Gillet P., 1984. *A theoretical approach to the kinetics of calcite ⇌ aragonite transition: application to laboratory experiments*. Earth and Planetary Science Letters 67 (3): 400-414.

Manighetti I., Mercier A., Barros L. D., 2021. *Fault Trace Corrugation and Segmentation as a Measure of Fault Structural Maturity*. Geophysical Research Letters 48 (20): 11 pages.

Mann A., Hanna S. S., 1990. *The tectonic evolution of pre-Permian rocks, Central and Southeastern Oman Mountains.* Geological Society, London, Special Publications 49: 307-325.

Mattern F., Scharf A., 2019. *Transition from the Hajir Formation to the Muaydin Formation*: *a facies change coinciding with extensional, syndepositional faulting (Ediacaran, Jabal Akhdar, Central Oman Mountains)*. Journal of African Earth Sciences 152: 237-244.

Miller J. M., Gray D. R., Gregory R. T., 1998. *Exhumation of high-pressure rocks in northeastern Oman*. Geology 26 (3): 235-238.

Molinaro M., Leturmy P., Guezou C., Eshraghi S. A., 2005. *The structure and kinematics of the southeastern Zagros fold-thrust belt, Iran: From thin-skinned to thick-skinned tectonics*. Tectonics 24 (3): 19 pages.

Molli G., Menegon L., Malasoma A., 2017. Switching deformation mode and mechanisms during subduction of continental crust: a case study from Alpine Corsica. Solid Earth 8: 767-788.

Motaghi K., Shabanian E., Nozad-Khalil T., 2020. *Deep structure of the western coast of the Makran subduction zone, SE Iran*. Tectonophysics 776: 11 pages.

Mount V. S., Crawford R. I. S., Bergman S. C., 1998. *Regional Structural Style of the Central and Southern Oman Mountains: Jebel Akhdar, Saih Hatat, and the Northern Ghaba Basin*. GeoArabia 3 (4): 475-490.

Mouthereau F., Lacombe O., Vergés J., 2012. *Building the Zagros collisional orogen: Timing, strain distribution and the dynamics of Arabia/Eurasia plate convergence*. Tectonophysics 532-535: 27-60.

Muñoz-Montecinos J., Angiboust S., Garcia-Casco A., 2021. *Blueschist-facies paleo-earthquakes in a serpentinite channel (Zagros suture, Iran) enlighten seismogenesis in Mariana-type subduction margins*. Earth and Planetary Science Letters 573: 14 pages.

Nabavi S. T., Fossen H., 2021. *Fold geometry and folding - a review*. Earth-Science Reviews 222: 62 pages.

Ninkabou D., Agard P., Nielsen C., Smit J., Gorini C., Rodriguez M., Haq B., Chamot-Rooke N., Weidle C., Ducassou C., 2021. *Structure of the Offshore Obducted Oman Margin: Emplacement of Semail Ophiolite and Role of Tectonic Inheritance*. Journal of Geophysical Research: Solid Earth 126 (2): 28 pages.

Ozcan E., Piazolo S., Mueller T., 2019. *Tectonometamorphic evolution of the Elekdag metaophiolite, Turkey: A petrographic and geochemical study*. MSc Thesis, School of Earth and Environment, University of Leeds, Leeds, 124 p.

Park R., 1969. *Structural correlation in metamorphic belts*. Tectonophysics 7 (4): 323-338.

Parker J. E., Thompson S. P., Lennie A. R., Pottera J., Tang C. C., 2010. *A study of the aragonite-calcite transformation using Raman spectroscopy, synchrotron powder diffraction and scanning electron microscopy*. CrystEngComm 12 (5): 1590-1599.

Pilia S., Ali M. Y., Searle M. P., Watts A. B., Lü C., Thompson D. A., 2021. *Crustal Structure of the UAE-Oman Mountain Range and Arabian Rifted Passive Margin: New Constraints From Active and Passive Seismic Methods*. Journal of Geophysical Research - Solid Earth 126 (4): 17 pages.

Putri N. R., Wulan A. N., Zahra R., Rohman A. N., 2025. *Variation of Principal Stress Direction with Depth in North Sumatra, Indonesia*. Earth and Environmental Sciences 1458: 12 pages.

Rabu D., Bechennec F., Beurrier M., Hutin G., 1986. *Geological Map of Nakhl - Sheet NF 40-3E - Scale 1.100.000 - Explanatory Notes*. Directorate General of Minerals, Sultanate of Oman Ministry of Petroleum and Minerals.

Ring U., Glodny J., Scharf A., Hansman R., 2023. *Some Like It Cold: The "Conundrum of Samail" Revisited*. Tectonics 42 (1): 15 pages.

Rioux M., Garber J. M., Searle M., Kelemen P., Miyashita S., Adachi Y., Bowring S., 2021. *High-Precision U-Pb Zircon Dating of Late Magmatism in the Samail Ophiolite: A Record of Subduction Initiation*. Journal of Geophysical Research - Solid Earth 126 (5): 26 pages.

Robertson A. H. F., 1987. *The transition from a passive margin to an Upper Cretaceous foreland basin related to ophiolite emplacement in the Oman Mountains*. GSA Bulletin 99 (5): 633-653.

Robertson A. H. F., Searle M. P., 1990. *The northern Oman Tethyan continental margin: stratigraphy, structure, concepts and controversies*. Geological Society, London, Special Publications 49: 3-25.

Roda M., Zucali M., Corti L., Visalli R., Ortolano G., Spalla M. I., 2021. *Blueschist mylonitic zones accommodating syn-subduction exhumation of deeply buried continental crust: The example of the Rocca Canavese Thrust Sheets Unit (Sesia-Lanzo Zone, Italian Western Alps)*. Swiss Journal of Geosciences 114 (1): 1-33.

Rossetti F., Nozaem R., Lucci F., Vignaroli G., Gerdes A., Nasrabadi M., Theye T., 2015. *Tectonic setting and geochronology of the Cadomian (Ediacaran-Cambrian) magmatism in Central Iran, Kuh-e-Sarhangi region (NW Lut Block)*. Journal of Asian Earth Sciences 102: 24-44.

Rostron P., Gaber S., Gaber D., 2016. *Raman Spectroscopy, Review*. International Journal of Engineering and Technical Research (IJETR) 6 (1): 50-64.

Ruban D. A., Al-Husseini M. I., Iwasaki Y., 2007. *Review of Middle East Paleozoic plate tectonics*. GeoArabia 12 (3): 35-56.

Rubatto D., Regis D., Hermann J., Boston K., Engi M., Beltrando M., McAlpine S. R., 2011. *Yo-yo subduction recorded by accessory minerals in the Italian Western Alps*. Nature Geoscience 4 (5): 338-342.

Scharf A., Bolhar R., Uysal T., Mattern F., Callegari I., Bozkaya G., Baublys K., 2025. *A vein-hosted carbonate: Record of late miocene to pleistocene hydrothermal activity in the Hajar Mountains (Jabal Akhdar Dome, Sultanate of Oman)*. Lithos.

Scharf A., Mattern F., Al-Wardi M., Frijia G., Moraetis D., Pracejus B., Bauer W., Callegari I., 2021. *The Geology and Tectonics of the Jabal Akhdar and Saih Hatat Domes, Oman Mountains*. Geological Society, London, U. K., Memoirs, 54, 125 p.

Scharf A., Mattern F., Moraetis D., Callegari I., Weidle C., 2019. *Postobductional kinematic evolution and geomorphology of a major regional structure-The Semail Gap Fault Zone (Oman Mountains).* Tectonics 38: 2756-2778.

Schmidt W. L., Platt J. P., 2021. *Stress, microstructure, and deformation mechanisms during subduction underplating at the depth of tremor and slow slip, Franciscan Complex, northern California*. Journal of Structural Geology 154: 28 pages.

Schumacher J. C., Brady J. B., Cheney J. T., Tonnsen R. R., 2008. *Glaucophane-bearing Marbles on Syros, Greece*. Journal of Petrology 49 (9): 1667-1686.

Searle M. P., 1985. *Sequence of thrusting and origin of culminations in the northern and central Oman Mountains*. Journal of Structural Geology 7 (2): 129-143.

Searle M. P., 2007. *Structural geometry, style and timing of deformation in the Hawasina Window, Al Jabal al Akhdar and Saih Hatat culminations, Oman Mountains.* GeoArabia 12 (2): 99-130.

Searle M. P., Cox J., 2002. *Subduction zone metamorphism during formation and emplacement of the Semail ophiolite in the Oman Mountains*. Geological Magazine 139 (3): 241-255.

Searle M. P., Waters D. J., Martin H. N., Rex D. C., 1994. *Structure and metamorphism of blueschist-eclogite facies rocks from the northeastern Oman Mountains*. Journal of the Geological Society 151 (3): 555-576.

Smith E., Dent G., 2019. *Modern Raman Spectroscopy - A Practical Approach, Second Edition*. John Wiley & Sons Ltd, Chichester, U. K., 225 p.

Stampfli G. M., Borel G. D., 2002. *A plate tectonic model for the Paleozoic and Mesozoic constrained by dynamic plate boundaries and restored synthetic oceanic isochrons*. Earth and Planetary Science Letters 196 (1-2): 17-33.

Stern B., Johnson P., 2008. *Do variations in Arabian plate lithospheric structure control deformation in the Arabian-Eurasian convergence zone?*. IOP Conference Series: Earth and Environmental Science 2 (1): 1-7.

Stern R. J., Avigad D., Miller N. R., Beyth M., 2006. *Evidence for the Snowball Earth hypothesis in the Arabian-Nubian Shield and the East African Orogen*. Journal of African Earth Sciences 44 (1): 1-20

Tavani S., Corradetti A., Sabbatino M., Seers T., Mazzoli S., 2020. *Geological record of the transition from induced to self-sustained subduction in the Oman Mountains.* Journal of Geodynamics 133: 8 pages.

Van Hinsbergen D. J., Edwards M. A., Govers R., 2009. *Geodynamics of collision and collapse at the Africa-Arabia-Eurasia subduction zone - an introduction*. Geological Society, London, Special Publications 311: 1-7.

Van Hinsbergen D. J., Maffione M., Koornneef L. M., Guilmette C., 2019. *Kinematic and paleomagnetic restoration of the Semail ophiolite (Oman) reveals subduction initiation along an ancient Neotethyan fracture zone*. Earth and Planetary Science Letters 518: 183-196.

Van Zuilen M. A., Fliegel D., Wirth R., Lepland A., Yuangao Q., Schreider A., Romashkin A. E., Philippot P., 2012. Mineral-templated Growth of Graphene-like Structures in Nature. Geochimica et Cosmochimica Acta 83: 252-262.

Vita-Finzi C., 2001. *Neotectonics at the Arabian plate margins*. Journal of Structural Geology 23 (2–3): 521-530.

Warburton J., Burnhill T. J., Graham R. H., Isaac K. P., 1990. *The evolution of the Oman Mountains Foreland Basin*. Geological Society, London, Special Publications 49: 419 – 427.

Warren C. J., Parrish R. R., Searle M. P., Waters D. J., 2003. *Dating the subduction of the Arabian continental margin beneath the Semail ophiolite, Oman*. Geology 31 (10): 889-892.

Warren C. J., Parrish R. R., Waters D. J., Searle M. P., 2005. *Dating the geologic history of Oman's Semail ophiolite: insights from U-Pb geochronology*. Contributions to Mineralogy and Petrology 150: 403-422.

Wehrmeister U., Jacob D., Soldati A., Hofmeister W., 2007. *Vaterite in freshwater cultured pearls from China and Japan*. The Journal of Gemmology 31: 399-416.

Weidle C., Wiesenberg L., Scharf A., Agard P., El-Sharkawy A., Krüger F., Meier T., 2023 Lithospheric evolution of eastern Arabia based on surface wave and receiver function analyses. Earth and Planetary Science Letters 611: 15 pages.

Zhao X., Zheng Z., Chen J., Gao Y., Sun J., Hou X., Xiong M., Mei S., 2022. *High P-T Calcite-Aragonite Phase Transitions Under Hydrous and Anhydrous Conditions*. Frontiers in Earth Science 10: 10 pages.

Zhu R., Zhao P., Zhao L., 2022. *Tectonic evolution and geodynamics of the Neo-Tethys Ocean*. Science China Earth Science 65: 1-24.

Zuccari C., Vignaroli G., Callegari I., Nestola F., Novella D., Giuntoli F., Guillong M., Viola G., 2023. *Forming and preserving aragonite in shear zones: First report of blueschist facies metamorphism in the Jabal Akhdar Dome, Oman Mountains*. Geology 51 (5): 454-459.

APPENDIX

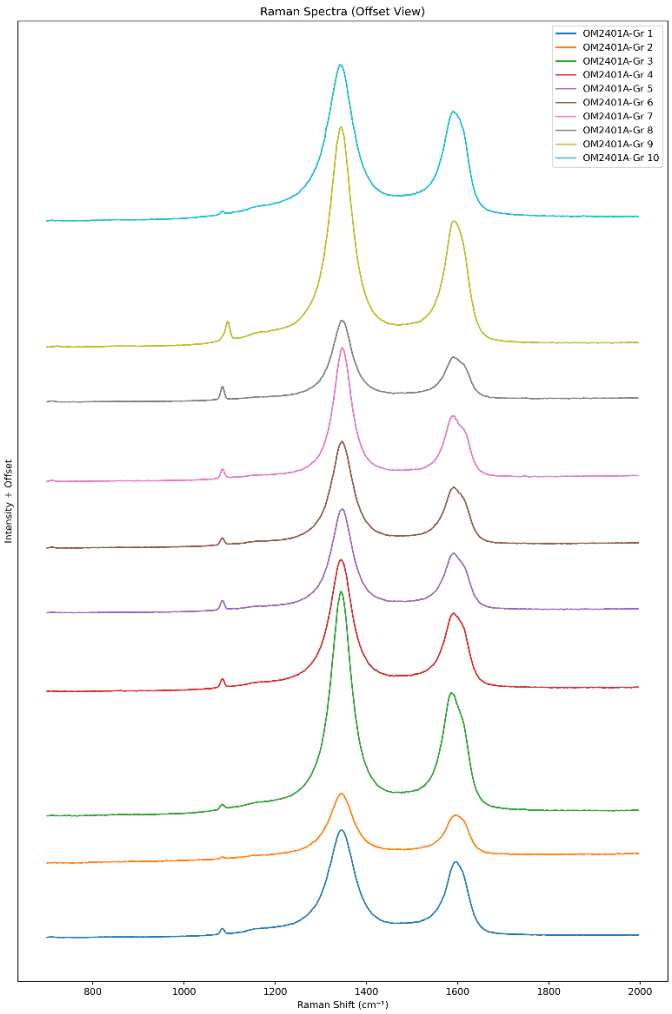

***Appendix 1**: Graphite Raman spectra acquired to estimate the temperature conditions of thin section OM2401A.*

	Analytic area D4	Analytic area D1	Analytic area D3	Analytic area G	Analytic area D2	RA1		T	d_std
OM2401A_Gr1	7365.3723	1.29E+05	1.27E+04	3.67E+04	1.71E+04	6.72E-01		369.90	0.028
OM2401A_Gr2	6174.66056	7.29E+04	7356.47365	24855.4504	9283.33419	6.56E-01		350.21	0.013
OM2401A_Gr3	13144.6085	2.15E+05	12945.7977	77146.7742	23840.9632	6.67E-01		363.45	0.028
OM2401A_Gr4	10502.5573	1.34E+05	10897.8288	4.45E+04	16813.6921	6.67E-01		363.75	0.028
OM2401A_Gr5	5979.43762	1.01E+05	8179.17652	32053.4852	11795.1866	6.74E-01		372.19	0.027
OM2401A_Gr6	4192.45459	1.05E+05	9129.66348	3.03E+04	13051.5609	6.75E-01		373.45	0.026
OM2401A_Gr7	4369.17799	1.09E+05	14616.6768	25318.3328	12684.9789	6.83E-01		384.08	0.014
OM2401A_Gr8	2508.43823	7.61E+04	5.18E+03	2.44E+04	9.34E+03	6.69E-01		366.33	0.029
OM2401A_Gr9	1.70E+04	2.26E+05	1.91E+04	6.25E+04	2.92E+04	6.86E-01		388.15	0.009
OM2401A_Gr10	18503.7021	1.85E+05	1.99E+04	6.51E+04	2.47E+04	6.50E-01		342.34	0.006
						Average	=	367.39	
						Dev Std	=	14	

***Appendix 2**: Temperature estimates for section OM2401A obtained through the Lahfid et al. (2010) method from analytic area ratios, along with associated standard deviations.*

	Analytic area D4	Analytic area D1	Analytic area D3	Analytic area G	Analytic area D2	RA1		T	d_std
OM2401A_Gr1	x	1.25E+05	x	3.58E+04	1.64E+04	7.06E-01		329.15	0.039
OM2401A_Gr2		7.25E+04		22861.1351	9790.3618	6.89E-01		336.23	0.025
OM2401A_Gr3		2.14E+05		61001.9729	32093.3051	6.97E-01		332.92	0.033
OM2401A_Gr4		1.15E+05		34011.6957	10560.6673	7.20E-01		323.02	0.038
OM2401A_Gr5		1.01E+05		26936.5343	13727.946	7.13E-01		325.97	0.041
OM2401A_Gr6		1.04E+05		19218.8663	14399.2261	7.56E-01		307.80	0.006
OM2401A_Gr7		1.09E+05		28668.7238	14237.821	7.17E-01		324.54	0.040
OM2401A_Gr8		7.58E+04		1.88E+04	1.00E+04	7.25E-01		321.13	0.035
OM2401A_Gr9		2.21E+05		5.51E+04	2.89E+04	7.25E-01		320.99	0.035
OM2401A_Gr10		1.84E+05		6.76E+04	2.20E+04	6.72E-01		343.54	0.009
						Average	=	326.53	
						Dev Std	=	10	

***Appendix 3**: Temperature estimates for section OM2401A obtained through the Aoya et al. (2010) method from analytic area ratios, along with associated standard deviations.*

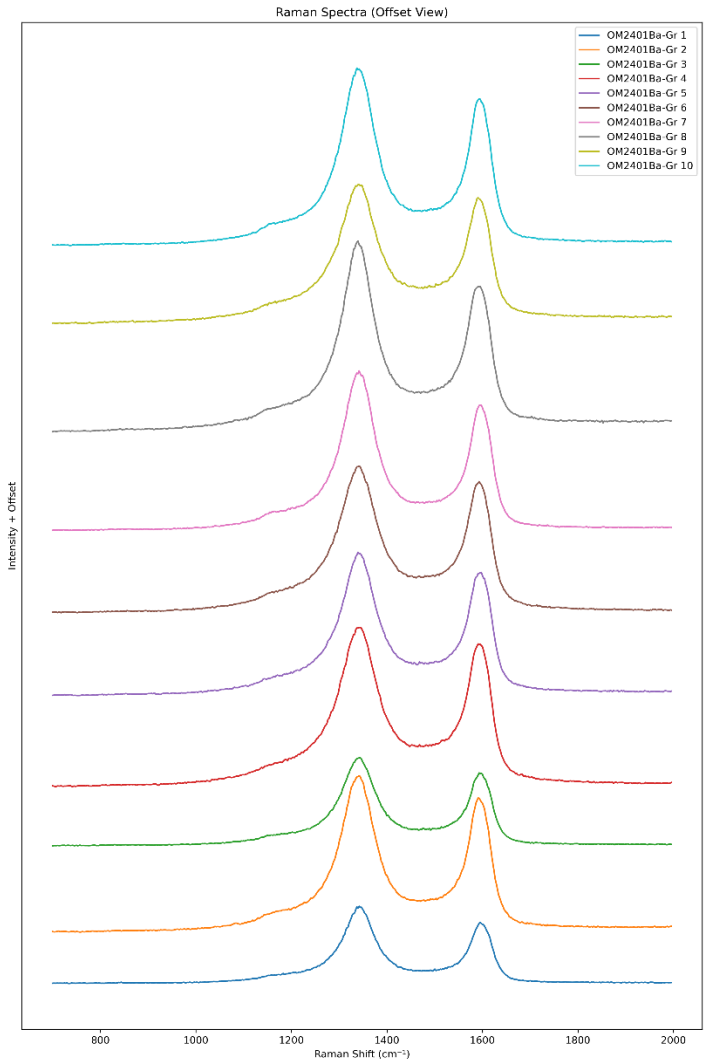

***Appendix 4**: Graphite Raman spectra acquired to estimate the temperature conditions of thin section OM2401Ba.*

	Analytic area D4	Analytic area D1	Analytic area D3	Analytic area G	Analytic area D2	RA1		T	d_std
OM2401Ba_Gr1	11697.8435	1.55E+05	1.68E+04	4.43E+04	1.57E+04	6.85E-01		**386.02**	0.005
OM2401Ba_Gr2	20155.3593	3.39E+05	39301.976	97396.4671	45381.4365	6.64E-01		**359.95**	0.029
OM2401Ba_Gr3	12618.6818	1.90E+05	21622.7666	53210.3425	23767.8573	6.73E-01		**371.59**	0.021
OM2401Ba_Gr4	32462.9851	3.87E+05	56759.2899	1.11E+05	52361.2872	6.55E-01		**349.56**	0.021
OM2401Ba_Gr5	27206.3946	3.12E+05	42718.901	94270.0808	44077.7177	6.52E-01		**345.20**	0.015
OM2401Ba_Gr6	24790.6133	3.52E+05	47596.4156	1.00E+05	49824.1785	6.56E-01		**350.49**	0.022
OM2401Ba_Gr7	20591.1815	3.31E+05	35425.7594	92412.9226	40792.6997	6.76E-01		**375.28**	0.016
OM2401Ba_Gr8	29990.3076	3.78E+05	47183.1502	1.11E+05	53013.048	6.59E-01		**353.79**	0.026
OM2401Ba_Gr9	27711.34	3.27E+05	47294.4444	96406.6432	43332.87	6.55E-01		**348.62**	0.020
OM2401Ba_Gr10	23062.8255	3.87E+05	44632.2732	1.09E+05	50236.5758	6.68E-01		**365.20**	0.028
						Average	=	**360.57**	
						Dev Std	=	14	

***Appendix 5**: Temperature estimates for section OM2401Ba obtained through the Lahfid et al. (2010) method from analytic area ratios, along with associated standard deviations.*

	Analytic area D4	Analytic area D1	Analytic area D3	Analytic area G	Analytic area D2	RA1		T	d_std
OM2401Ba_Gr1	x	1.57E+05	x	2.68E+04	2.66E+04	7.46E-01		**312**	0.023
OM2401Ba_Gr2		2.23E+05		80401.8793	42616.3469	6.45E-01		**356**	0.001
OM2401Ba_Gr3		1.92E+05		34743.5129	20741.8851	7.76E-01		**300**	0.017
OM2401Ba_Gr4		3.69E+05		75248.7758	41784.4013	7.59E-01		**307**	0.021
OM2401Ba_Gr5		2.90E+05		61619.1784	35190.1765	7.50E-01		**311**	0.022
OM2401Ba_Gr6		3.48E+05		78620.1749	26668.5036	7.68E-01		**303**	0.019
OM2401Ba_Gr7		3.31E+05		79933.1956	37758.1564	7.38E-01		**316**	0.022
OM2401Ba_Gr8		3.77E+05		75627.9684	37602.8927	7.69E-01		**303**	0.019
OM2401Ba_Gr9		2.96E+05		83803.94	40642.572	7.04E-01		**330**	0.014
OM2401Ba_Gr10		3.91E+05		73473.2263	35131.9863	7.83E-01		**297**	0.015
						Average	=	**313.31**	
						Dev Std	=	**18**	

***Appendix 6**: Temperature estimates for section OM2401Ba obtained through the Aoya et al. (2010) method from analytic area ratios, along with associated standard deviations.*

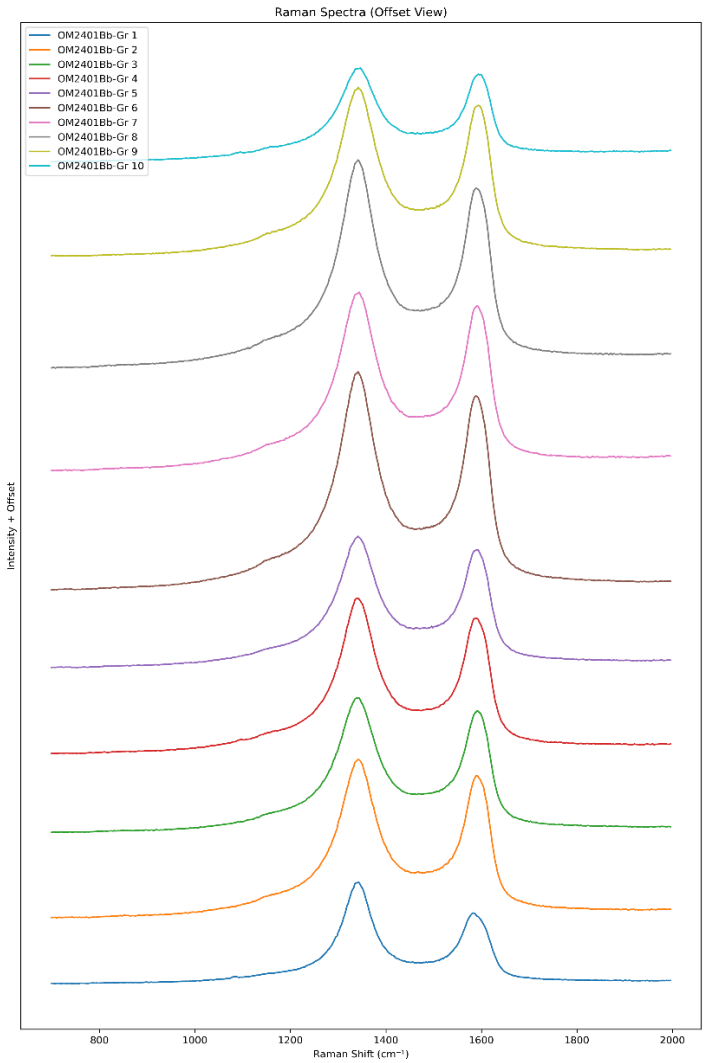

***Appendix 7**: Graphite Raman spectra acquired to estimate the temperature conditions of thin section OM2401Bb.*

	Analytic area D4	Analytic area D1	Analytic area D3	Analytic area G	Analytic area D2	RA1		T	d_std
OM2401Bb_Gr1	44490.7501	4.66E+05	6.46E+04	1.64E+05	5.92E+04	6.40E-01		**329.80**	0.036
OM2401Bb_Gr2	78749.3885	8.84E+05	1.46E+05	2.87E+05	1.25E+05	6.33E-01		**321.32**	0.075
OM2401Bb_Gr3	57385.1435	7.88E+05	1.22E+05	2.32E+05	1.22E+05	6.40E-01		**329.98**	0.034
OM2401Bb_Gr4	72324.7963	8.35E+05	1.34E+05	2.87E+05	1.16E+05	6.29E-01		**315.99**	0.024
OM2401Bb_Gr5	68182.7094	7.54E+05	1.26E+05	2.43E+05	1.07E+05	6.34E-01		**322.34**	0.081
OM2401Bb_Gr6	1.12E+05	1.22E+06	2.01E+05	4.04E+05	1.70E+05	6.33E-01		**320.97**	0.072
OM2401Bb_Gr7	77507.053	1.00E+06	1.67E+05	3.21E+05	1.43E+05	6.31E-01		**319.34**	0.057
OM2401Bb_Gr8	1.09E+05	1.10E+06	1.81E+05	3.69E+05	1.50E+05	6.33E-01		**322.06**	0.080
OM2401Bb_Gr9	71134.9814	9.70E+05	1.48E+05	2.92E+05	1.48E+05	6.39E-01		**329.38**	0.040
OM2401Bb_Gr10	41546.8158	5.08E+05	77944.7254	1.57E+05	81108.9156	6.35E-01		**324.41**	0.082
						Average	**=**	**323.56**	
						Dev Std	**=**	**5**	

***Appendix 8**: Temperature estimates for section OM2401Bb obtained through the Lahfid et al. (2010) method from analytic area ratios, along with associated standard deviations.*

	Analytic area D4	Analytic area D1	Analytic area D3	Analytic area G	Analytic area D2	RA1		T	d_std
OM2401Bb_Gr1	x	4.20E+05	x	1.25E+05	6.01E+04	6.94E-01		**334**	0.023
OM2401Bb_Gr2		5.44E+05		2.55E+05	94183.9528	6.09E-01		**371**	0.002
OM2401Bb_Gr3		7.16E+05		1.62E+05	79337.8599	7.48E-01		**311**	0.009
OM2401Bb_Gr4		7.19E+05		2.25E+05	1.03E+05	6.86E-01		**338**	0.023
OM2401Bb_Gr5		6.42E+05		1.95E+05	96385.6807	6.88E-01		**337**	0.023
OM2401Bb_Gr6		1.03E+06		3.20E+05	1.46E+05	6.88E-01		**337**	0.023
OM2401Bb_Gr7		7.46E+05		2.65E+05	1.26E+05	6.56E-01		**351**	0.015
OM2401Bb_Gr8		9.76E+05		2.59E+05	1.04E+05	7.29E-01		**319**	0.015
OM2401Bb_Gr9		8.84E+05		2.53E+05	1.24E+05	7.01E-01		**331**	0.023
OM2401Bb_Gr10		4.64E+05		1.20E+05	51079.5909	7.31E-01		**318**	0.015
						Average	**=**	**334.79**	
						Dev Std	**=**	**17**	

***Appendix 9**: Temperature estimates for section OM2401Bb obtained through the Aoya et al. (2010) method from analytic area ratios, along with associated standard deviations.*

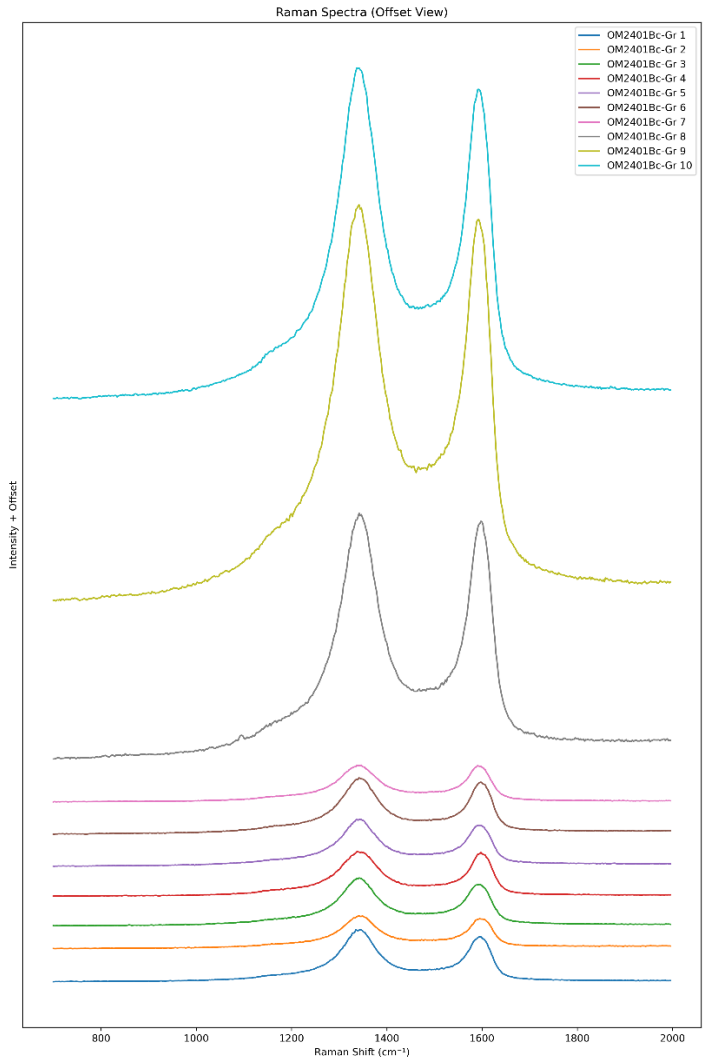

***Appendix 10**: Graphite Raman spectra acquired to estimate the temperature conditions of thin section OM2401Bc.*

	Analytic area D4	Analytic area D1	Analytic area D3	Analytic area G	Analytic area D2	RA1		T	d_std
OM2401Bc_Gr1	15621.3	1.85E+05	2.42E+04	5.31E+04	2.83E+04	6.55E-01		**348.93**	0.030
OM2401Bc_Gr2	8737.01583	1.13E+05	15469.1819	35850.6341	16013.4452	6.44E-01		**335.42**	0.037
OM2401Bc_Gr3	14457.2482	1.74E+05	26181.6347	52561.8562	25814.2548	6.43E-01		**333.83**	0.032
OM2401Bc_Gr4	9467.75365	1.76E+05	22572.4353	4.91E+04	22556.8972	6.63E-01		**359.05**	0.006
OM2401Bc_Gr5	15345.3465	1.65E+05	25021.179	50944.4782	23277.8082	6.45E-01		**336.83**	0.040
OM2401Bc_Gr6	14959.1743	2.03E+05	25825.9469	5.98E+04	28442.3374	6.56E-01		**350.55**	0.025
OM2401Bc_Gr7	9266.85921	1.43E+05	20406.678	43431.2202	20774.7669	6.43E-01		**334.58**	0.034
OM2401Bc_Gr8	53545.7935	9.20E+05	1.29E+05	2.73E+05	1.42E+05	6.42E-01		**332.46**	0.029
OM2401Bc_Gr9	1.39E+05	1.69E+06	3.10E+05	4.69E+05	2.35E+05	6.43E-01		**334.13**	0.033
OM2401Bc_Gr10	90399.4638	1.33E+06	1.89E+05	3.82E+05	1.90E+05	6.50E-01		**343.28**	0.042
						Average	**=**	**340.91**	
						Dev Std	**=**	**9**	

***Appendix 11**: Temperature estimates for section OM2401Bc obtained through the Lahfid et al. (2010) method from analytic area ratios, along with associated standard deviations.*

	Analytic area D4	Analytic area D1	Analytic area D3	Analytic area G	Analytic area D2	RA1		T	d_std
OM2401Bc_Gr1	x	1.15E+05	x	4.88E+04	2.41E+04	6.12E-01		**370**	0.022
OM2401Bc_Gr2		6.96E+04		33963.6041	13931.296	5.92E-01		**379**	0.015
OM2401Bc_Gr3		1.09E+05		36211.4111	19451.3557	6.61E-01		**349**	0.017
OM2401Bc_Gr4		1.03E+05		43749.9165	16948.6654	6.30E-01		**362**	0.025
OM2401Bc_Gr5		1.11E+05		44251.832	14139.913	6.55E-01		**351**	0.019
OM2401Bc_Gr6		1.29E+05		53635.897	15239.185	6.52E-01		**353**	0.020
OM2401Bc_Gr7		7.03E+04		41713.5435	16488.6171	5.47E-01		**399**	0.002
OM2401Bc_Gr8		5.80E+05		2.26E+05	1.16E+05	6.29E-01		**363**	0.025
OM2401Bc_Gr9		9.51E+05		3.36E+05	1.57E+05	6.59E-01		**349**	0.018
OM2401Bc_Gr10		8.31E+05		2.97E+05	1.48E+05	6.51E-01		**353**	0.020
						Average	**=**	**362.77**	
						Dev Std	**=**	**16**	

***Appendix 12**: Temperature estimates for section OM2401Bc obtained through the Aoya et al. (2010) method from analytic area ratios, along with associated standard deviations.*

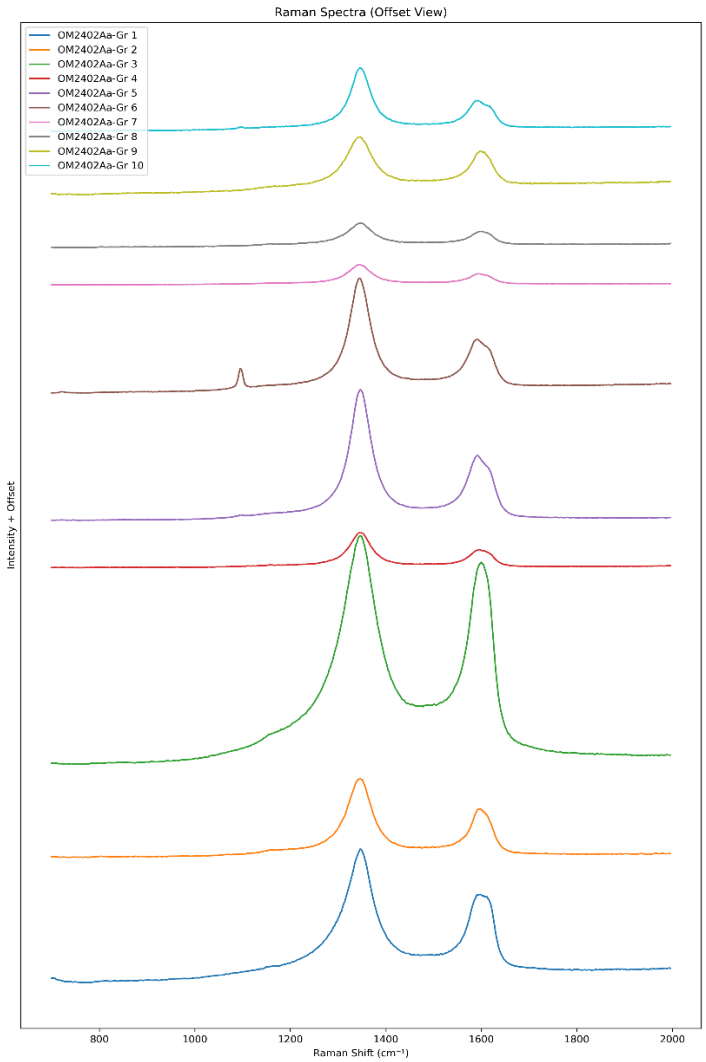

***Appendix 13**: Graphite Raman spectra acquired to estimate the temperature conditions of thin section OM2402Aa.*

	Analytic area D4	Analytic area D1	Analytic area D3	Analytic area G	Analytic area D2	RA1	T	d_std
OM2402Aa_Gr1	68898.8994	1.31E+05	1.67E+04	5.44E+04	2.08E+04	6.85E-01	**386.79**	0.015
OM2402Aa_Gr2	7323.86178	9.21E+04	7303.36388	24948.3054	10182.0508	7.01E-01	**406.44**	0.013
OM2402Aa_Gr3	46551.4275	3.78E+05	59019.6193	1.21E+05	53271.682	6.45E-01	**336.63**	0.002
OM2402Aa_Gr4	2779.07234	3.62E+04	3641.95043	8.02E+03	4015.75352	7.13E-01	**421.38**	0.007
OM2402Aa_Gr5	7273.95239	1.34E+05	8818.5452	42445.4908	14259.2794	6.83E-01	**384.46**	0.015
OM2402Aa_Gr6	2388.98879	1.12E+05	5657.33329	3.29E+04	10019.0392	7.03E-01	**408.96**	0.012
OM2402Aa_Gr7	1847.00406	2.21E+04	2101.37706	5657.36695	2169.79034	7.07E-01	**413.45**	0.010
OM2402Aa_Gr8	6343.32904	2.72E+04	3.61E+03	9.20E+03	2.68E+03	6.84E-01	**385.23**	0.015
OM2402Aa_Gr9	4.56E+03	6.67E+04	7.63E+03	2.16E+04	6.94E+03	6.63E-01	**359.23**	0.008
OM2402Aa_Gr10	3861.09841	5.96E+04	2.74E+03	1.95E+04	5.91E+03	6.93E-01	**396.10**	0.015
						Average	= **389.87**	
						Dev Std	= 26	

***Appendix 14**: Temperature estimates for section OM2402Aa obtained through the Lahfid et al. (2010) method from analytic area ratios, along with associated standard deviations.*

	Analytic area D4	Analytic area D1	Analytic area D3	Analytic area G	Analytic area D2	RA1	T	d_std
OM2402Aa_Gr1	x	1.26E+05	x	5.18E+04	1.65E+04	6.47E-01	**354**	0.008
OM2402Aa_Gr2		9.20E+04		20569.6681	11911.9233	7.39E-01	**315**	0.016
OM2402Aa_Gr3		2.89E+05		1.19E+05	55959.7284	6.23E-01	**365**	0.003
OM2402Aa_Gr4		3.22E+04		7321.28408	3510.82476	7.48E-01	**311**	0.014
OM2402Aa_Gr5		1.34E+05		34266.7796	18180.2946	7.19E-01	**324**	0.021
OM2402Aa_Gr6		1.13E+05		25393.7389	13123.4874	7.46E-01	**312**	0.015
OM2402Aa_Gr7		2.20E+04		5333.43662	2237.76958	7.44E-01	**313**	0.015
OM2402Aa_Gr8		2.63E+04		8.72E+03	2.90E+03	6.94E-01	**334**	0.021
OM2402Aa_Gr9		6.64E+04		1.99E+04	8.38E+03	7.01E-01	**331**	0.021
OM2402Aa_Gr10		5.94E+04		1.82E+04	5.84E+03	7.12E-01	**326**	0.021
						Average	= **328.70**	
						Dev Std	= **19**	

***Appendix 15**: Temperature estimates for section OM2402Aa obtained through the Aoya et al. (2010) method from analytic area ratios, along with associated standard deviations.*

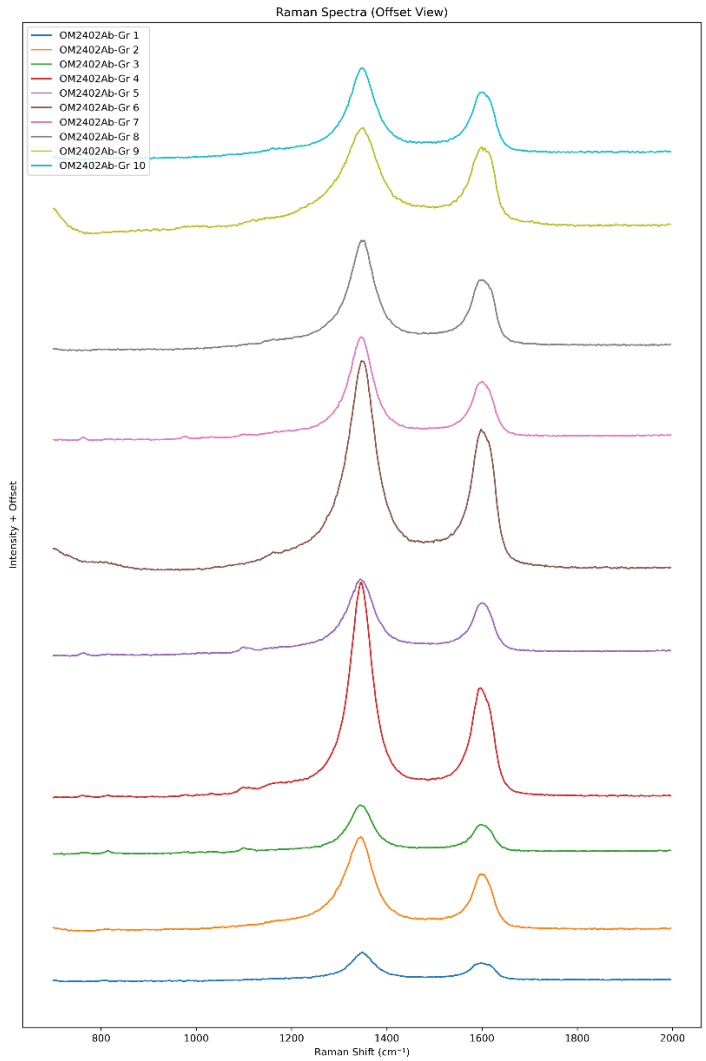

***Appendix 16**: Graphite Raman spectra acquired to estimate the temperature conditions of thin section OM2402Ab.*

	Analytic area D4	Analytic area D1	Analytic area D3	Analytic area G	Analytic area D2	RA1		T	d_std
OM2402Ab_Gr1	2237.59992	1.18E+04	1.23E+03	4.26E+03	1.50E+03	6.67E-01		**363.81**	0.008
OM2402Ab_Gr2	8492.12464	4.26E+04	5099.08605	10039.1385	4622.69441	7.21E-01		**431.82**	0.006
OM2402Ab_Gr3	2949.95918	2.02E+04	1475.02107	5.15E+03	2242.05885	7.23E-01		**434.03**	0.006
OM2402Ab_Gr4	6681.46618	8.44E+04	6553.44932	2.08E+04	8731.66985	7.16E-01		**425.28**	0.008
OM2402Ab_Gr5	4884.92194	3.53E+04	4615.09198	9472.37217	4364.93856	6.85E-01		**386.93**	0.012
OM2402Ab_Gr6	18270.1807	9.38E+04	9003.55654	3.08E+04	12158.2054	6.83E-01		**384.23**	0.012
OM2402Ab_Gr7	4481.88817	4.22E+04	3228.89345	10226.598	4972.94744	7.17E-01		**426.48**	0.008
OM2402Ab_Gr8	7737.55604	4.66E+04	4.74E+03	1.57E+04	5.67E+03	6.76E-01		**374.77**	0.010
OM2402Ab_Gr9	1.69E+04	5.99E+04	1.11E+04	1.94E+04	7.06E+03	6.72E-01		**369.89**	0.009
OM2402Ab_Gr10	4366.87133	4.18E+04	4.66E+03	1.44E+04	5.17E+03	6.55E-01		**349.46**	0.005
						Average	=	**394.67**	
						Dev Std	=	**32**	

***Appendix 17**: Temperature estimates for section OM2402Ab obtained through the Lahfid et al. (2010) method from analytic area ratios, along with associated standard deviations.*

	Analytic area D4	Analytic area D1	Analytic area D3	Analytic area G	Analytic area D2	RA1		T	d_std
OM2402Ab_Gr1	x	1.16E+04	x	3.99E+03	1.39E+03	6.84E-01		**339**	0.015
OM2402Ab_Gr2		4.28E+04		8169.11748	4770.02875	7.68E-01		**303**	0.010
OM2402Ab_Gr3		2.02E+04		4.90E+03	2184.19991	7.41E-01		**314**	0.024
OM2402Ab_Gr4		8.41E+04		17286.2804	9453.17056	7.59E-01		**307**	0.015
OM2402Ab_Gr5		3.50E+04		9474.30924	4770.44852	7.11E-01		**327**	0.028
OM2402Ab_Gr6		9.47E+04		28328.1591	12310.9798	7.00E-01		**332**	0.024
OM2402Ab_Gr7		4.19E+04		9220.45662	5260.6473	7.43E-01		**313**	0.023
OM2402Ab_Gr8		4.61E+04		1.34E+04	6.58E+03	6.98E-01		**333**	0.022
OM2402Ab_Gr9		6.21E+04		1.73E+04	5.27E+03	7.33E-01		**317**	0.027
OM2402Ab_Gr10		4.14E+04		1.35E+04	6.51E+03	6.75E-01		**343**	0.010
						Average	=	**322.80**	
						Dev Std	=	**14**	

***Appendix 18**: Temperature estimates for section OM2402Ab obtained through the Aoya et al. (2010) method from analytic area ratios, along with associated standard deviations.*

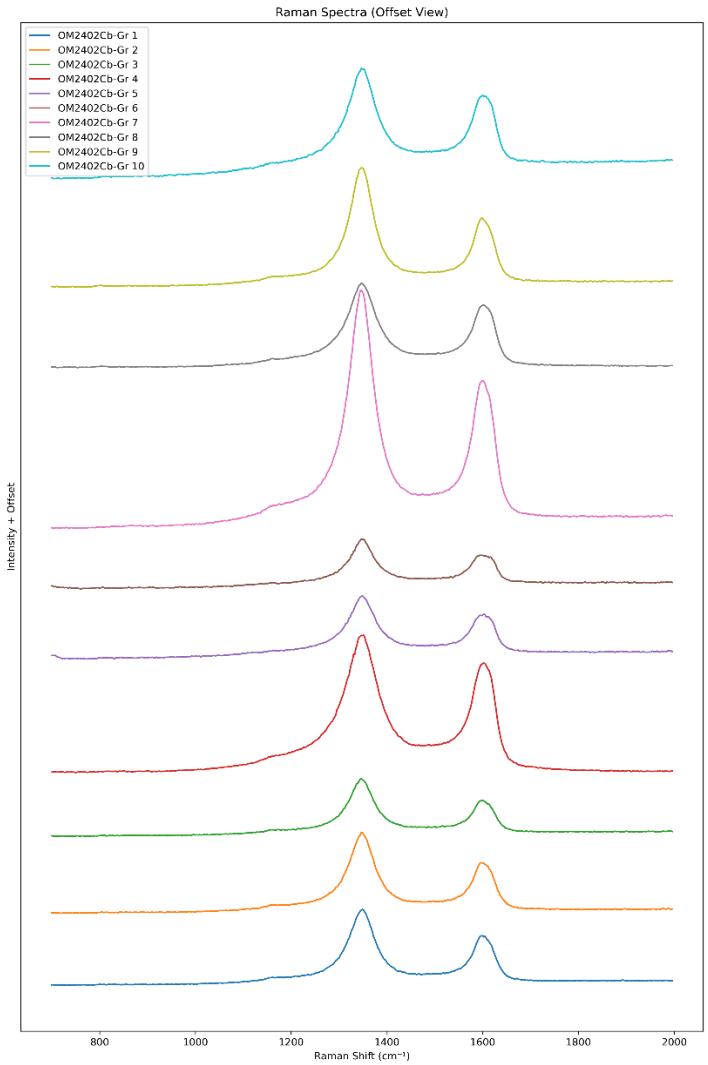

***Appendix 19**: Graphite Raman spectra acquired to estimate the temperature conditions of thin section OM2402Cb.*

	Analytic area D4	Analytic area D1	Analytic area D3	Analytic area G	Analytic area D2	RA1		T	d_std
OM2402Cb_Gr1	3503.06452	4.73E+04	3.97E+03	1.36E+04	5.35E+03	6.89E-01		**391.21**	0.012
OM2402Cb_Gr2	4339.05964	4.99E+04	4290.82636	14270.0523	5607.32714	6.92E-01		**395.10**	0.011
OM2402Cb_Gr3	3247.368	3.43E+04	3002.95887	1.05E+04	3343.7477	6.91E-01		**393.51**	0.012
OM2402Cb_Gr4	13719.0493	1.11E+05	14049.9574	3.30E+04	14496.7919	6.69E-01		**366.89**	0.015
OM2402Cb_Gr5	8480.83153	3.80E+04	5163.8461	13899.0505	4801.71181	6.61E-01		**356.41**	0.012
OM2402Cb_Gr6	5411.62012	2.62E+04	3693.28737	1.11E+04	3446.66565	6.34E-01		**322.51**	0.002
OM2402Cb_Gr7	14597.7018	1.45E+05	12469.6396	42784.0762	16790.7991	6.89E-01		**390.91**	0.013
OM2402Cb_Gr8	5951.59569	5.93E+04	6.94E+03	1.83E+04	7.54E+03	6.66E-01		**362.63**	0.014
OM2402Cb_Gr9	5.04E+03	6.88E+04	5.02E+03	1.91E+04	6.86E+03	7.04E-01		**410.82**	0.006
OM2402Cb_Gr10	9961.0924	6.99E+04	8.71E+03	2.34E+04	8.76E+03	6.61E-01		**356.67**	0.012
						Average	=	**374.66**	
						Dev Std	=	**26**	

***Appendix 20**: Temperature estimates for section OM2402Cb obtained through the Lahfid et al. (2010) method from analytic area ratios, along with associated standard deviations.*

	Analytic area D4	Analytic area D1	Analytic area D3	Analytic area G	Analytic area D2	RA1		T	d_std
OM2402Cb_Gr1	x	4.73E+04	x	1.01E+04	6.43E+03	7.41E-01		**314**	0.015
OM2402Cb_Gr2		4.99E+04		13622.4247	6040.32871	7.17E-01		**324**	0.030
OM2402Cb_Gr3		3.42E+04		8.45E+03	4629.38512	7.23E-01		**322**	0.027
OM2402Cb_Gr4		1.10E+05		32443.7939	13965.4588	7.03E-01		**330**	0.033
OM2402Cb_Gr5		3.82E+04		13532.8716	4827.09321	6.76E-01		**342**	0.019
OM2402Cb_Gr6		2.55E+04		11120.2032	2737.14313	6.48E-01		**354**	0.004
OM2402Cb_Gr7		1.44E+05		42232.3004	17147.7866	7.08E-01		**328**	0.033
OM2402Cb_Gr8		5.98E+04		1.71E+04	7.58E+03	7.08E-01		**328**	0.033
OM2402Cb_Gr9		6.86E+04		1.65E+04	7.98E+03	7.37E-01		**316**	0.018
OM2402Cb_Gr10		6.90E+04		2.08E+04	1.02E+04	6.90E-01		**336**	0.029
						Average	=	**329.54**	
						Dev Std	=	**12**	

***Appendix 21**: Temperature estimates for section OM2402Cb obtained through the Aoya et al. (2010) method from analytic area ratios, along with associated standard deviations.*

AKNOWLEDGEMENTS

I would like to express my sincere gratitude to the members of the Department who have contributed to the development of this work. In particular, I am deeply thankful to my supervisor, Prof. Giulio Viola, for his insightful guidance, constructive feedback, and continuous support throughout the research process. I am also grateful to my co-supervisor, Dr. Costantino Zuccari, and Sara, for their valuable advice, assistance, and encouragement during various stages of my research, as well as to all the others who took part in the mission in Oman: Prof. Francesco Giuntoli, Prof. Ivan Callegari, Alessandro, and Luciano.

Un grazie di cuore alla mia famiglia, Silvia, Roberto, Clara e Amelia, e ai miei amici, per esserci sempre stati, per la pazienza, per le risate e per avermi fatto sentire sostenuto costantemente.

A special thank you goes to Aleksandra, for her invaluable emotional and psychological support. Your presence made this journey lighter and brighter.